UNIVERSITÀ DI PISA
Scuola di Ingegneria

Corso di Laurea Magistrale in
INGEGNERIA MECCANICA

DEVELOPMENT OF MODELING TECHNIQUES FOR ROLLING ELEMENT BEARINGS

THESIS PRESENTED FOR THE ACHIEVEMENT OF MASTER'S DEGREE IN
MECHANICAL ENGINEERING

Author:
Leoluca Scurria

Supervisors:
Prof. Leonardo Bertini
Dr. Gert Heirman

Academic year 2015/2016

Alla mia Famiglia

Abstract

Nowadays rolling element bearings represent the most used low-friction supports usable in a wide range of applications thanks to their possibility to be adapted to a wide range of applications. They allow rotation in one direction while constraining the motions (2 rotations and 3 translations) along the other directions.

This thesis work aims at the numerically efficient simulation of bearing behavior and a high fidelity prediction of the contact loads by including the most significant phenomena, such as lubrication, clearance, preload, gyroscopic moments and centrifugal loads.

The bearing's inner ring is considered to have 5 dofs (degrees of freedom relatively to the outer ring) while the reaction forces and moments are computed as output. The models are based on contact behavior evaluation under different assumptions. The first step of fidelity concerns the "idealized model" in dry contact model is adopted. In a second level of fidelity the clearance and the preload are introduced. Since rolling element bearings can operate at high speeds (e.g. 12000 rpm), as third fidelity level the centrifugal load on the rolling elements is introduced. This load is due to the rotation speed of the rolling elements around the bearing axis. The highest fidelity level in this work introduces the lubrication. Since the contacts between the rolling element and the raceways are non-conformal contacts, the elastohydrodynamic lubrication theory is used.

The research presented in this thesis is the result of the work performed during a 6 months internship in Siemens Industry Software, Leuven, Belgium, within the 3D simulation division, focusing on drivetrain simulation for LMS Virtual.Lab Motion within the Mechatronics Research and Technology Development team of the 3D Simulation Division. At the time of writing of this thesis, the modeling techniques developed in this work are being integrated by means of a prototype implementation in the commercially available multibody simulation tool LMS Virtual.Lab Motion.

Acknowledgments

I would like to thank Professor Leonardo Bertini who gave me the opportunity to have this inspiring experience, in which I grew up and I learned more than I thought.

A thank you to my company supervisor Dr. Gert Heirman which had fully supported me during this six months, sharing with me his deep knowledge in the matter. Moreover thank you for the effort and the several extra working hours we spent together, working for new possibilities.

Thank you to all the Driveline RTD Team for have opened my mind with your knowledge.

A thank you from the bottom of my heart to my dad Salvatore and my mother Mariarosa for supporting me during the whole academic path, sharing happiness, worries, and all the feelings I have felt during these years.

To my friend and sister Matilde for believing in me at least as much as I believe in her, as person first and as Engineer too, for the hours spent enjoying life as well as solving technical problems.

To my girlfriend Arianna which has walked beside me through this though path, sharing the loads weighting on our shoulders. She turned everything to colors.

Thank you to all my friends and colleagues in Siemens for the enjoyed time within and out of the company.

Massa Marittima,
April 2016

Scurria Leoluca

Ringraziamenti

Voglio ringraziare il Professor Leonardo Bertini il quale mi ha dato l'opportunità di fare questa stimolante esperienza, nella quale sono cresciuto molto ed ho imparato più di quanto potessi immaginare.

Un ringraziamento al mio supervisor aziendale Dr. Gert Heirman il quale mi ha pienamente supportato durante questi sei mesi, condividendo con me la sua grande esperienza nel campo. Inoltre grazie per l'impegno e le molte ore extra'lavorative spese insieme per aprirmi nuove possibilità.

Un grazie a tutto il team Driveline RTD per avermi aperto la mente con la vostra conoscenza.

Un grazie dal profondo del cuore a mio padre Salvatore ed a mia madre Mariarosa per avermi supportato durante l'intero percorso universitario, condividendo felicità, preoccupazioni e tutte i sentimenti provati in questi anni.

Alla mia amica e sorella Matilde per aver creduto in me almeno quanto io credo in lei, come persona in primis ed anche come Ingegnere, per le ore spese godendoci la vita così come per le ore spese a risolvere problemi tecnici.

Alla mia fidanzata Arianna che ha camminato accanto a me attraverso questo duro cammino, condividendo il peso sulle nostre spalle. Ha reso tutto più colorato.

Grazie a tutti i miei amici e colleghi di Siemens per il tempo goduto sia all'interno che all'esterno dell'azienda.

Massa Marittima,
Aprile 2016

Scurria Leoluca

Contents

List of Figures

List of Tables

Nomenclature

$\mathbf{u}$	Inner-raceway groove center displacement vector
α	Nominal contact angle
α_0	The α value with all the axial clearance on one side
α_r	Contact angle in displaced configuration
α_{barus}	Lubricant pressure-viscosity coefficient
α_{max}	Maximum contact angle allowed
α_{tot}	Equivalent bearing angle
β	Roller angle
Δ	Dimensionless penetration
δ	Mutual approach of bodies in contact
$\delta^\star$	Dimensionless contact deformation
δ_a	Axial inner ring displacement
δ_i	Ball-inner raceway penetration
δ_i	Linear displacement along the *i-axis*
δ_o	Ball-outer raceway penetration
δ_r	Radial inner ring displacement
η_0	Lubricant viscosity at ambient pressure
γ_j	Rotational displacement along the *j-axis*
κ	Elliptical eccentricity parameter (a/b)
ν	Poisson ratio
ν	Poisson ration
ω_b	Ball rotational speed

ω_{pw} Rotational velocity of ball center around the bearing axis

ω_{shaft} Shaft rotational speed

$\overline{h}_c$ Dimensionless fluid film thickness in the center of the contact

ρ Material density

$\rho_{k,j}$ Curvature of the body k along the principal plane j

$\Sigma\rho$ Curvature sum

CrownDrop Crown drop vector

E Complete elliptic integral of the second kind

F Complete elliptic integral of the first kind

f Residual forces vector

J Jacobian matrix

$\mathbf{R}_{ij}$ Rotation matrix from $i - coordinates$ to $j - coordinates$

$\mathbf{W}_{gl}$ Wrench transformation matrix

${}^{j}w$ Wrench vector w.r.t. the $j-$coordinate system

A Degree of the curvature of the crowning curve

A Distance between raceway groove curvature centers

a Semimajor axis of the projected contact

$a^{\star}$ Dimensionless semimajor axis of contact ellipse

A_0 The A value with all the axial clearance on one side

A_r Distance between raceway groove curvature centers in displaced configuration

B Outer ring width

B Total curvature of the bearing

b Semiminor axis of the projected contact

$b^{\star}$ Dimensionless semiminor axis of contact ellipse

cl Radial clearance in roller bearings

$clnc$ Axial clearance

$clnc_r$ Radial clearance in deep groove ball bearing

D Ball Roller diameter

D_g Major tapered roller radius

D_l Minor tapered roller radius

D_{ib} Inner bore diameter

D_{ob} Outer bore diameter

d_{pw} Pitch diameter

E Young modulus

E Young's modulus

E_{eq} Reduced modulus of elasticity

$F(\rho)$ Curvature difference

f_i Ball-Inner ring osculation

f_o Ball-Outer ring osculation

G Dimensionless material parameter

H_c Dimensionless fluid film thickness in the center of the contact

K_{qj} Load deflection factor for inner($j = i$) and outer($j = o$) ring

L Contact line length

L Dimensionless lubricant parameter

L Dimensionless material parameter

l Slice length

l_s Length of the central straight zone

M Dimensionless load parameter

m Amount of slices

N Dimensionless load parameter

$prel$ Axial preload

Q Force applied on the contact

$q_{i,j}$, $q_{o,j}$ Contact force between the j-th slice and the inner/outer raceway

R_i Inner raceway radius of curvature (Roller Bearing)

r_i Inner-raceway groove curvature radius

r_o Outer-raceway curvature radius

r_p	Radius of the inner raceway groove center
r_q	Radius of the outer raceway groove center
$R_{i,x}$	Reduced radius of curvature along the x axis w.r.t. the inner-raceway point of contact
$R_{i,y}$	Reduced radius of curvature along the y axis w.r.t. the inner-raceway point of contact
$R_{j,x}$	Reduced radius of curvature w.r.t. body j in ball's motion direction lying in the contact plane
$R_{j,y}$	Major reduced radius of curvature w.r.t. body j (Perpendicular to x and lying on the contact plane)
$R_{k,eq}$	Reduced radius of curvature (contact k)
$R_{k,j}$	Radius of the body k along the principal plane j
$R_{o,x}$	Reduced radius of curvature along the x axis w.r.t. the outer-raceway point of contact
$R_{o,y}$	Reduced radius of curvature along the y axis w.r.t. the outer-raceway point of contact
r_{pw}	Pitch radius
S_j	Cartesian coordinate system $\{x_j, y_j, z_j\}$
t	Outer ring thickness
U	Dimensionless velocity
u_a	Inner raceway axial displacement (groove center)
u_r	Inner raceway radial displacement (groove center)
u_s	Sum velocity
v_a	Rolling element axial displacement
v_r	Rolling element radial displacement
W	Dimensionless load parameter
Z	Number of rolling elements
z_j	Distance, along the z_l axis, between the roller mean plane and j-th slice's mean plane
z_m	Crown drop at the end of the ends of the effective contact
dof	Degrees of Freedom
w.r.t.	With respect to

Chapter 1

Introduction

Rolling element bearings are used to allow low friction rotation in one direction while constraining motion along the others (three translations, two rotations). They are largely used in drivelines and gearboxes, mostly to support gears mounted on shafts.

The bearing is composed by four parts which are shown in Figure 1.1.

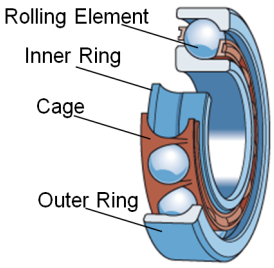

Figure 1.1: Parts composing the bearing

In this work the rolling element can be both a ball (i.e. ball bearings) and a roller (i.e. cylindrical roller and tapered roller bearings). The rolling elements roll on the raceways which are located in the internal part of the rings. The nominal contact between the rolling element and the raceways can be a point (e.g. ball bearings) or a line (e.g. roller bearings). The contacts in which the nominal (unloaded case) contact print has a null area are called as non-conformal.

Due to the non-linearity introduced by the non-conformal contacts within the bearings, the system level and the sub-system level behavior can no longer be studied separately. In order to evaluate the $N\&V$ (Noise and Vibration) behavior of mechanical systems, high-fidelity models for rolling element bearings are required.

The proposed work aim at the high fidelity prediction of rolling element bearings in order to allow system level $N\&V$ analysis.

The proposed work is divided in two parts, the first one concerns the modeling of ball bearings (i.e. point contact), while the second one concerns roller bearings (i.e. line contact).

Each part starts with the contact modeling in order to compute the equilibrium of the rolling element squeezed between the raceways under assumptions which become

less strict at each step.

Part I starts with Chapter 4 in which an Idealized model is introduced, which takes into account only the non liearity coming from the non-conformal contacts in order to compute the rolling element equilibrium. Chapter 4 introduces also the effects of clearance and preload, which can deeply change the load-deflection characteristic curve of the rolling element. Since the bearing can rotate up to tens of thousands RPM, the rolling elements rotates around the bearing shaft with a speed which can provoke non-negligible centrifugal load on the rolling element. The effect of the centrifugal load on the ball equilibrium is therefore introduced in Chapter 5. In angular contact ball bearings, the centrifugal load provokes the loss of symmetry, hence the solution requires an iterative process. Since almost all bearings operate in lubricated conditions, Chapter 6 introduces the lubricated contact in elastohydrodynamic regime (EHL). EHL introduces more physics to the model and moreover gives a more reliable solution. The model presented in Chapter 6 represents the most advanced contact modeling technique since it accounts for the most influencing phenomena such as lubrication, centrifugal load, clearance and preload. Finally Chapter 7 concerns the procedure to account for the contact modeling techniques developed through the beforehand Chapters in the bearing behavior description. The procedure considers as input a 5 dofs (degrees of freedom) inner ring displacement (two tilting and three translations). This input is used to calculate the displacement of the inner ring (w.r.t. the outer ring) in correspondence of each rolling element. Then the contact model calculates the reaction forces due to that displacement. Once the reaction forces are computed, they are summed in order to calculate the reaction forces and moments in correspondence of the bearing axis.

Then Part II is introduced, which concerns roller bearings. Chapter 7 introduces the solution for dry line contact, accounting for centrifugal load, clearance, crowning and misalignment between the roller and the raceway. Then the contact model developed is used to compute the equilibrium of a cylindrical roller squeezed between the raceways. Chapter 11 introduces the EHL line contact, which allows more accurate analysis. Then the solution becomes more speed dependent since the lubricant plays a key role. Chapter 11 shows the procedures to account for lubricated line contact in cylindrical roller equilibrium. The developed line contact modeling techniques in the beforehand Chapters are then used to compute the equilibrium of a tapered roller in Chapter 12. The equilibrium of a tapered roller introduces more variables, such as flange contact force and gyroscopic moment. Finally Chapter 13 introduces the procedure to compute the solution of the whole bearing considering different contact models in order to compare them. The procedure is based on Chapter 7 even if it includes minor corrections.

Chapter 2

State of the Art

"Nanos gigantium humeris insidentes"
-Bernardo di Chartres

The behavior evaluation of a rolling element bearing is in general a nonlinear, statically indeterminate problem, except for simple cases such as purely axially loaded thrust ball bearings. More complicated cases can be studied manually introducing simplifying assumptions; see Palmgren [1]. If those assumptions are not allowed or desired, iterative processes and computer simulations have to be introduced.

Models to describe the bearing behavior have been published by Jones [2] [3]. The work done in [2] includes systems consisting of a number of rolling element bearings on a rigid shaft, introducing major assumptions not allowed for our purpose (e.g. low speed roller bearings, non-misaligned cylindrical roller bearings etc..). In [3], the shaft flexibility has been introduced, by means of influence factors. Later, Jones and McGrew [4] [5] [6] have done a step further in the analysis of ball, tapered roller and cylindrical roller bearings (flangeless inner and outer ring). A systematic approach for the solution of deep groove and angular contact ball bearings and tapered roller bearings has been done by Andreason [7] [8] [9] in which vectors are introduced to describe the geometry, displacements and forces. Andreason's analysis has then been extended by Liu[10] with the high speed effects of roller centrifugal loads and gyroscopic moment.

Then Harris and Kotzalas have published their books [11] [12] where a broad view on the most significant phenomena concerning rolling element bearings is given. They have given a systematic approach to account for almost all rolling element phenomena, (e.g. gyroscopic moment, skewing, stress distributions etc..).

The approach proposed in this work starts from the contact modeling and rolling element behavior to describe the whole bearing behavior under ever less strict assumptions. This approach is adopted in order to allow different analyses, where the compromise between fidelity and computational cost can be chosen by the user. In fact, more fidelity also means typically a computationally more expensive solution.

Concerning contact models, in case of rolling element bearings the contact between the rolling element and the raceways is defined as non-conformal, since the contact print in unloaded configuration has a null area. The non-conformal contact ban be

point contact or line contact depending on the unloaded contact print shape. The point contact is typical of ball bearings, while line contact can be found in roller bearings (e.g. cylindrical, tapered etc.)

The point contact solution neglecting friction has been developed by Hertz [13] which formulations is still largely used to model solid bodies contacting at one point in dry conditions (i.e. no lubricant).

At approximartely the same time, Reynolds described the flow of Newtonian fluids in narrow gaps [14]. The theory of lubrication started. Then it took over 50 years before Ertel [15] and Grubin [16] combined both effects to achieve what is nowadays known as Elastohydrodynamic Lubrication (EHL). Subsequently the solution for EHL point contacts has been tackled with numerical methods, starting from Newton Raphson algorithms (e.g. Hamrock and Dowson [17]) and then introducing more sophisticated methods as multigrid (e.g. Brandt and Livne [18]). Thereafter Wijnant [19] has combined numerical models and curve fitting on the solution in order to develop formulations which describe the steady state and transient lubricated contact behavior.

Line contact modeling presents more complexity due to the bi-dimensionality of the problem, since along the line of contact the approach between the surfaces can be constant or in general non-constant due to misalignment between the cylinder and the plate or even non cylindrical body (e.g. crowned cylinder). In case of finite length cylinders, misalignment etc. the contact is defined as Non-Hertzian, since the assumptions made by Hertz become questionable. To consider misalignment the roller is sliced up in into several slices. Along the length of each slice the penetration between the contacting solid bodies is assumed as constant.

Several methods have been derived to predict the response of the solid near the contact area, given an assumed load distribution (e.g. elliptical in the direction orthogonal to the contact line). Several empirical models exist (e.g. Rothbart[20], Palmgren[21], [22], [23]) as well as analytical solutions based on the constitutive behavior of the solid. The most simple proposed by Weber and Banaschek [24] neglect the coupling between discretized slices and the finiteness of the cylinder (e.g. rollers in roller bearings have finite lengths), whereas the more advanced allow to take this into account, either emipirical (e.g. by Teutsch and Sauer [25]), or analytical (e.g. Reussner [26], Kunert [22]).

To improve the model fidelity, lubrication can be introduced in the model. Several formulas has been developed to predict the fluid film thickness of line contacts under steady state by Moes [27], Gelink and Schipper [28], or even in transient conditions as Sasaki et al. [29] and Rahnejat [30] did. As pointed out by Wiegert et al. [31], many of these rely on superposing analytical solutions to the Reynolds equations for different simple boundary conditions, which may be questionable.

This work starts from both contact models and bearing modeling techniques, and merging them creates a novel approach to describe bearings behavior accounting for the most relevant phenomena (e.g. clearance, centrifugal load, gyroscopic moment etc.). The models proposed in this work allow the evaluation of the bearing response in steady-state conditions in order to achieve a more accurate system-level behavior evaluation.

Part I

Development of Modeling Techniques for Angular Contact Ball Bearings

Chapter 3

Introduction to Angular Contact Ball Bearings Modeling Techniques

This part concerns the development of an high fidelity modeling technique for angular contact ball bearings. In Angular contact ball bearings the inner and the outer raceway are relatively displaced to each other in the bearing axis direction. This allows them to accommodate combined loads, as simultaneous axial and radial loads. The angular contact ball bearing capacity of axial loads carrying increases as the contact angle increases. It is defined as the angle, on the cross-section, between the line along which the contact points lay and the line perpendicular to the bearing axis. Figure 3.1 shown a typical angular contact ball bearing.

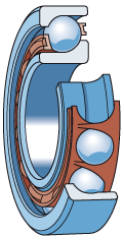

Figure 3.1: Angular Contact Ball Bearing

The high fidelity modeling technique developed starts from the contact modeling to describe the whole bearing behavior. Few contact modeling are introduced in order to increase the fidelity at each step. Each model is improved introducing more physic to it. The first one considers what is called idealized bearing, in which the only phenomena considered is the non linearity coming from the non-conformal contact between the ball and the raceways. Then some geometrical parameters are included, as clearance (axial play) and preload. Due to clearance and preload the bearing internal load distribution changes. The bearing inner ring, rotating provokes the ball rotation around the bearing axis. This rotation induces centrifugal load on the rolling elements. The centrifugal load is then introduced as third model, it increases the model complexity since it cause a loss of symmetry within the bearing.

In order to reduce wear, noises and vibrations in almost all cases, the contact between

the rolling element and the raceways is lubricated. Due to high contact pressure both the lubricant and the solid bodies behavior is complex. Concerning the lubricant behavior, the viscosity changes as the local pressure increases. The viscosity increment induces the solid bodies (ball and raceway) to assume a complex deformation. The effect of lubrication is introduce as fourth model, which represents the most accurate model proposed in this work.

As well as the contact fidelity increases, the computational effort does.

Once that the contact modelings are introduced, a procedure to account for all the rolling element is developed in order to define a law which, for a given inner ring displacement vector gives back the reaction loads on the bearing axis due to the contacts between the rolling element and the raceways.

Chapter 4

Idealized Model

This section illustrates the methods used to develop an idealized model to start from and to move the first steps forward in bearing modeling.

With the adjective *"idealized"* is meant a model where most part of phenomena, clearance, centrifugal load etc. are neglected; In particular the following minor assumptions are made:

- The internal clearance will be neglected at first;
- Dry contact between ball and raceways;
- Negligible dynamic loads;
- Low rotation speed hence negligible centrifugal effects;

And more, in order to justify using the *Hertz contact theory*:

- The proportional limit of the material is not exceeded, that is, all deformation occurs in the elastic range;
- Loading is perpendicular to the surface, that is, the effect of the surface shear stress is neglected;
- The contact area dimensions are small compared with the radii of curvature of the bodies under load;

These last assumptions do not limit the model validity since the contact analyzed fits well in these assumptions.

The classical solution for the local stresses and strains of two elastic bodies *apparently contacting at a single point* was established by Hertz [13] in 1986. Nowadays, contact stresses are frequently called Hertzian or simply Hertz in recognition of his accomplishment.

The above-mentioned assumptions are made in order to allow modeling the ball-raceway contact as a Hertian contact, which gives a convenient solution to the contact problem.

4.1 Dry Contact Model

Figure 4.1 shows the configuration of a rolling element moving on a raceway, in particular the inner one.

As long as we consider the dry contact we will neglect the effects of the lubricant, leaving the discussion for the following chapters.

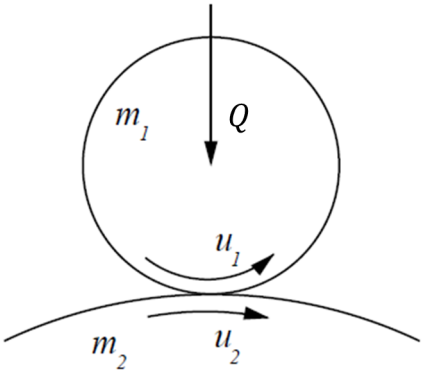

Figure 4.1: Rolling element moving on a raceway.

Due to the applied load Q both solids will deform elastically, forming an elastic contact print or contact area. Since the surfaces have sufficient radii of curvature in all directions, the unloaded contact will be a point, due to this it is defined as a non-conforming contact. The footprint produced by the bodies deformation is in general an ellipse, thus elliptical contact.

Locally, each undeformed surface can be defined by two radius of curvature $R_{k,j}$ along the two principal directions of curvature. In order to model them as an equivalent compliant ellipse contacting an infinite stiff plane, which is exactly what the Hertz theory does, some parameters have to been introduced.

The first introduced parameter is the surfaces curvature ρ, it is defied as:

$$\rho_{k,j} = \begin{cases} \frac{1}{R_{k,j}}, & \text{For } \textit{convex} \text{ surfaces} \\ -\frac{1}{R_{k,j}}, & \text{For } \textit{concave} \text{ surfaces} \end{cases} \tag{4.1}$$

Then for each principal direction of curvature an *equivalent radius of curvature* has to be introduced in order to account for the different curvature of the bodies along the same direction. Since for each principal direction an equivalent radius of curvature can be introduced, the surfaces curvature can be defined by two of them. The first direction is along the rolling element motion direction while the second one lies on the contact plane and is perpendicular to the first one. In this work the convention used to refer to these direction is to use y for the direction with the greater equivalent radius of curvature while with x the one with the minor one.

In ball bearings, the x direction is the motion direction, while the y direction is the perpendicular one, as is shown in Figure 4.2.

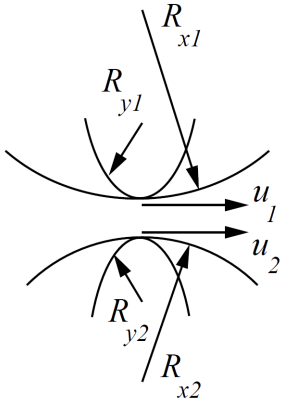

Figure 4.2: Definition of the principal curvature axes.

These assumptions lead to:

$$\frac{R_{j,y}}{R_{j,x}} \geq 1 \tag{4.2}$$

Where the reduced radii of curvature, R_x and y, are defined according to:

$$R_x^{-1} = \rho_{I,x} + \rho_{II,x} \tag{4.3}$$

$$R_y^{-1} = \rho_{I,y} + \rho_{II,y} \tag{4.4}$$

Moreover the following definitions are used:

- *Curvature sum:*

$$\Sigma\rho = \sum_{i,j} \frac{1}{R_{i,j}} = \frac{1}{R_{I,x}} + \frac{1}{R_{I,y}} + \frac{1}{R_{II,x}} + \frac{1}{R_{II,y}} \tag{4.5}$$

- *Curvature difference*

$$F(\rho) = \frac{(\rho_{I,x} - \rho_{I,y}) + (\rho_{II,x} - \rho_{II,y})}{\Sigma\rho} \tag{4.6}$$

4.1.1 Hertzian Solution

Our purpose is to develop a model which describes the ball bearing behavior. It will be based on Hertz contact theory. In this work, nomenclature of *Harris and Kotzalas*[11] is adopted.

In ball bearings, the ball is squeezed between two raceways, which causes two contact point on it; the raceways are defined as the area within the bearing rings where the rolling elements roll. The two raceways have different curvatures. The inner raceway has a *hyperbolic paraboloid* shape, since it is convex in the rolling direction and concave in the perpendicular one. Hence the contact is defined as *sphere-hyperbolic paraboloid* contact. The outer raceway has both rolling direction and the perpendicular one as concave

surfaces, hence this surface is defined as *elliptical paraboloid*. The contact between the rolling element and the outer raceway can be then defined as *sphere-elliptical paraboloid*. In Figure 4.3 is showed the cross-section geometry of the bearing, in order to graphically visualize the problem.

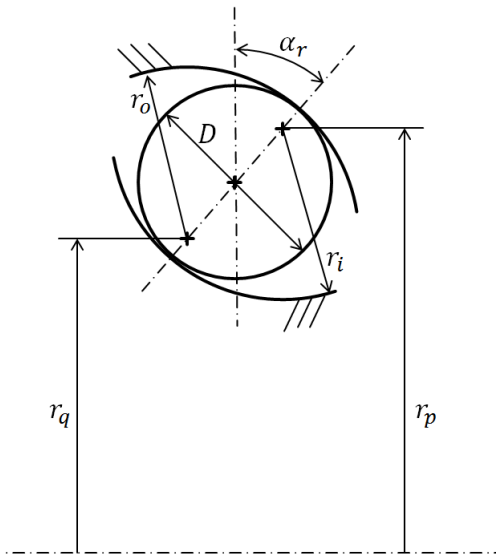

Figure 4.3: Ball bearing cross-section geometry

In this case the *reduced radii of curvature* for the inner-ring and outer-ring contact are defined as follow:

- Inner ring:

$$R_{i,y} = \left(\frac{2}{D} - \frac{1}{r_i}\right)^{-1}, \quad R_{i,x} = \left(\frac{2}{D} + \frac{1}{R_i}\right)^{-1} \tag{4.7}$$

- Outer ring:

$$R_{o,y} = \left(\frac{2}{D} - \frac{1}{r_o}\right)^{-1}, \quad R_{o,x} = \left(\frac{2}{D} - \frac{1}{R_o}\right)^{-1} \tag{4.8}$$

Where R_i and R_o are the effective radii of curvature along the motion direction, naming α_r the effective contact angle (in displaced configuration), they are defined as:

$$R_i = \frac{r_p}{\cos(\alpha_r)} - \frac{D}{2}, \quad R_o = \frac{r_q}{\cos(\alpha_r)} + \frac{D}{2} \tag{4.9}$$

Omitting the theoretical treatise (a complete explanation can be found in [11]), to describe the *Hertz* some parameters still need to be introduced.

Since the solution is given by *elliptical integrals*, introducing the auxiliary quantity $F(\rho)$ as determined by Equation 4.6, this is found to be function of the elliptical parameters **E** and **F** as well as contact contactprints a and b as follows:

$$F(\rho) = \frac{(\kappa^2 + 1)\mathbf{E} - 2\mathbf{F}}{(\kappa^2 - 1)\mathbf{E}} \tag{4.10}$$

where $\mathbf{F}$ and $\mathbf{E}$ are the complete elliptical integrals of the first and the second kind, and κ the elliptical eccentricity parameter. Moreover κ represent also the ratio of a and b respectively, where a is the semimajor axis of the projected elliptic contact surface and b the semiminor one.

Brewe and Hamrock [32], using a least squares method of linear regression, obtained simplified approximations defined as:

$$\kappa \approx 1.0339 \left(\frac{R_y}{R_x}\right)^{0.636} \tag{4.11}$$

$$\mathbf{E} \approx 1.0003 + \frac{0.5968}{\left(\frac{R_y}{R_x}\right)} \tag{4.12}$$

$$\mathbf{F} \approx 1.5277 + 0.6023\ ln\left(\frac{R_y}{R_x}\right) \tag{4.13}$$

For $1 \leq \kappa \leq 10$ the errors in the calculation of these parameter is less than 3%.

In our case both bodies are made of the same material, so it was further determined that [11]:

$$a = a^\star \left[\frac{3Q}{\Sigma\rho}\frac{\left(1-\nu^2\right)}{E}\right]^{1/3} \tag{4.14}$$

$$b = b^\star \left[\frac{3Q}{\Sigma\rho}\frac{\left(1-\nu^2\right)}{E}\right]^{1/3} \tag{4.15}$$

$$\delta = \delta^\star \left[\frac{3Q}{\Sigma\rho}\frac{\left(1-\nu^2\right)}{E}\right]^{2/3} \frac{\Sigma\rho}{2} \tag{4.16}$$

Where δ is the mutual approach of the two bodies in contact and [11]:

$$a^\star = \left(\frac{2\kappa^2\mathbf{E}}{\pi}\right)^{1/3} \tag{4.17}$$

$$b^\star = \left(\frac{2\mathbf{E}}{\pi\kappa}\right)^{1/3} \tag{4.18}$$

$$\delta^\star = \frac{2\mathbf{F}}{\pi}\left(\frac{\pi}{2\kappa^2\mathbf{E}}\right)^{1/3} \tag{4.19}$$

In Harris and Kotzalas [11], values for the dimensionless parameters are given also as tables and as functions of $F(\rho)$.

4.2 Hertz Contact Theory Applied to Angular-Contact Ball Bearings

This section describes both the static ball equilibrium and the kinematics during the displacement of the inner ring with respect to the outer ring.
It is shown how displacement can deeply change the bearing conditions of the individual ball-raceway contacts.

4.2.1 The Ball Equilibrium

In ball bearings the contact between the rolling element and both raceways are point contacts due to the difference between the ball radius and the raceway radius of curvature. That difference is quantified by the *osculation*:

$$f_i = \frac{r_i}{D}, \quad f_o = \frac{r_o}{D} \tag{4.20}$$

To write a simple $\delta - Q$ relation based on the formulation proposed by Harris [11] the constants can be gathered in a single term as follows:

$$K_{qj} = \left[\frac{1}{2} \left(3 \, \frac{1-\nu^2}{E} \right)^{2/3} \delta_j^{\star} \right]^{-3/2} \cdot \Sigma \rho_j^{-1/2} \tag{4.21}$$

The latter equation allows to introduce a more compact formulation:

$$Q_j = K_{qj} \cdot \delta_j^{3/2} \qquad \text{where} \quad j = i, o \tag{4.22}$$

Typical load-deflection curves are shown in figure 4.4, where by the red curve we refer to the ball-outer raceway contact while the blue curve refers to the ball-inner raceway.

In the study-case of a rolling element squeezed between both raceways those contact forces have to satisfy the equilibrium of the ball. As the approach between the ring is given, the rolling element equilibrium can be computed introducing the force equilibrium as follows:

$$\begin{cases} \delta_{tot} = \delta_i + \delta_o \\ Q_i = Q_o \;\rightarrow\; K_{qi} \cdot \delta_i^{3/2} = K_{qo} \cdot \delta_o^{3/2} \end{cases} \tag{4.23}$$

that leads to:

$$\begin{cases} \delta_o = \left[\left(\frac{K_{qo}}{K_{qi}} \right)^{2/3} + 1 \right]^{-1} \cdot \delta_{tot} \\ \delta_i = \delta_{tot} - \delta_o \end{cases} \tag{4.24}$$

and finally:

$$Q = Q_i = Q_o = K_{qi} \cdot \delta_i^{3/2} = K_{qo} \cdot \delta_o^{3/2} \tag{4.25}$$

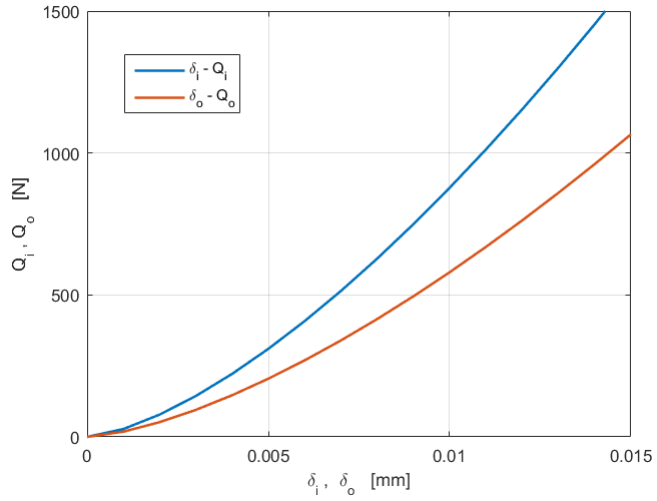

Figure 4.4: Load-Approach curves

Where Q_i and Q_o are respectively the contact force between the inner-raceway or outer-raceway and the rolling element. The ball under load is shown in figure 4.5.
The momentum equilibrium is not necessary yet since the contact forces lays on the same straight line.

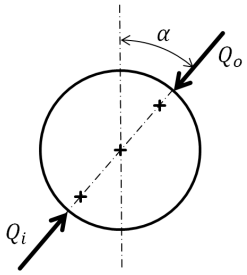

Figure 4.5: The rolling element under load

The computational cost of the solution is nearly zero, since the ball equilibrium is computed without iterative processes, which leads to an efficient and immediate solution.

4.2.2 Internal-Geometry Variation due to Displacement

Displacing the inner-ring changes the contact conditions, the most important variable parameter is the *contact angle* α. It is defined as the angle between the bearing radial direction and the contact-line which is defined as the straight line through the raceways center of curvature as shown in figure 4.6.
The *contact angle* varies from an initial nominal value called α to a real value so called α_r. This change will deeply influence the bearing behavior.

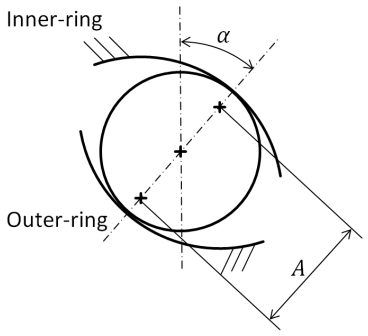

Figure 4.6: The parameter A

The parameter A is the distance between raceway groove curvature centers, also shown in Figure 4.6. In case of contact between bodies, in unloaded conditions his value is:

$$A = (f_o + f_i - 1) \cdot D \tag{4.26}$$

where the first factor is also called *total curvature of the bearing*, then named B:

$$B = f_o + f_i - 1 \tag{4.27}$$

$$A = B \cdot D \tag{4.28}$$

Displacing the inner ring, also displaces its radius of curvature center, due to this, the line where the two centers are located change its slope, which means that the contact angle is no longer equal to the nominal contact angle α.

The *real contact angle* α_r is function of the radial and axial displacement of the inner ring as is shown in figure 4.7 where c_o refers to the outer groove radius of curvature center, c_i the inner one, both in undisplaced configuration, while c_i' is the displaced inner groove radius of curvature center.

The terms δ_a and δ_r are respectively the axial and the radial inner ring displacement while A_r is the distance between raceway groove curvature centers in displaced configuration.

By geometrical considerations, a relation for A_r can be easily written as follows:

$$A_r = \sqrt{(A\cos\alpha + \delta_r)^2 + (A\sin\alpha + \delta_a)^2} \tag{4.29}$$

Furthermore:

$$\alpha_r = \operatorname{acos}\left(\frac{A \cdot \cos\alpha + \delta_r}{A_r}\right) = \operatorname{asin}\left(\frac{A \cdot \sin\alpha + \delta_a}{A_r}\right) \tag{4.30}$$

4.2.3 Clearance and Preload Effects

The clearance is an essential factor in bearing's behavior. Due to it the bearing will present a *free-play* and *free-misalignment*, while the opposite effect is given by the

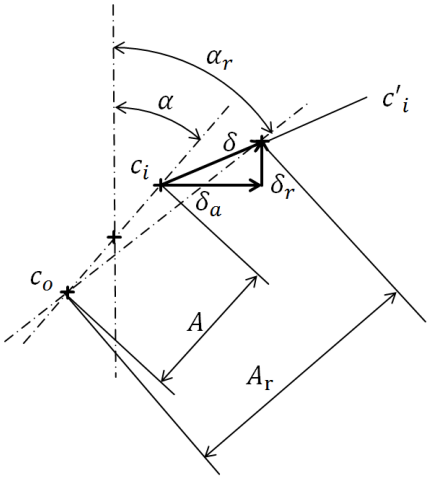

Figure 4.7: Internal geometry while the ball is under load

preload. One of the most important phenomena concerns the load distribution among the rolling elements, as is showed in figure 4.8, where is shown the circular sector ψ_l where the rolling elements get in contact.

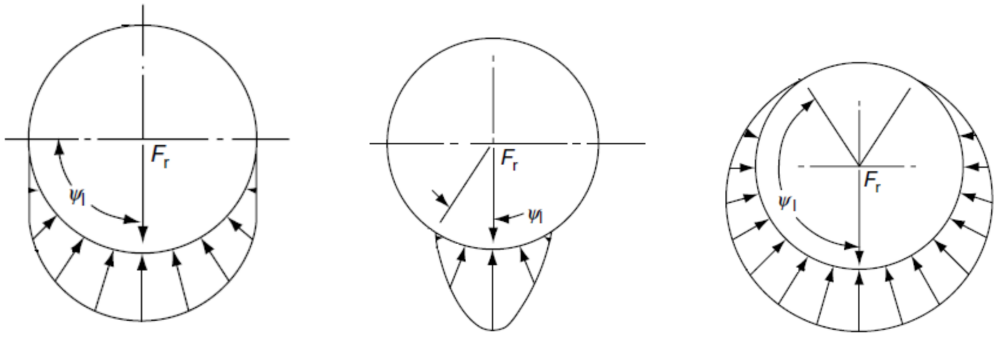

(a) Without *clearance* (and *preload*)

(b) With *clearance*

(c) With *preload*

Figure 4.8: Influence of *clearance* and *preload* on load distribution over rolling elements

Manufacturers data about the *internal clearance* are defined, in case of angular contact ball bearings, using a pair of them and defining the axial play as showed in Figure 4.9.

Since different definitions of clearance exists, in this work the following definition will be adopted: starting form the inner ring position in which the ball and the raceways are in contact, and moving backwards (hence loosing the contacts), the clearance is defined as the maximum axial play allowed between these two configurations. Introducing the *clearance* and *preload* parameters and playing with them, any configuration can be described.

Supposing as nominal configuration the one in which the rolling elements are in

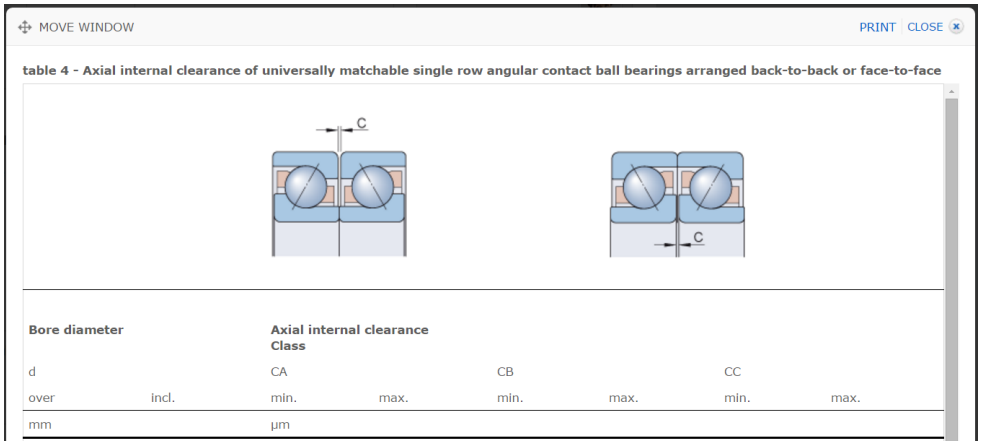

Figure 4.9: Definition of internal clearance by SKF

contact with both raceways and then going backwards is possible to define our initial *contact angle* and the initial arrangement of internal configuration.

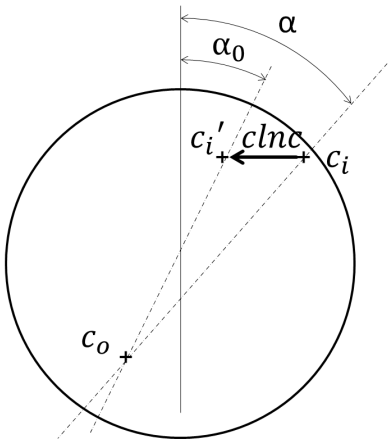

Figure 4.10: Contact angle variation due to axial clearance

The nominal configuration in Figure 4.10 is defined by c_o and c_i where c_o means the center of the outer groove radius of curvature and c_i the center of the inner groove radius of curvature, both in undisplaced configuration. Starting from this position we will impose a negative axial translation of the inner ring as much as the axial *clearance* is. Once mounted, the nominal position of the bearing w.r.t. the clearance will be within this range. Then the contact angle and the distance between the two groove curvature centers are defined as:

$$A_0 = \sqrt{A^2 - 2A\text{sin}\alpha \cdot clnc + clnc^2} \tag{4.31}$$

$$\alpha_0 = \text{acos}\left(\frac{A \cdot \cos\alpha}{A_0}\right) \tag{4.32}$$

The axial preload will be taken into account adding this value to the axial displacement in order to allow for any inner raceway groove curvature center between c_i and c_i'.

When the axial clearance is taken into account, the values of A and α are replaced by the values of A_0 and α_0.

In this way an easy way to distinguish whether the rolling element gets in contact or not is given by:

$$\begin{cases} A_r < BD, & \text{NO Contact} \\ A_r \geq BD, & \text{Contact} \end{cases} \tag{4.33}$$

In case of *deep groove ball bearings* the internal clearance is given as *radial clearance*, it can be easily convert in *axial clearance* by [11] :

$$clnc = 2A \cdot \sin\left(\text{acos}\left(1 - \frac{clnc_r}{2A}\right)\right) \tag{4.34}$$

where $clnc_r$ is the nominal radial clearance. By Eq. 4.34 the technique developed for the angular contact ball bearings can be extended to deep groove ball bearings while in *thrust ball bearings* case the clearance has no reason to exist due to its intrinsic geometry.

4.3 Rolling Element Behavior

This section shows how the rolling element behaves in case of inner ring displacement. Thanks to this model's simplicity the computation is fast and takes negligible time to be computed.

Figure 4.11-*(b)* shows the load as function of δ_r for fixed values of δ_a. Figure 4.11-*(a)* shows the load as function of δ_a and δ_r in a three dimensional plot.

Is clearly visible how below a certain displacement there is no contact between the rolling element and the raceways due to clearance, while when the clearance is totally covered by the displacement the contact occurs.

The *preload* provokes the opposite situation in which also for zero-displacement there is still a certain amount of contact force, this configuration is shown in Figure 4.12.

The second parameter to be investigated is the *real contact angle* α_r which influences the bearing behavior since it represent the contact force direction. The *contact angle* behavior is shown in Figure 4.13 where for low displacement, thus when the rolling element is not yet in contact, the contact angle in not defined.

Is clearly visible how it increases as the axial displacement δ_a increases while it decreases as the radial displacement δ_r decreases.

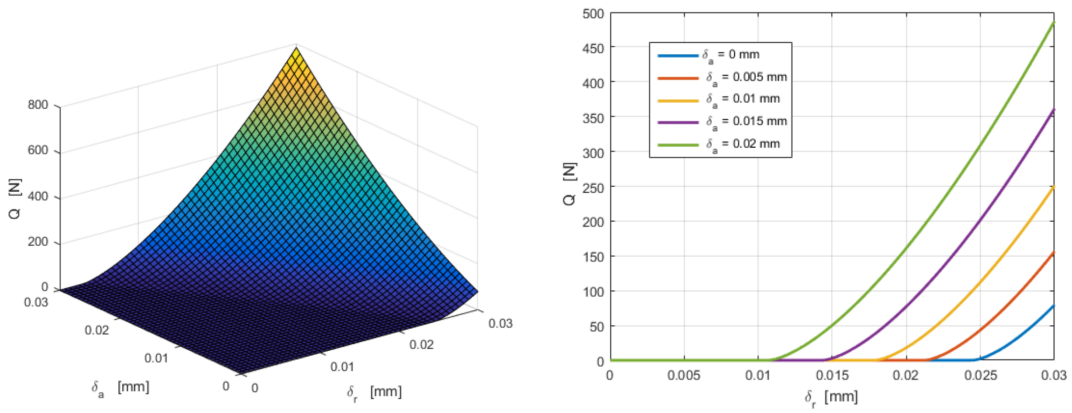

(a) 3D plot (b) 2D plot

Figure 4.11: Load-deflection characteristic curve for a rolling element in case of clearance

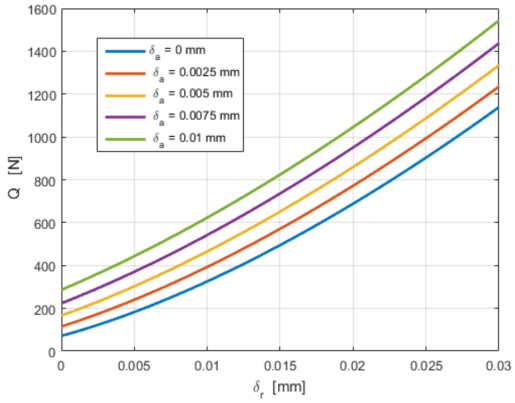

Figure 4.12: Load-deflection characteristic curve for a rolling element in case of preload

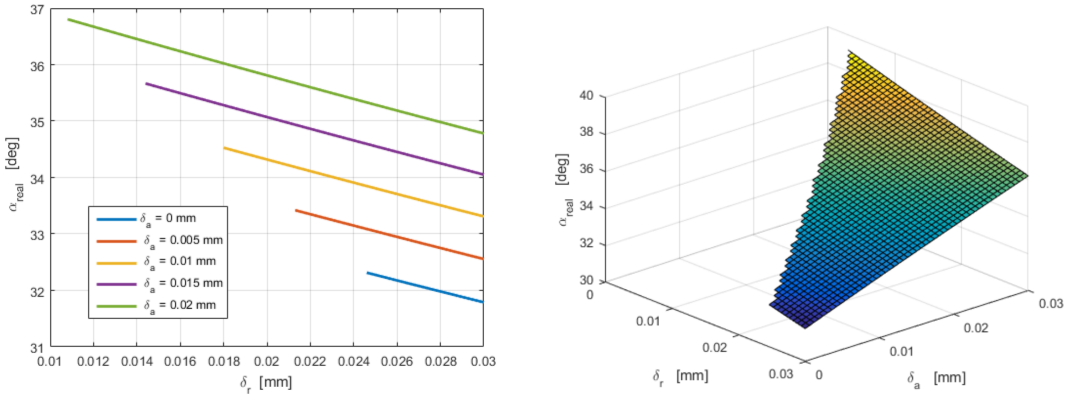

(a) 2D plot (b) 3D plot

Figure 4.13: Influence of *radial* and *axial displacement* on the *contact angle* α_r

Chapter 5

Angular-Contact Ball Bearing Model Accounting for Centrifugal Loads

Since angular-contact ball bearings allows speeds up to few thousands *rpm*; in case of high fidelity methods, which are our aim, centrifugal loads are not negligible since their effect can deeply modify the internal position of the rolling element.

In fact, in case of angular contact ball bearings the *centrifugal load* direction is not aligned with the contact line of action. To achieve the equilibrium, the ball has to assume a configuration where the contact contact angle with the inner and outer ring raceway are different. This configuration can not be defined a priori but requires an iterative process.

This model is substantially based on the work of De Mul et al.[33], though the algorithm used to solve the base problem differs somewhat and the implemented technique takes into account the clearance in a different way compared with what De Mul et al.[33] proposed.

The adopted assumptions made are the same as in Chapter 4 except for the centrifugal load which is no longer neglected.

5.1 Rolling Element Equilibrium

The equilibrium of a rolling element is basically a non-linear, statically indeterminate problem, except for trivial cases.

Since the contact angles between rolling element and both raceways change and due to the non-linearity in the contact location, the solution can not be computed in **closed form**, thus an iterative process has to be used.

As shown in Figure 5.1 the centrifugal load provokes a loss of symmetry, which means that the line of action of the contact resultant forces applied from both raceways on the ball are no more aligned w.r.t. each other.

On the *cross-section*, the ball has 2 *dofs* since the rotational equilibrium is not taken into account since friction is neglected. Therefore the contact forces lines of action have

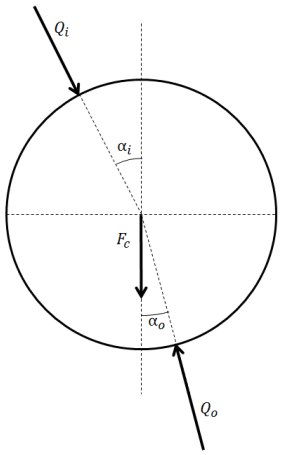

Figure 5.1: Loss of symmetry in rolling element equilibrium.

to pass through the ball center. The ball position in the cross section plane w.r.t. the equilibrium without centrifugal load (computable in exact form) can be described by two independent linear coordinates, v_r and v_a, which are respectively the *radial* and *axial* linear displacement of the ball center.

In order to efficiently figure out the problem, a geometrical representation is needed. Figure 5.2 shows the geometry of the loaded and displaced equilibrium.

Table 5.1 lists and explains the meaning of the points and lines shown in Figure 5.2.

C_o	Outer-ring curvature center (Fixed)
C_s	Rolling element center
C'_s	Rolling element center (Displaced)
C_i	Inner-ring curvature center
C'_i	Inner-ring curvature center (Displaced)
l_o	Distance between ball center and C_o
l_{0_o}	Distance between ball center and C'_o
l_i	Distance between ball center and C_i
l_{0_i}	Distance between ball center and C'_i
α_o	Outer ring-ball contact angle
α_i	Inner ring-ball contact angle

Table 5.1: List of Symbols of Figure 5.2

The ball equilibrium without centrifugal load can be calculated as Chapter 4 describes.

Introducing the centrifugal load the ball center is no longer located on the contact line connecting inner and outer ring groove centers.

The aim is now to describe the rolling element location by two variables (since it has

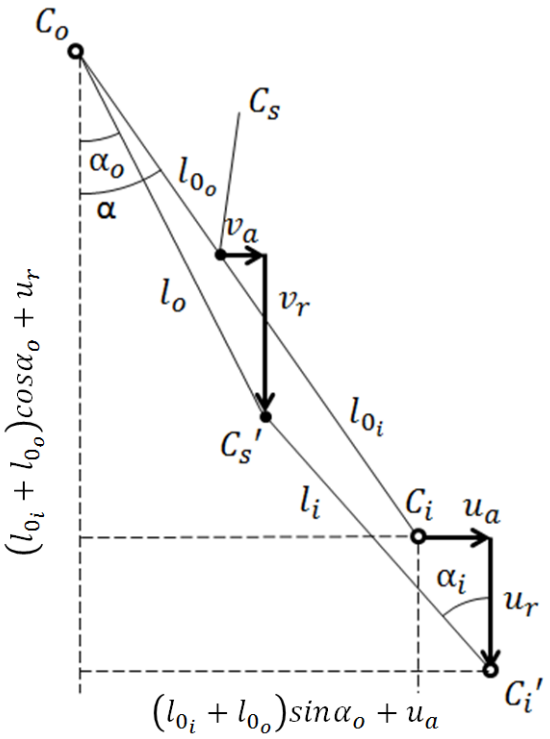

Figure 5.2: Positions and displacements of groove centers and ball center in the cross section when centrifugal load occurs.

2-dof). Indeed the most suitable variables are the location on the cross-section plane of the ball's center w.r.t. the unloaded configuration, so called v_a and v_r.

To align the procedure with what De Mul et al. have done in [33], the equations have to be pre-processed. In fact the clearance definition adopted in this work is more accurate since it is based on a single value (retrievable from catalogs) instead of two values (radial and axial).

Starting from the loaded configuration without ball centrifugal load we can define an *equivalent penetration and contact angle*. Through the model proposed in Chapter 4 the rolling element equilibrium can be easily computed (neglecting centrifugal load) therefore the penetration between ball and both raceways, δ_i and δ_o from Eq. (4.25), as well as the real contact angle α_r from Eq. (4.30).

Assuming then α_r as nominal contact angle, the *equivalent axial and radial* inner-ring displacement can be computed as follows:

$$\begin{cases} u_a = (\delta_i + \delta_o) \cdot \sin\alpha_r \\ u_r = (\delta_i + \delta_o) \cdot \cos\alpha_r \end{cases} \tag{5.1}$$

In this way the clearance is taken into account as explained in Chapter 4, rephrasing the problem in an equivalent way which allows to use what proposed in [33]. In fact the rolling element is being unloaded along the line of action defined by α_r.

The above-mentioned procedure leads to assume that the α angle in Figure 5.2

corresponds to α_r calculated neglecting the centrifugal load and $\mathbf{u} = [u_r \; u_a]^T$ as from Eq. 5.1.

Referring to Figure 5.2 the following geometric relationships apply[33]:

$$tan\alpha_i = \frac{l_{0_i}\text{sin}\alpha_r + u_a - v_a}{l_{0_i}\text{cos}\alpha_r + u_r - v_r} \tag{5.2}$$

$$tan\alpha_o = \frac{l_{0_o}\text{sin}\alpha_r + v_a}{l_{0_o}\text{cos}\alpha_r + v_r} \tag{5.3}$$

$$l_i = \left[\left(l_{0_i}\text{cos}\alpha_r + u_r - v_r\right)^2 + \left(l_{0_i}\text{sin}\alpha_r + u_a - v_a\right)^2\right]^{1/2} \tag{5.4}$$

$$l_o = \left[\left(l_{0_o}\text{cos}\alpha_r + v_r\right)^2 + \left(l_{0_e}\text{sin}\alpha_r + v_a\right)^2\right]^{1/2} \tag{5.5}$$

$$\delta_i = l_i - l_{0_i} \tag{5.6}$$

$$\delta_o = l_o - l_{0_o} \tag{5.7}$$

Combining Eq. (5.6) and (5.7) with Eq. (4.22) the contact forces Q_i and Q_o due to ball-raceways penetrations can be easily computed.

The third force acting on the rolling element is the *centrifugal force* due to the revolution of the rolling element around the bearing axis. This force can be immediately calculated as follows:

$$F_c = m_b \cdot r_{pw} \cdot \omega_{pw}^2 \tag{5.8}$$

where ω_{pw} is the rotational velocity of ball center around the bearing axis, m_b the mass of the ball and r_{pw} the pitch diameter. Since the shaft speed ω_{shaft} instead of ω_{pw} is given as input, a relation between these two variables is needed.

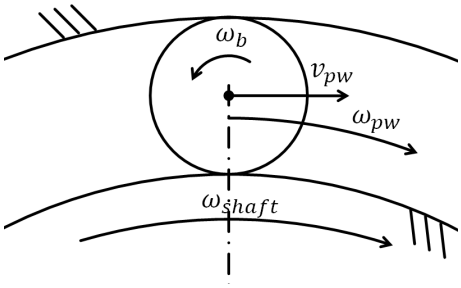

Figure 5.3: Representation of ball and inner-ring velocity.

As first approximation (not that far from reality) it is assumed that the ball-raceways contacts are constantly without sliding, therefore referring to Figure 5.3:

$$\omega_b \cdot D = \omega_{shaft} \cdot \left(r_p - \frac{D}{2}\,\text{cos}\alpha_r\right) \tag{5.9}$$

$$v_{pw} = \omega_b \cdot \frac{D}{2} = \omega_{pw} \cdot r_{pw} \tag{5.10}$$

combining (5.9) with (5.10) in order to eliminate ω_b, leads to the relation between ω_{pw} and ω_{shaft} as follows:

$$\omega_{pw} = \frac{r_p - D/2\ \cos\alpha_r}{2\ r_{pw}}\omega_{shaft} \tag{5.11}$$

Now that the three forces have been defined, the rolling element equilibrium can be formulated as follows (see Figure 5.1):

$$\mathbf{f} = \begin{bmatrix} F_r \\ F_a \end{bmatrix} = \begin{bmatrix} Q_i\cos\alpha_i - Q_o\cos\alpha_o + F_c \\ Q_i\sin\alpha_i - Q_o\sin\alpha_o \end{bmatrix} = \begin{bmatrix} 0 \\ 0 \end{bmatrix} \tag{5.12}$$

which is a set of non linear equations, where $\mathbf{f}$ represents the vector of the residual forces in each iteration step while the unknown is the ball center position vector $\mathbf{v} = [v_r\ v_a]^T$; to solve Eq. (5.12) a *Newton-Raphson method* can be introduced, which gives the following iterative process:

$$\mathbf{v}_{k+1} = \mathbf{v}_k - \mathbf{J}_k^{-1}\mathbf{f}_k \tag{5.13}$$

where $\mathbf{J}_k$ is the *Jacobian matrix* for the *k-th* iteration step. It is defined as follows:

$$\mathbf{J} = \begin{bmatrix} \dfrac{\partial F_r}{\partial v_r} & \dfrac{\partial F_r}{\partial v_a} \\ \dfrac{\partial F_a}{\partial v_r} & \dfrac{\partial F_a}{\partial v_a} \end{bmatrix} \tag{5.14}$$

where (see [33]):

$$\frac{\partial F_r}{\partial v_r} = -\frac{\partial Q_i}{\partial \delta_i}\mathrm{c}^2\alpha_i - \frac{Q_i}{l_i}\mathrm{s}^2\alpha_i - \frac{\partial Q_o}{\partial \delta_o}\mathrm{c}^2\alpha_o - \frac{Q_o}{l_o}\mathrm{s}^2\alpha_o \tag{5.15}$$

$$\frac{\partial F_a}{\partial v_r} = \frac{\partial F_r}{\partial v_a} = -\frac{\partial Q_i}{\partial \delta_i}\mathrm{s}\alpha_i\mathrm{c}\alpha_i + \frac{Q_i}{l_i}\mathrm{s}\alpha_i\mathrm{c}\alpha_i - \frac{\partial Q_o}{\partial \delta_o}\mathrm{s}\alpha_o\mathrm{c}\alpha_o + \frac{Q_o}{l_o}\mathrm{s}\alpha_o\mathrm{c}\alpha_o \tag{5.16}$$

$$\frac{\partial F_a}{\partial v_a} = -\frac{\partial Q_i}{\partial \delta_i}\mathrm{s}^2\alpha_i - \frac{Q_i}{l_i}\mathrm{c}^2\alpha_i - \frac{\partial Q_o}{\partial \delta_o}\mathrm{s}^2\alpha_o - \frac{Q_o}{l_o}\mathrm{c}^2\alpha_o \tag{5.17}$$

Where the abbreviation s and c are applied to respectively sin and cos to streamline the notation. Applying Eq. (4.22) to both contacts, leads to:

$$\frac{\partial Q_i}{\partial \delta_i} = \frac{3}{2}\cdot K_i \cdot \delta_i^{1/2} \tag{5.18}$$

$$\frac{\partial Q_o}{\partial \delta_o} = \frac{3}{2}\cdot K_o \cdot \delta_o^{1/2} \tag{5.19}$$

The method has a quadratic convergence rate and having a sufficient accurate guess value to start from, the method will converge in almost all cases due to the monotonic set of equations to be solved.

The method breaks down when the rolling element is not or just barely in contact. This reduce the *Jacobian* to a badly conditioned, singular or even null matrix. When this

happens, the new solution vector obtained in the next iteration step becomes extremely large and physically meaningless. To avoid this solution behavior a *"damped" Jacobian matrix* is used. This is roughly achieved limiting the amplitude of the Jacobian changes at each step w.r.t. the previous one. This prevent possible solution singularity.

5.2 Rolling Element Behavior

This section shows how the rolling element behaves when a load (in terms of displacement) is given to the inner raceway varying the shaft speed.

The behavior is shown introducing a fixed axial displacement of the inner ring δ_a and then an increasing radial displacement δ_r. Different curves are plotted on the same picture in order to illustrate how the shaft speed influences the solution, in particular the contact angles.

The first result shown is the contact load in Figure 5.4 where the axial displacement has been set as:

$$\delta_a = 0.01 \ mm \tag{5.20}$$

while three different shaft speeds are imposed, respectively at 0, 5000, 10000 *rpm*.

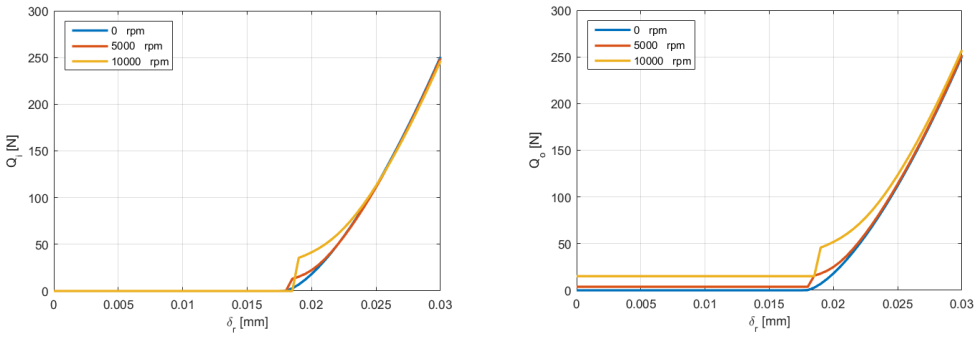

(a) Inner raceway-ball contact force

(b) Outer raceway-ball contact force

Figure 5.4: Contact forces behavior

The loading process is composed by three different parts:

- *First part:* there is no contact between on the inner raceway so the centrifugal load is carried by the outer raceway contact. Because of this missed contact, there is no contact force on the inner raceway while a constant force is applied on the outer one.
- *Second part:* the rolling element gets in contact also with the inner raceway. It is clearly visible how this provokes a discontinuity. This behavior will be fully explained later.
- *Third part:* the rolling element is significantly loaded, so the centrifugal load becomes negligible w.r.t. contact forces such that the rolling element behaves similar to the 0 *rpm* case.

The discontinuity can be explained by looking in detail what happens during the radial displacement. At the beginning the rolling element does not get in contact with the inner raceway. Then increasing δ_r the point in which the rolling element would be in contact, if one were to neglect the centrifugal load, occurs. Due to contact deformation between the ball and the outer raceway it looses contact. Finally when this deformation is compensated by δ_r the rolling element suddenly restores its oblique contact angles. Due to this both the contact angles have to change in order to compensate for the centrifugal load, which provokes an increment of penetration on both raceways, leading to the abrupt *step* clearly visible in Figure 5.4.

The penetration evaluation comes from Hertz theory (4.22) and it is showed in Figure 5.5 where is still clearly visible the discontinuity above-mentioned and the three parts already explained.

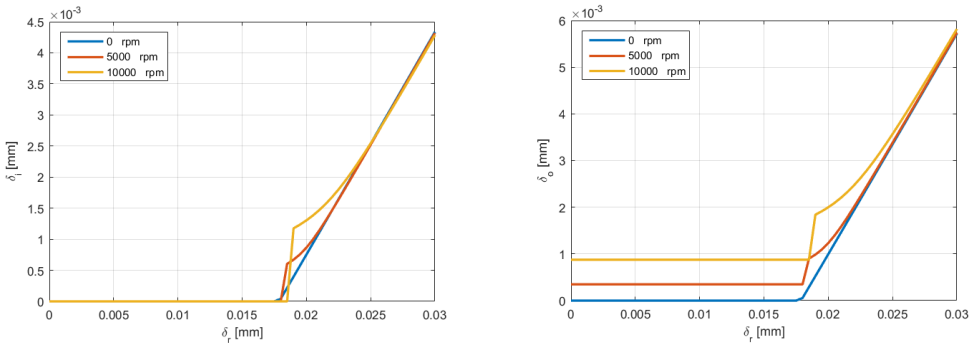

(a) Inner raceway-ball penetration (b) Outer raceway-ball penetration

Figure 5.5: Penetrations behavior

The second parameters to investigate are the contact angles, which are showed in Figure 5.6. In fact, due to centrifugal load, they are no longer identical since they have to balance the centrifugal effect.

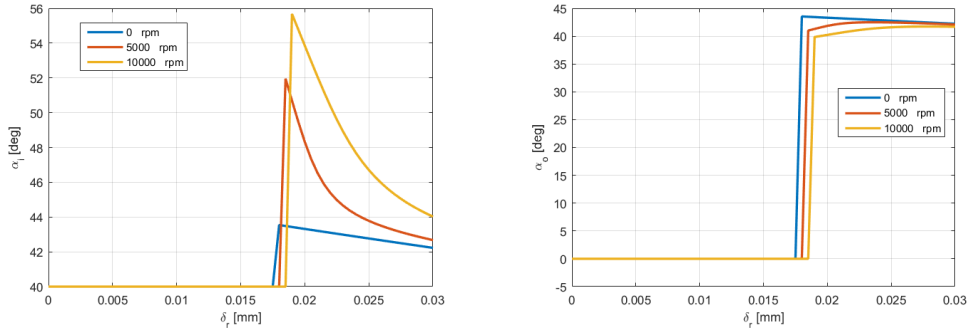

(a) Inner raceway-ball contact angle (b) Outer raceway-ball contact angle

Figure 5.6: Contact angles behavior behavior

Concerning these parameters the three parts are still the same but they have brought different behaviors shown in Figure 5.6 and they can be explained as:

- *First part:* due to the missed ball-inner raceway contact, the rolling element locates itself in a configuration in which $\alpha_o = 0\ deg$ while the inner contact angle is undefined since there is no contact, therefore the nominal value is displayed. This is a configuration where $\alpha_o = 0\ deg$ allows the outer ring to carry the whole centrifugal load.
- *Second part:* the ball gets in contact with both raceways; α_o set itself to a value less than the nominal value in order to carry the centrifugal load, while α_i becomes greater than the nominal value in order to satisfy the ball equilibrium.
- *Third part:* as already explained, the more the rolling element is loaded, the more the centrifugal load becomes negligible w.r.t. the contact forces, thus both variables approximate the behavior of the 0 rpm case.

Chapter 6

Rolling Element Behavior Accounting for Lubrication

In this chapter, the previously presented modeling technique, is extended to account for lubrication. Lubricated contact models require more computational effort due to their intrinsic complexity. Since almost all bearings work in lubricated conditions this will give a additional value to our modeling techniques and moreover a considerable increment of fidelity.

In case of ball bearings, usually the contact requires to be modeled as *elastohydrodynamic (EHL)* which leads to a more reliable model in terms of behavior prediction, on the other hand more sophisticated algorithms are involved which raise the computational effort.

The EHL regime occurs when, due to the contact pressure distribution both the lubricant piezoviscosity and the solid compliance cannot be neglected, the EHL regime is the opposite of the rigid-isoviscous regime in which both the bodies compliance and the lubricant piezoviscosity are neglected.

The model used in this work is based on the work of Wijnant [19] which developed a *dimensionless equation* describing the contact behavior. Such equation is established solving the *Reynolds* [14] and *Film Thickness* equations combining *multigrid* and *multilevel* methods and then a curve is fitted to approximate the behavior by a single dimensionless equation.

6.1 Elliptical EHL Contact

Almost all rolling bearings work under lubricated conditions, therefore adding the physics related to lubrication to the model, also the prediction will be more reliable.

In case of *non-conformal point contact* the contact behavior can no longer be modeled as rigid-isoviscous and studying the contact by an hydrodynamic analysis only, immediately shows why. In fact solving the *Reynolds equation* for point-contact in steady-state condition, neglecting body elasticity and lubricant piezoviscosity, the pressure field obtained has a high peak already for relatively low speed. This peak easily reaches a value which brings to non-negligible bodies deformation and non-negligible

lubricant viscosity variation.

When both bodies' elasticity and lubricant piezoviscosity are of importance, the regime is called *Elastohydrodynamic Lubrication (EHL)*.

Figure 6.1 shows the typical pressure distribution and film thickness in *elliptical EHL contact*. The pressure in the contact closely resembles the Hertzian semi-ellipsoidal distribution. It deviates from this distribution in the inlet region and in the outlet region of the contact. In the inlet region the pressure has a smoother distribution instead of the discontinuity in the pressure gradient occurring for dry contacts. In the outlet part a pressure peak occurs, known as *"pressure spike"*. The spike is a consequence of the exponential increase of the viscosity with pressure. Its height depends on the density and consequently on the density-pressure relation that is used, when studying it by means of numerical simulation.

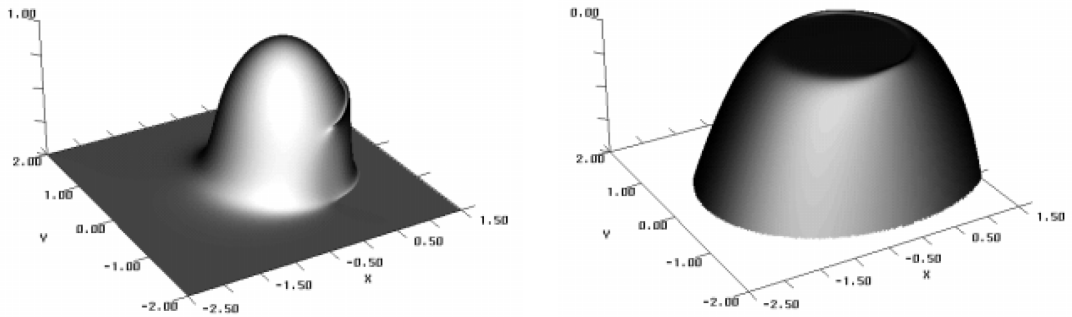

(a) *Pressure distribution* (b) *Film thickness distribution*

Figure 6.1: Pressure and Film thickness distribution in elliptical EHL contact [19] (Inlet: $x < 0$, Outlet: $x > 0$)

Figure 6.2 shows an interference plot which clearly shows how the film thickness distribution is *horseshoe-shaped* where the narrower part is located at the outlet provoking the pressure spike.

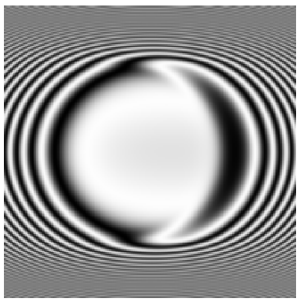

Figure 6.2: Typical interference plots of film thickness [19] (Inlet: left, Outlet: right)

Beyond the increased fidelity, there is a second important goal why EHL phenomena have to be introduced in the modeling technique. The contact stiffness in lubricated contacts is a continuous function, as Figure 6.3 shows, while in case of dry contact

it has a discontinuous behavior. The stiffness function in EHL regime, reaches zero asymptotically for infinite separation of the surfaces.

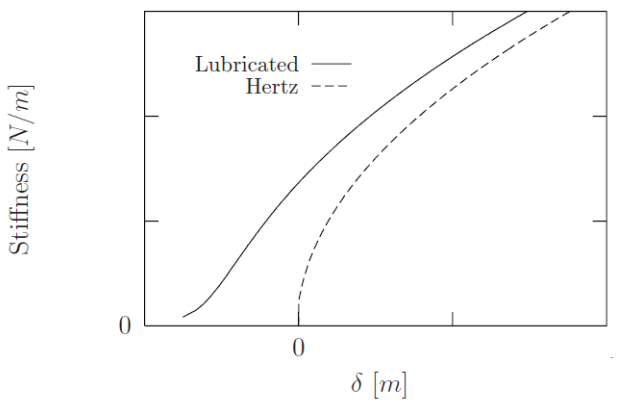

Figure 6.3: Stiffness of the EHL contact compared to the Hertzian stiffness [19]

The *dimensionless parameters* used to describe the contact behavior, are defined in the work of Wijnant [19] using a powerful tool to obtain similarity groups for a given set of equations. It is so-called *optimum similarity analysis*, as presented by Moes [27], which ensures the minimal number of independent parameters.

The bodies' behavior and the contact surfaces are defined by the same parameters as in case of *dry contact*: respectively E_{eq} and the *reduced radius of curvature* of the surfaces.

$$E_{eq} = \left(\frac{1-\nu^2}{E}\right)^{-1} \tag{6.1}$$

$$R_{k,eq} = \left(R_{k,x}^{-1} + R_{k,y}^{-1}\right)^{-1} \tag{6.2}$$

The *Barus*[34] function is introduced to describe the lubricant piezoviscosity.

$$\eta = \eta_0 e^{\alpha_{barus} p} \tag{6.3}$$

Where η_0 is the viscosity at ambient pressure and α_{barus} is the pressure-viscosity coefficient.

In case of steady-state contact conditions the dimensionless parameters to be introduced are [19]:

$$N = \left(\frac{R_{k,x}}{R_{k,y}}\right)^{0.5} \frac{Q}{E_{eq} R_x^2} \left(\frac{E_{eq} R_{k,x}}{\eta_0 u_s}\right)^{3/4} \tag{6.4}$$

$$L = \alpha_{barus} E_{eq} \left(\frac{\eta_0 u_s}{E_{eq} R_x}\right)^{1/4} \tag{6.5}$$

$$\Delta = \delta / c \tag{6.6}$$

Where:

$$c = \frac{b^2}{2R_{eq}} \cdot \frac{\mathbf{F}}{\mathbf{E}} \tag{6.7}$$

and:

$$b = \left(\frac{3QR_{eq}}{E_{eq}}\right)^{1/3}\left(\frac{2\mathbf{E}}{\kappa\pi}\right)^{1/3} \tag{6.8}$$

The solution for elliptical contact is then formulated as follows[19]:

$$\Delta(N,L) = 1 - p(L)N^{q(L)} \quad \text{where} \tag{6.9}$$

$$p(L) = \left((4-0.2L)^7 + (3.5+0.1L)^7\right)^{1/7} \tag{6.10}$$

$$q(L) = -\left(0.6 + 0.6\,(L+3)^{-1/2}\right) \tag{6.11}$$

Which leads to the contact behavior in Figure 6.4 which clearly shows the asymptotic characteristic of the EHL contact.

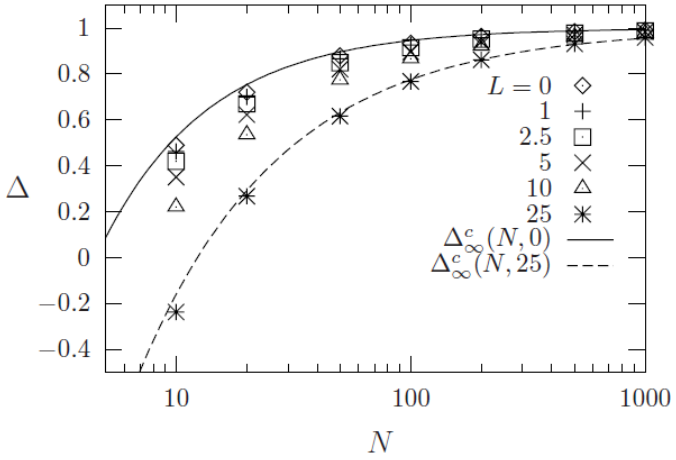

Figure 6.4: Δ as a function of N for different values of L [19]

6.2 Rolling Element Equilibrium in EHL

The model developed by Wijnant is a powerful tool since it describes the coupled effect of the lubricant and the solid bodies. The issue gets more complicated when the equilibrium of a rolling element has to be computed. In this case the input is no more the load Q but the sum of ball-inner and outer ring penetration. In case of dry contact the relationship between both penetrations is computed easily. In this case, it is not possible to manipulate Eq. (6.9) in order to obtain the penetration as function of the load. This means that to solve the rolling element equilibrium three iterative processes have to be involved; two parallel ones to calculate the load Q for a given penetration δ within a third higher-level iterative process to compute the ball center position.

Contact Solution To compute the contact solution, the first step to be moved is to expand Eq. (6.9) and then collect the unknown Q in order to separate the constant part of the formula from the unknown. It reads:

$$\frac{\delta_j}{Q^{2/3} C_C} \;=\; 1 - p(L)\,[Q\;C_N]^{q(L)} \tag{6.12}$$

where C_C and C_N are constant defined as:

$$C_C \;=\; \frac{\left[\left(\frac{3R_{eq}}{E_{eq}}\right)^{1/3}\left(\frac{2\mathbf{E}}{\kappa\pi}\right)^{1/3}\right]^2 \cdot \mathbf{F}}{2R_{eq}\cdot\mathbf{E}} \tag{6.13}$$

$$C_N \;=\; \left(\frac{R_{k,x}}{R_{k,y}}\right)^{0.5} \frac{1}{E_{eq}R_x^2}\left(\frac{E_{eq}R_{k,x}}{\eta_0 u_s}\right)^{3/4} \tag{6.14}$$

therefore δ is defined as:

$$\delta \;=\; Q^{2/3}\;C_C\left[1 - p(L)\,(Q\;C_N)^{q(L)}\right] \;=\; Q^{2/3}\;C_C - p(L)C_C C_N^{\;q(L)}\;Q^{q(L)+2/3} \tag{6.15}$$

The above mentioned function has to be solved using an iterative method. Therefore the *Newton-Raphson* method is used. Moving δ on the right-hand side, the function to solve can be defined as follows:

$$f(Q) \;=\; Q^{2/3}\;C_C - p(L)C_C C_N^{\;q(L)}\;Q^{q(L)+2/3} - \delta \;=\; 0 \tag{6.16}$$

In order to define the solving routine, $\partial f/\partial Q$ has to be defined:

$$f'(Q) \;=\; \frac{\partial f}{\partial Q} \;=\; \frac{2}{3}Q^{-1/3}\;C_C - \left(q(L) - \frac{1}{3}\right)p(L)\;C_C\;C_N^{q(L)-1/3} \tag{6.17}$$

The resulting Newton-Raphson method reads:

$$Q_{k+1} = Q_k - \frac{f(Q_k)}{f'(Q_k)} \tag{6.18}$$

This procedure is implemented for both contacts (*inner* and *outer*) since the higher-level routine computing the ball position defines the contact penetration between the rolling element and the raceways. Once the penetration is defined, the load on each contact is computed by Eq. (6.18).

In this case, the Jacobian does not need to be modified (e.g. damped), since even for negative penetration a certain amount of stiffness is still present. This also helps the solution convergence.

Rolling element equilibrium The procedure to compute the rolling element equilibrium is exactly the same as proposed in Chapter 5. In particular the Eq. (5.14)(5.15)(5.16) and (5.17) can be still used where Q_i and Q_o are computed through the two lower-level loops by Eq. (6.18). The partial derivatives $\partial Q_i/\partial\delta_i$ and $\partial Q_o/\partial\delta_o$ are defined by deriving Eq. (6.15) w.r.t. Q and then calculating the inverse, which leads to:

$$\frac{\partial Q}{\partial\delta} \;=\; \left(\frac{\partial\delta}{\partial Q}\right)^{-1} \;=\; \left[\frac{\partial f}{\partial Q} \;=\; \frac{2}{3}Q^{-1/3}\;C_C - \left(q(L) - \frac{1}{3}\right)p(L)\;C_C\;C_N^{\;q(L)-1/3}\right]^{-1} \tag{6.19}$$

Tolerances Particular attention has to be payed to the tolerances of Newton-Raphson methods. The fact that two loops have to be computed within another one is risky in terms of numerical stability since the higher-level loop iterates using approximates solutions. If the tolerance of the lower-level loops is not correctly scaled w.r.t. the higher-level loop tolerance at each step, the rolling element equilibrium will be influenced by the contact force solution compromising the method convergence. Usually in such a case the tolerance of the lower-level loops is set at least one order of magnitude smaller than the tolerance of the higher-level loop in order to avoid numerical instabilities; in the specific study-case, after several tests, it was fixed as three order of magnitude smaller since this is a good compromise between numerical stability and convergence speed.

Concerning the ball equilibrium the tolerance is based on the centrifugal load value, which is defined as:

$$tol_b \;=\; F_c \cdot scf \tag{6.20}$$

where scf is the centrifugal load scale factor, suggested as $1 \cdot 10^{-6}$. In case of low speeds, $toll_b$ is replaced with a constant value. Therefore since the tolerance tol_b has the dimension of a force, it is not directly comparable with the function $f(Q)$. Thus, in order to derive the tolerance in the units of a force, the error penetration function $f(Q)$ needs to be scaled with the quantity $f'(Q)^{-1}$ of which the dimension correspond to that of a stiffness. Which leads to:

$$tol_c \;=\; \frac{f(Q)}{f'(Q)} \cdot scf \cdot scf_c \tag{6.21}$$

where scf_c has to be at least 10^{-1}.

Relative surfaces speed In order to compute the solution, the mutual surfaces speed has to be calculated since the contact load is a function of it. The only speed which plays a role in this solution is the sum of speeds, which means that only the Poiseuille flow is taken into account (sqeeze). Hence the slipping is neglected.

Referring to Figure 5.3 and still considering the outer ring fixed, the sum velocity u_{s_o} and u_{s_i} can be written as follow:

$$u_{s_o} = 2\omega_{pw}\; R_o \tag{6.22}$$

$$u_{s_i} = 2\left(\omega_{shaft} - \omega_{pw}\right)\; R_i \tag{6.23}$$

6.3 Rolling Element Behavior in EHL

This section shows the rolling element behavior when a certain displacement is given to the inner ring. A smoother behavior is expected, compared with the one obtained in Chapter 5 since the function characterizing the lubricated contact has a continuous behavior.

In the case shown here, the axial displacement is fixed at $\delta_a = 0.015\ mm$, then three different rotational speeds are imposed, 0, 5000 and 10000 rpm, while the radial displacement δ_r is kept as a variable. Figure 6.5 shows the contact load behavior. As

expected the behavior is smooth and without any discontinuity thanks to lubrication. Moreover, comparing this behavior with Figure 5.4, it can be seen how in this model the shaft speed plays a key role even for high loads, since it increases the lubricant effects on the contact spots due to the faster squeezing of the lubricant. Thus the curves for different speeds are not converging as the penetration increases.

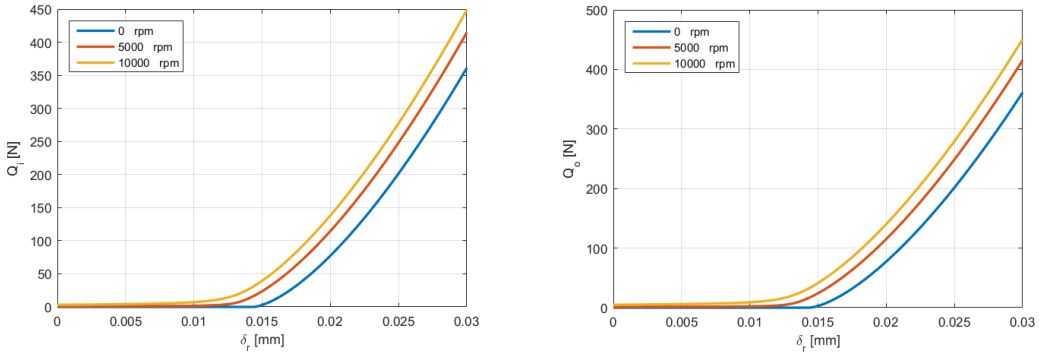

(a) *Inner raceway-ball contact force* (b) *Outer raceway-ball contact force*

Figure 6.5: Contact forces behavior

The second parameters to be evaluated are the contact angles which significantly influence the bearing behavior. Similar to the contact force, a totally smooth behavior is expected. They are shown in Figure 6.6.

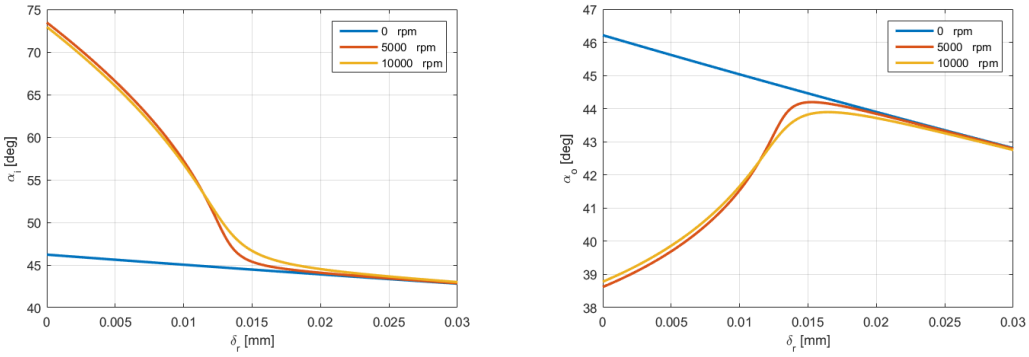

(a) *Inner raceway-ball contact angle* (b) *Outer raceway-ball contact angle*

Figure 6.6: Contact angles behavior

For high penetrations the static and the high speed solutions for contact forces are not converging, while the contact angles do. This is due to the centrifugal load which becomes negligible compared with the contact forces.

Introducing lubrication, in case of negative penetration (no contact in case of the dry model) the rolling element does not assume the configuration $\alpha_o = 0°$ since the zero contact load condition can not occur due to lubrication. This indeed leads to a

smoother behavior and a more reliable contact model. On the other hand these results come at higher computational cost which could be prohibitive in some cases. Moreover could also be that this kind of accuracy is not required, especially because it already represents an improvement with respect to current commonly used modeling techniques.

The above-mentioned means that even if this is the most accurate modeling technique developed in this work, the one developed in Chapter 5 is still useful since it requires a low computational effort and depending case by case its accuracy could be more than enough.

Chapter 7

Angular Contact Ball Bearing Behavior

Contact modeling and rolling element equilibrium are computed using the procedures and the models described in the previous chapters. The next step is to develop a rigorous method to compute the whole bearing equilibrium for a given inner ring displacement.

This section explains the procedure which allows to evaluate the bearing behavior. It is based on the contact modeling and rolling element equilibrium described in the previous chapters.

The output is the vector of the total force and moment interaction between the inner and outer raceway. The procedure to compute the solution can be divided in the following steps:

1. From the global inner ring displacement, the displacement at the location of each single rolling element is calculated;

2. The rolling element equilibrium is then computed by non-conformal contact modeling. This step is the process bottle-neck since it is the more time-consuming. This step gives the contact loads on each individual rolling element due to the local inner ring displacement;

3. Once all the contact loads between the rolling elements and the inner ring are computed, they have to be referred to the global coordinate system (on the bearing axis) and then summed.

To limit the complexity of the analysis, the following major assumptions are made:

- As bearings are frequently mounted in sturdy shafts and in robust housings, "structural" deformation of the bearing rings is neglected and only elastic deformation associated with the concentrated contacts in the bearing is considered;

- Generally, friction in bearings is low and negligible compared to the raceway and flange normal loads on the rolling elements;

- Loads generated by interaction from the cage are negligible.

At the end a procedure has to be written which first performs a transformation from the coordinate system of the bearing to the coordinate system of the rolling element, in order to calculate the local displacements, and then a procedure which transforms the contact forces from the rolling element coordinate system to the coordinate system of the bearing.

7.1 From Rolling Element to Bearing Behavior

This section describes the procedure to determine from the *displacement* and *tilting* of the inner w.r.t. the outer raceway, the inner-ring's displacement in each single rolling element location, and then to merge each rolling element contribution.
Once this technique is developed it is used for all the ball bearing models further studied. This is done by a kinematics-based procedure.

The strong point of this method resides in his simplicity; because of this the computation will be elegant and efficient.

Two distinct right-handed Cartesian coordinate system are defined; the first one fixed in space and so called *global* which has the z-axis along the bearing's axis and a local coordinate system for each rolling element as shown in Figure 7.1.

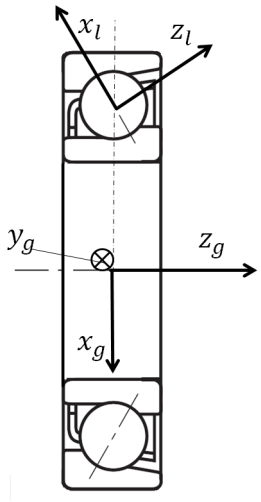

Figure 7.1: The global and the local coordinate system

7.1.1 From the Global Displacement to the Local One

Since the inputs are the inner ring translations and tiltings along the *global axes*, the first step is to convert the displacement of the inner ring w.r.t. the *global coordinate system* to *local displacement* referred at each rolling element location in *local coordinates*.

The inner ring displacement referred to each rolling element is easily defined reminding that those values are defined w.r.t. the inner raceway groove center O_i in Figure 7.2. Since the difference between the inner groove radius of curvature and the rolling

element radius is various orders of magnitude smaller than r_p, for our current purpose we can consider $O_i \equiv O_b$ without introducing significant errors.

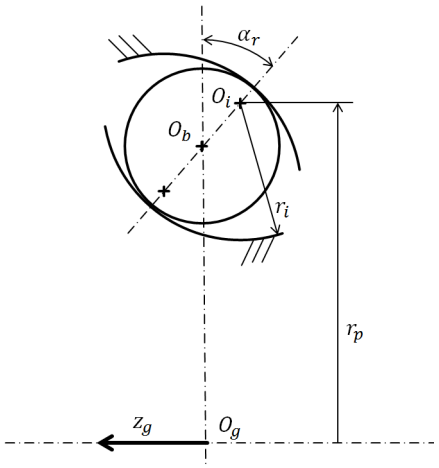

Figure 7.2: The inner ring reference point O_i

Introducing ψ, which is the angle between the ball position on the global $x-y$ plane and the global x-axis, the vector $\overrightarrow{O_gO_i}$ can be written, w.r.t. the global coordinate system, in the following form:

$$\overrightarrow{O_gO_i} = r_p \cdot \begin{bmatrix} \cos\psi & \sin\psi & 0 \end{bmatrix}^T \tag{7.1}$$

Now the local inner ring displacement associated to the global displacement can be written as:

$$\delta_a = -\delta_z - \begin{bmatrix} \gamma_x & \gamma_y & 0 \end{bmatrix}^T \times \begin{bmatrix} r_p\cos\psi & r_p\sin\psi & 0 \end{bmatrix}^T \tag{7.2}$$

$$\delta_r = \begin{bmatrix} \delta_x & \delta_y & 0 \end{bmatrix} \cdot \begin{bmatrix} \cos\psi & \sin\psi & 0 \end{bmatrix}^T \tag{7.3}$$

Where the minus sign in (7.2) is due to the opposite direction between z_g and δ_a.

7.1.2 Methodology to Describe and Sum the Contact Loads in Global Coordinates

The aim of this methodology is to create a standard procedure which allows to sum all the rolling element local forces in global coordinate in order to calculate the reaction forces and moments w.r.t. the origin of the global axis.

In order to align the *global* coordinate system to the *local* system two different rotations have to be composed. Naming $\{S_g\}$, $\{S_1\}$ and $\{S_l\}$ the three coordinate system as shown in figure 7.3, the transformation's steps are:

- $\{S_g\} \rightarrow \{S_1\}$ The purpose of the first rotation is to to align the global x-axis with the ball center as shown in Figure 7.3, it can be done rotating to an angle ψ around the z_g axis;

- $\{S_1\} \rightarrow \{S_l\}$ This transformation aligns the x_l axis with the contact line as shown in Figure 7.3. This rotation is done rotating by an angle α around the y_1 axis.

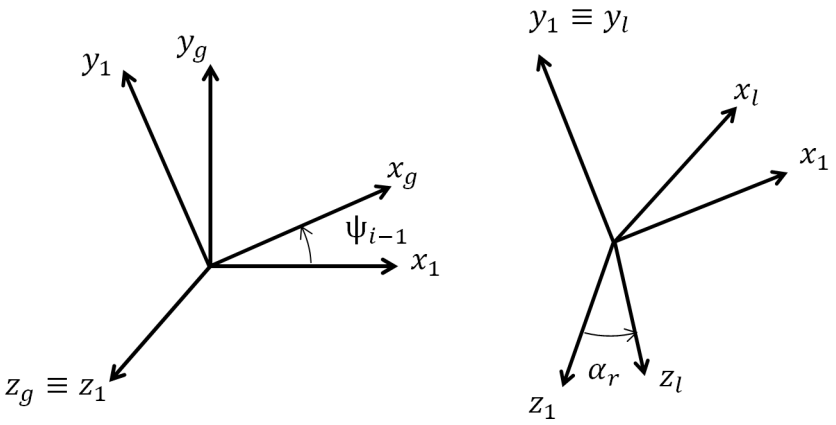

Figure 7.3: Transformation to align the *global* coordinate system to the *local* one

The first rotation defines the system $\{S_1\}$ by the rotation matrix (7.4).

$$\mathbf{R}_{g1} = \begin{bmatrix} \cos\psi & -\sin\psi & 0 \\ \sin\psi & \cos\psi & 0 \\ 0 & 0 & 1 \end{bmatrix} \tag{7.4}$$

Thereafter the second one rotates $\{S_1\}$ aligning it to $\{S_l\}$ by the rotation matrix (7.5).

$$\mathbf{R}_{1l} = \begin{bmatrix} \cos\alpha_r & 0 & \sin\alpha_r \\ 0 & 1 & 0 \\ -\sin\alpha_r & 0 & \cos\alpha_r \end{bmatrix} \tag{7.5}$$

Since the rotations are given in local axes, the transformation $\{S_g\} \rightarrow \{S_l\}$ has to be composed from left hand side to right as follows:

$$\mathbf{R}_{gl} = \mathbf{R}_{g1} \cdot \mathbf{R}_{1l} = \begin{bmatrix} \mathrm{c}\psi\ \mathrm{c}\alpha_r & -\mathrm{s}\psi & \mathrm{c}\psi\ \mathrm{s}\alpha_r \\ \mathrm{s}\psi\ \mathrm{c}\alpha_r & \mathrm{c}\psi & \mathrm{s}\psi\ \mathrm{s}\alpha_r \\ -\mathrm{s}\alpha_r & 0 & \mathrm{c}\alpha_r \end{bmatrix} \tag{7.6}$$

The contact force between the rolling element and the inner ring raceway is in x-direction, Figure 7.4 shows a negative force, in the adopted convention. Since friction is neglected, no forces are introduced along the others directions.

Now a transformation matrix has to be build in order to transform this force in a statically-equivalent combination of forces and moments referred to the *global axes*. All the actions can be combined in a vector, called *wrench*, as follows:

$${}^j w = \left[\begin{array}{ccc|ccc} {}^jF_x & {}^jF_y & {}^jF_z & {}^jM_x & {}^jM_y & {}^jM_z \end{array} \right]^T \tag{7.7}$$

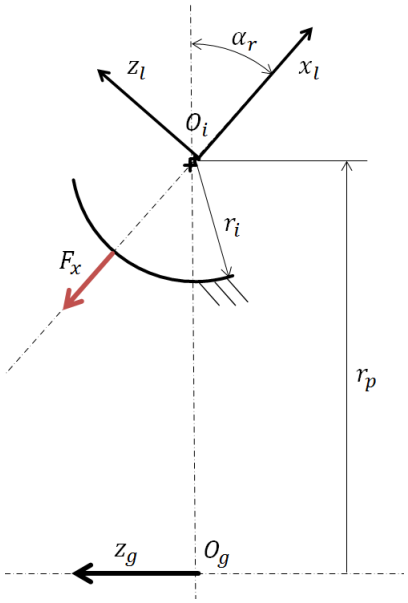

Figure 7.4: Contact load

It is possible to change the application point and coordinate system by a wrench transformation matrix:

$$\mathbf{W}_{gl} = \begin{bmatrix} \mathbf{I}_{3\times3} & \mathbf{0}_{3\times3} \\ \widehat{\mathbf{O}_{gl}} & \mathbf{I}_{3\times3} \end{bmatrix} \begin{bmatrix} \mathbf{R}_{gl} & \mathbf{0}_{3\times3} \\ \mathbf{0}_{3\times3} & \mathbf{R}_{gl} \end{bmatrix} \tag{7.8}$$

Writing the vector $\overrightarrow{O_gO_l} = \overrightarrow{O_{gl}}$ in global coordinates:

$$\overrightarrow{O_{gl}} = \begin{bmatrix} O_{gl_x} \\ O_{gl_y} \\ O_{gl_z} \end{bmatrix} \tag{7.9}$$

$\widehat{O_{gl}}$ is then the cross product matrix defined as follows:

$$\widehat{\mathbf{O}_{gl}} = \begin{bmatrix} 0 & -O_{gl_z} & O_{gl_y} \\ O_{gl_z} & 0 & -O_{gl_x} \\ -O_{gl_y} & O_{gl_x} & 0 \end{bmatrix} \tag{7.10}$$

Now the contribution of the $j-th$ rolling element w.r.t. the global coordinate system centered in O_g can be written as follows:

$${}^{g}w_j = \mathbf{W}_{gl} \cdot {}^{l}w_j \tag{7.11}$$

Since contact load is in $x-direction$, the expressions will be considerably simplified in order to make the code faster. Now it becomes easy to sum all the forces into a single, so called *total*, wrench vector:

$$ {}^{g}w_{tot} = \sum_{j} {}^{g}w_{j} = \left[\begin{array}{ccc|ccc} F_x & F_y & F_z & M_x & M_y & M_z \end{array} \right]^T \tag{7.12} $$

This method will be used to combine the effects of the rolling elements in all developed models, both for ball as well as roller bearings. Concerning roller bearings, minor corrections are needed due to their geometry.

The implementation of this methodology results in a simple, fast and efficient algorithm.

7.2 Angular-Contact Ball Bearing Behavior

This section analyzes the bearing behavior, using the above-mentioned procedure. The behavior is illustrated for a certain displacement of the inner ring w.r.t. the outer ring. Furthermore the inner ring is rotated along the bearing axis (i.g. global z-axis), i.e. the shaft rotation.

To be more precise, the inner ring rotates around the virtual axis defined by the displaced inner ring. The shaft rotation induces a cage rotation, so the position of the balls changes during the simulation. This causes the overall bearing stiffness to vary in time, or as a function of the shaft rotation angle as will be shown.

The behavior is computed for each developed model in order to clarify the difference between them and in order to illustrate the advantages and disadvantages of each contact model. Particular attention will be payed to comparing the model which takes the centrifugal loads into account in dry contact with the one which includes EHL.

In order to be consistent with the comparisons, it is mandatory to select a model of angular-contact ball bearing. For this from the SKF catalog, the bearing *7202 BE-2RZP* is chosen. Since no information is available about dimensions as ball diameter, inner and outer ring raceway curvature radius, pitch radius etc., they are estimated according to the ISO norms [35] and [36] using the static and dynamic load ratings reported by the *SKF* catalogue. As material proprieties the typical values of Young modules and Poisson ratio are choosen since they do not vary too much between different steels. Concerning the lubricant characteristics, the same lubricant used in the *SKF* bearing *DGBB 6202* analyzed by Wensing [37] is considered, since the dimensions are similar to the ones of *7202 BE-2RZP*. The estimated dimensions and the parameters retrieved together known parameters are listed in Table 7.1.

We should remark that the developed codes do not have any sort of restrictions in terms of geometry or material proprieties, in fact their architecture is made to work for small bearings as well as big bearings.

Concerning the displacement, the outer ring will be fixed while the inner one will be displaced in *5-dofs* (in *global coordinate-system*). The rotation around the *global z-axis* will be accounted for as well, but since friction is neglected it is not considered as a *dof.* Therefore the model accounts for two tilting directions x and y and three displacement

B	11 mm	Outer ring width
D_{ob}	35 mm	Outer bore diameter
D_{ib}	15 mm	Inner bore diameter
r_i	3.07 mm	Inner-ring curvature radius
r_o	3.24 mm	Outer-ring curvature radius
D	6 mm	Ball diameter
r_p	15.7 mm	Radius of the inner raceway groove center
r_q	15.56 mm	Radius of the outer raceway groove center
$clnc$	0.0335 mm	Axial clearance
α	40°	Nominal contact angle
α_{max}	70°	Maximum contact angle allowed
r_{pw}	15.63 mm	Pitch radius
Z	8	Number of rolling elements
E	206 GPa	Young modulus
ν	0.3	Poisson ratio
ρ	7.8 kg/dm^3	Material density
α_{barus}	$1 \cdot 10^{-8}$ Pa^{-1}	Lubricant pressure-viscosity coefficient
η_0	0.1 Pas	Lubricant viscosity at ambient pressure

Table 7.1: Geometrical and material proprieties

directions x, y and z.
The linear displacement along the i-direction is then named δ_i whereas the j-direction tilting γ_j.

7.2.1 Idealized Bearing Behavior

This subsection shows the achievements obtained by the *ideal model* introduced in Chapter 4. Reminding that this model takes into account the clearance while it neglects the centrifugal loads, the behavior will be influenced only by geometrical bearing proprieties.

To compute the solution, the translations of the inner ring are fixed as well as γ_y. In particular the values shown in Table 7.2 are used.

δ_x	$1.5 \cdot 10^{-2}$ mm
δ_y	0 mm
δ_z	$-2.5 \cdot 10^{-2}$ mm
γ_y	0°

Table 7.2: Displacement applied to the bearing inner ring

The results are plotted as a function of the shaft rotational angle while four different values of γ_x are used.

Figure 7.5 (a-c) shows the bearing behavior, it is clearly visible how the bearing

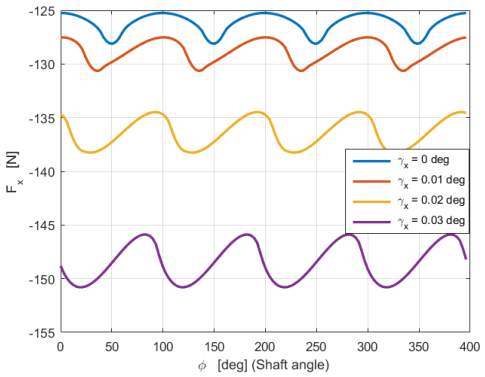

(a) Bearing reaction force along the x-axis

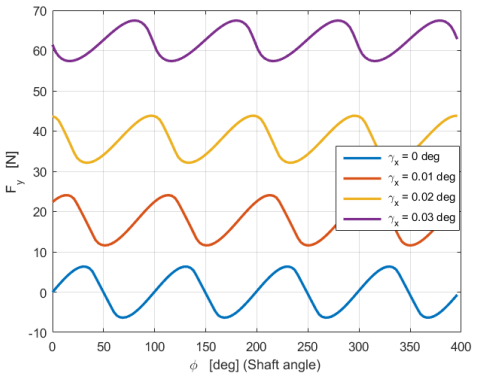

(b) Bearing reaction force along the y-axis

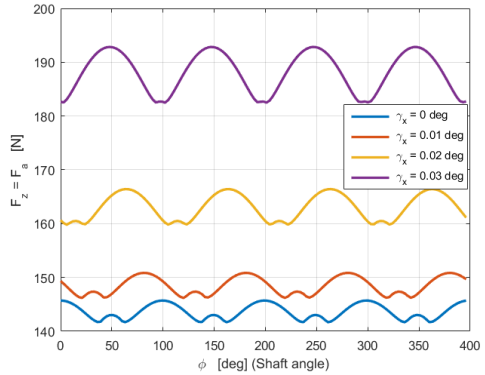

(c) Bearing reaction force along the z-axis

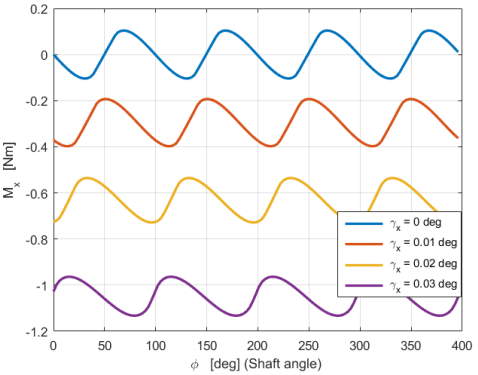

(d) Bearing reaction moment along the x-axis

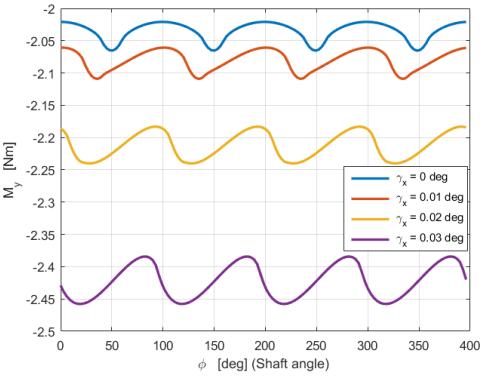

(e) Bearing reaction moment along the y-axis

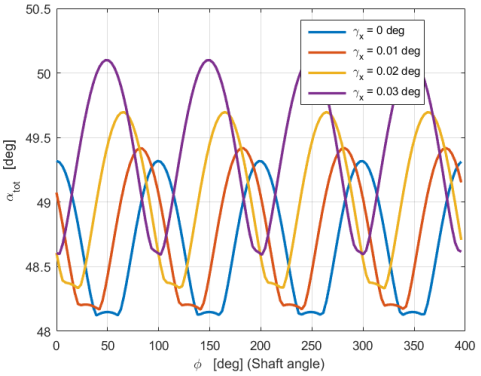

(f) Equivalent bearing angle α_{tot}

Figure 7.5: Bearing reaction forces, moments and equivalent bearing angle

stiffness depends from the internal ball arrangement. In fact rotating the shaft, also the position of the ball changes. This leads to a non-constant reaction for a fixed displacement which means a non-constant stiffness.

Then the moments are computed and shown in Figure 7.5 (d-e).

In all the shown pictures it is clearly visible how the stiffness oscillations have a fixed period which corresponds to the following shaft rotational angle:

$$\psi_T = \frac{2\pi}{Z} \cdot \frac{r_p - D/2 \cos\alpha_r}{2\, r_{pw}} \tag{7.13}$$

Furthermore the equivalent contact angle α_{tot} is computed. With equivalent contact angle is meant the angle between the resultant of the forces and the plane perpendicular to the bearing axis. It can be seen as a weighted mean value of the contact angles of all the rolling elements. The above-mentioned angle is computed and his behavior is shown in Figure 7.5 (f)

7.2.2 Bearing Behavior Accounting for Centrifugal Loads

As seen in Chapter 5, introducing the centrifugal load, the load symmetry of the contact loads is lost due to the contact angles α_i and α_o which are no more coincident. Moreover the discontinuity will play a major role in the bearing behavior since it will deeply influence the stiffness fluctuations.

The load-deflection characteristic of the rolling element will be more similar to the *idealized model* as the penetration increases, since the centrifugal load looses its relevance if compared with the contact loads.

To compute the solution the displacements listed in Table 7.3 are introduced.

δ_x	$-2.5 \cdot 10^{-2}\ mm$
δ_y	$-2.5 \cdot 10^{-2}\ mm$
δ_z	$-2.5 \cdot 10^{-2}\ mm$
γ_y	$0.01°$

Table 7.3: Displacement applied to the bearing inner ring

Two different values are studied for γ_x, respectively 0.01°and 0.02°. The bearing behavior under the mentioned hypotheses is shown in Figure 7.6 and Figure 7.7.

It is clearly visible how the discontinuity affects the behavior.

Moreover in Figure 7.8 the equivalent bearing angle α_{tot} is shown. Also here, the discontinuity and the fluctuating trend are visible.

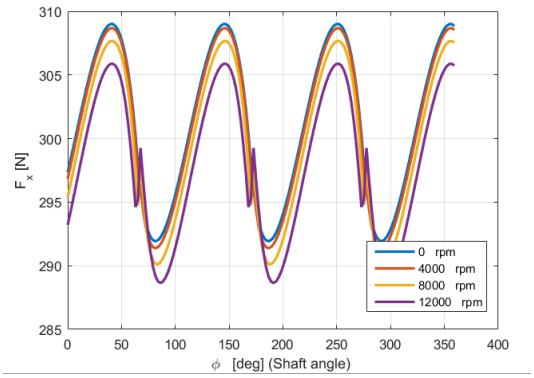

(a) Reaction force along the x-axis with $\gamma_x = 0.01°$

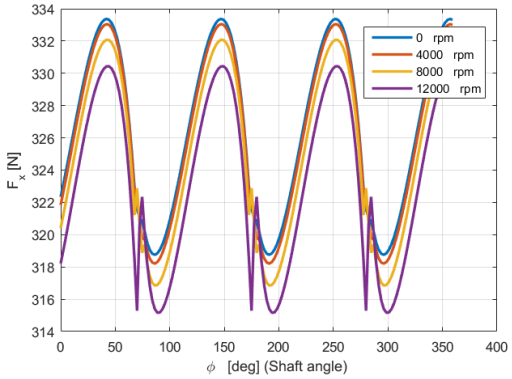

(b) Reaction force along the x-axis with $\gamma_x = 0.02°$

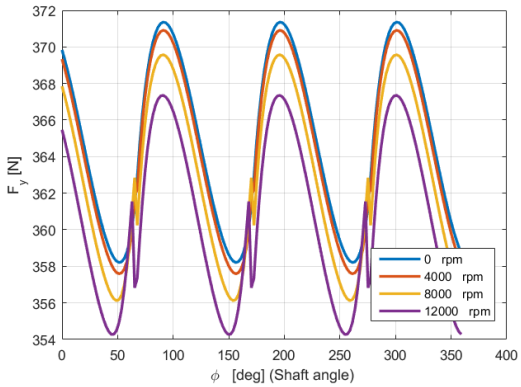

(c) Reaction force along the y-axis with $\gamma_x = 0.01°$

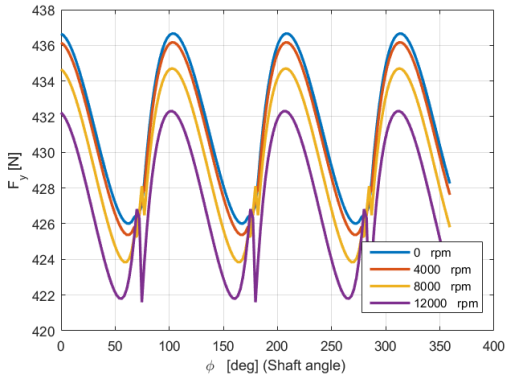

(d) Reaction force along the y-axis with $\gamma_x = 0.02°$

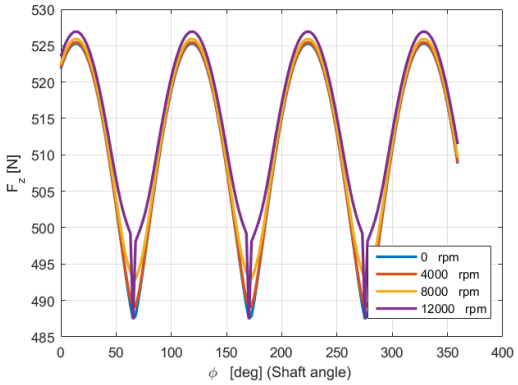

(e) Reaction force along the z-axis with $\gamma_x = 0.01°$

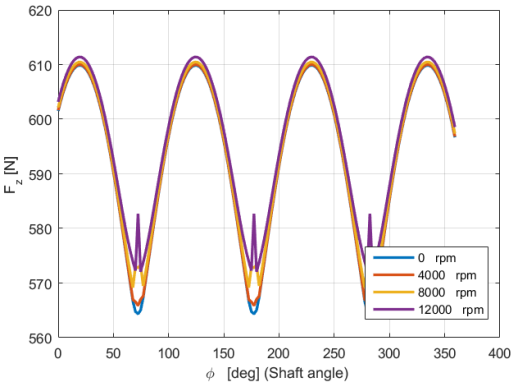

(f) Reaction force along the z-axis with $\gamma_x = 0.02°$

Figure 7.6: Bearing reaction forces

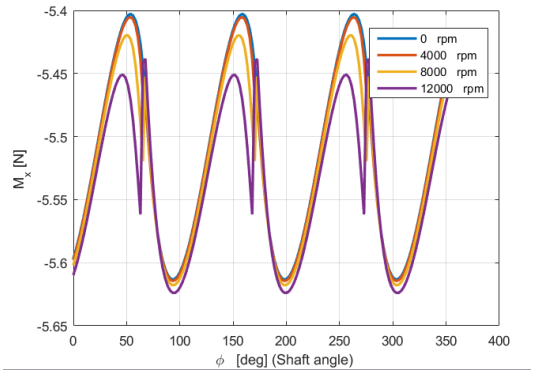

(a) Reaction moments along the x-axis with $\gamma_x = 0.01°$

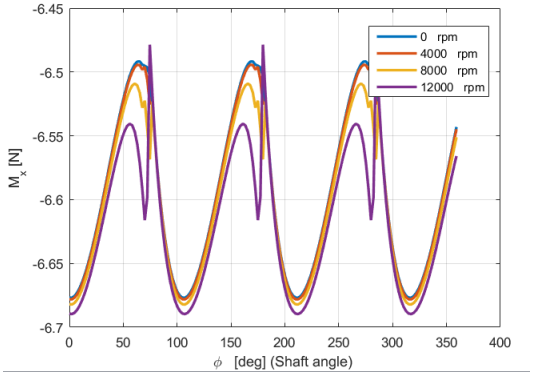

(b) Reaction moments along the x-axis with $\gamma_x = 0.02°$

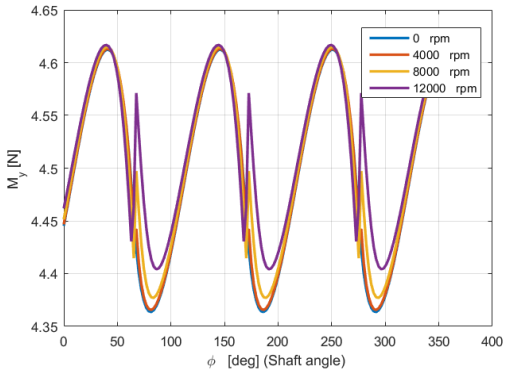

(c) Reaction moments along the y-axis with $\gamma_x = 0.01°$

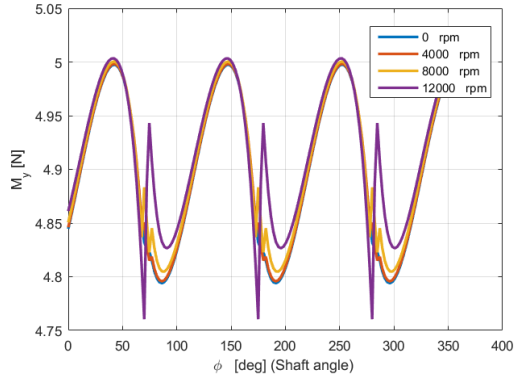

(d) Reaction moments along the y-axis with $\gamma_x = 0.02°$

Figure 7.7: Bearing reaction moments

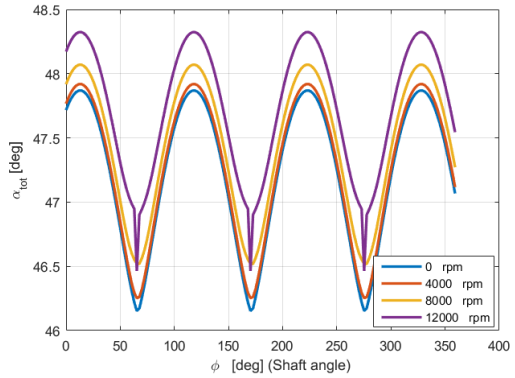

(a) Equivalent bearing angle with $\gamma_x = 0.01°$

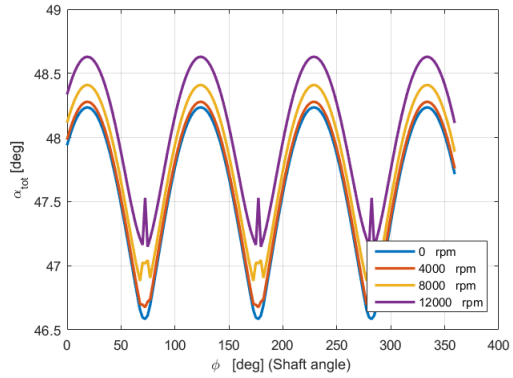

(b) Equivalent bearing angle with $\gamma_x = 0.02°$

Figure 7.8: Equivalent bearing angle

7.2.3 Bearing Behavior Accounting for EHL

This subsection shows the bearing behavior accounting for *elastohydrodynamic lubrication* as fully explained in Chapter 6. The solution is computed exactly as done for the previous models but, as already mentioned, this model requires more computational effort due to all the involved iterative processes.

In this model, the shaft speed plays a major role, since the contact load is highly influenced by it. As done before, three translations of the inner ring and the tilting around y-axis are fixed. The imposed displacements are summarized in the Table 7.4.

δ_x	$-2.5 \cdot 10^{-2}\ mm$
δ_y	$-2.5 \cdot 10^{-2}\ mm$
δ_z	$-2.5 \cdot 10^{-2}\ mm$
γ_y	$0.01°$

Table 7.4: Displacement applied to the bearing inner ring

Two different values of γ_x are studied, respectively 0.01°and 0.02°, and four different rotation speeds, respectively 0 rpm 4000 rpm 8000 rpm and 12000 rpm. The results are shown in Figure 7.9 and Figure 7.10 where also the equivalent bearing angle is computed and shown.

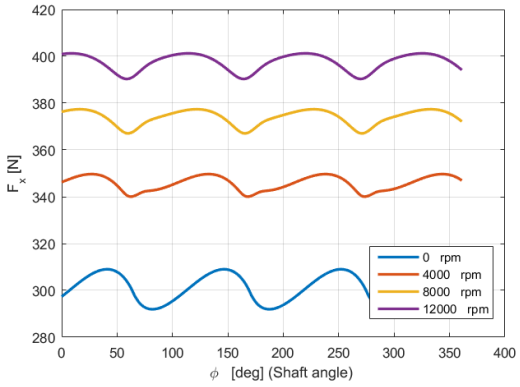

(a) Reaction force along the x-axis with $\gamma_x = 0.01°$

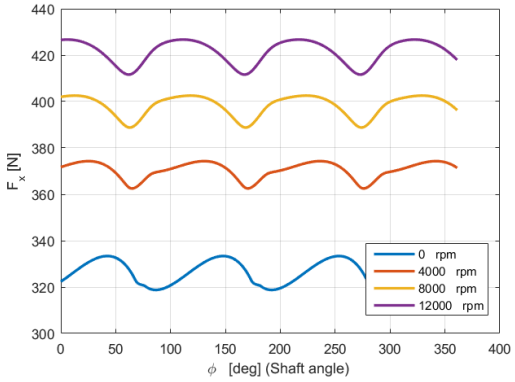

(b) Reaction force along the x-axis with $\gamma_x = 0.02°$

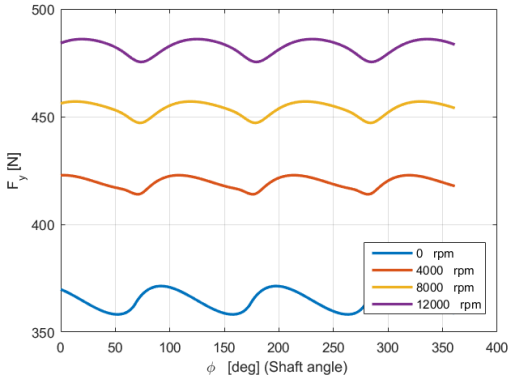

(c) Reaction force along the y-axis with $\gamma_x = 0.01°$

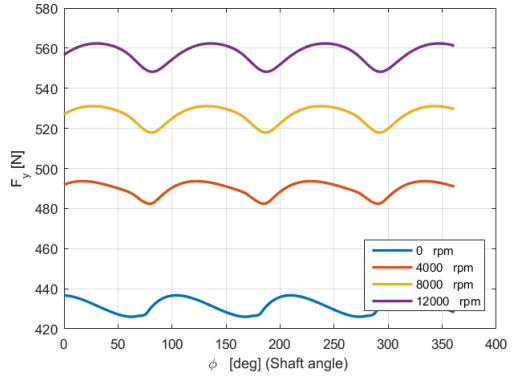

(d) Reaction force along the y-axis with $\gamma_x = 0.02°$

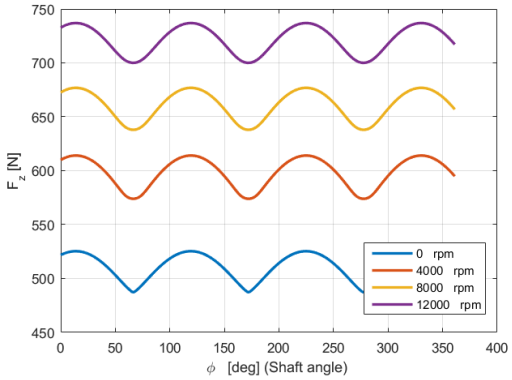

(e) Reaction force along the z-axis with $\gamma_x = 0.01°$

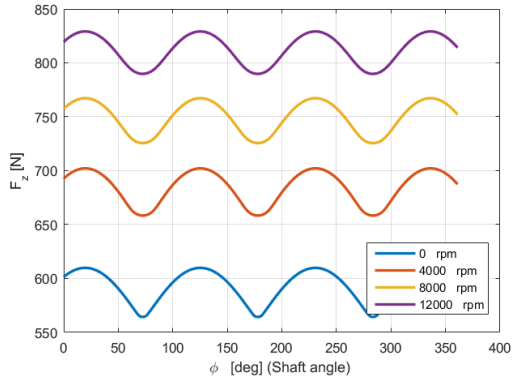

(f) Reaction force along the z-axis with $\gamma_x = 0.02°$

Figure 7.9: Bearing reaction forces

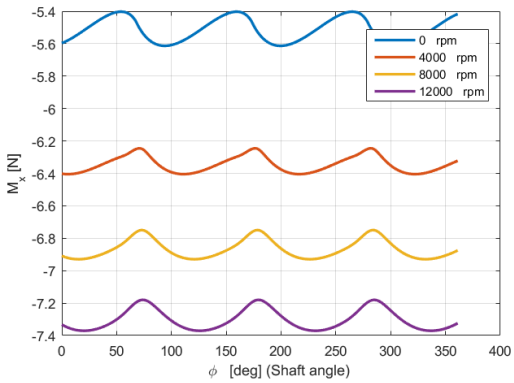

(a) Reaction moments along the x-axis with $\gamma_x = 0.01°$

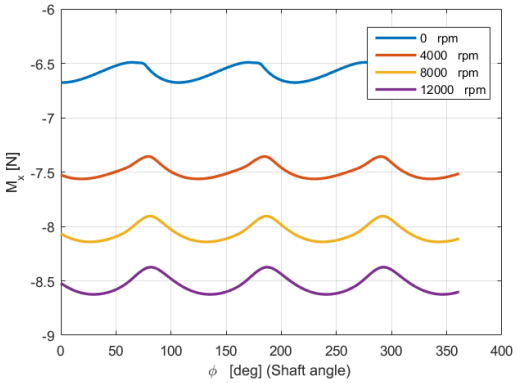

(b) Reaction moments along the x-axis with $\gamma_x = 0.02°$

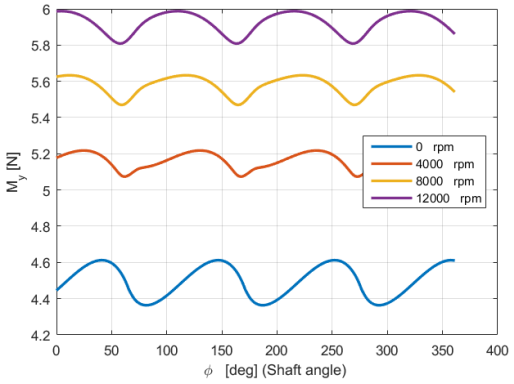

(c) Reaction moments along the y-axis with $\gamma_x = 0.01°$

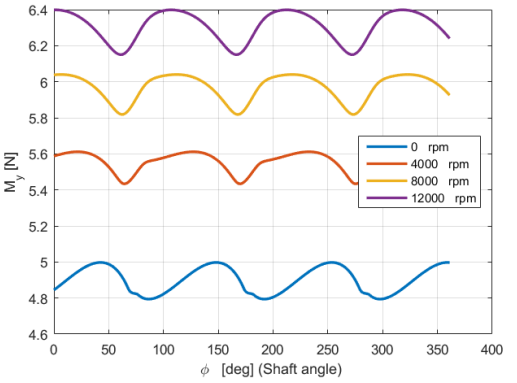

(d) Reaction moments along the y-axis with $\gamma_x = 0.02°$

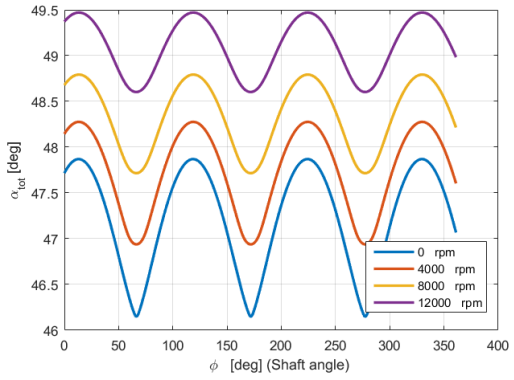

(e) Equivalent bearing angle with $\gamma_x = 0.01°$

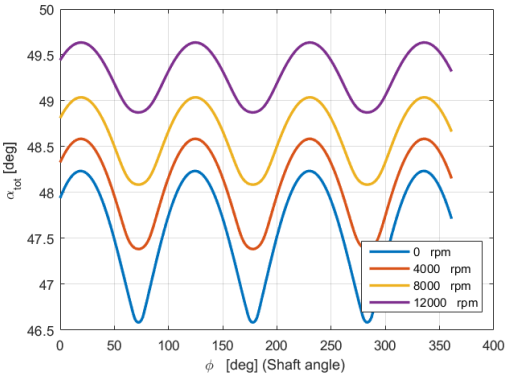

(f) Equivalent bearing angle with $\gamma_x = 0.02°$

Figure 7.10: Bearing reaction moments and equivalent bearing angle

7.2.4 Dry-Centrifugal vs. EHL-Centrifugal

In this section a comparison between the developed model is shown. In particular the dry contact model and the EHL model are compared, both accounting for centrifugal

load. As already seen in Chapter 5, the shaft speed has only limited influence on the bearing behavior in case of dry contact, since increasing the load on the rolling element, the behavior converges to the one without centrifugal load. While in case of EHL contact, the influence of the shaft speed plays a key role since it increases the lubricant effect, deeply changing the bearing response.

Introducing the displacements in Table 7.5 the model solution is then computed.

δ_x	$-2.5 \cdot 10^{-2}\ mm$
δ_y	$-2.5 \cdot 10^{-2}\ mm$
δ_z	$-2.5 \cdot 10^{-2}\ mm$
γ_y	$0.01°$
γ_x	$0.03°$

Table 7.5: Displacement applied to the bearing inner ring for the comparison

The comparison between the models is shown in Figure 7.11. It is clearly visible how, when the shaft speed exceeds a certain value, the dry contact model returns underestimated values. Moreover the EHL model returns a smoother behavior, hence more suitable. On the other hand, the process to compute the solution accounting for EHL, is more time consuming than the dry contact model, even if it still allows for a fast solution.

Concerning forces and moments the dry contact returns, varying ω_{shaft}, curves which are almost overlapping, while considering the angle α_{real} a slight difference can be already seen even if lubrication is neglected. Introducing the lubrication the characteristic curves are shifting while the shape and the wave frequency remains the same since it is defined by the number of rolling element within the bearing.

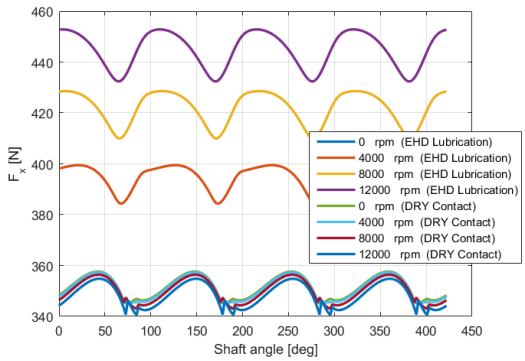

(a) Bearing reaction force along the x-axis

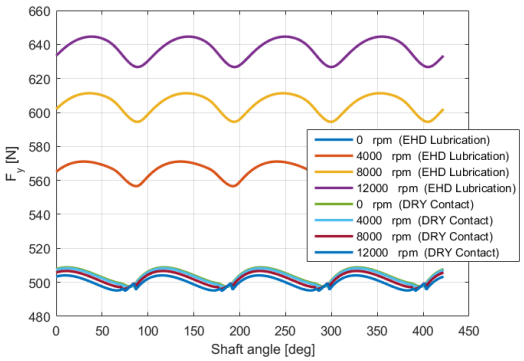

(b) Bearing reaction force along the y-axis

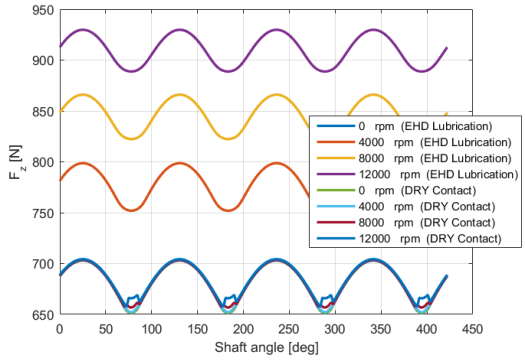

(c) Bearing reaction force along the z-axis

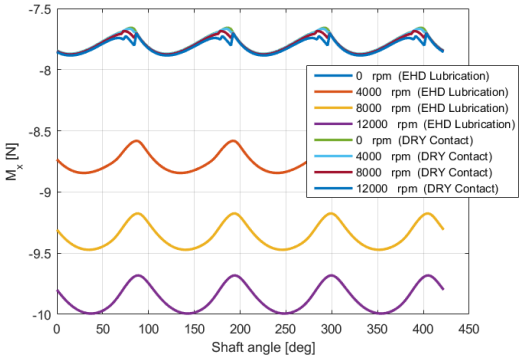

(d) Bearing reaction moment along the x-axis

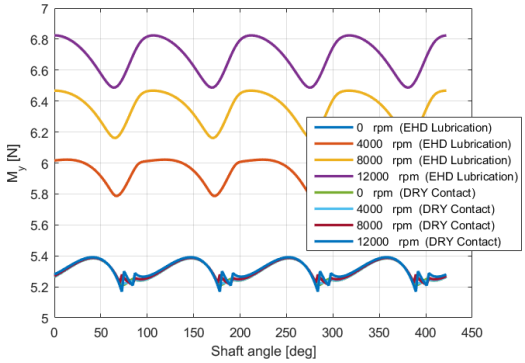

(e) Bearing reaction moment along the y-axis

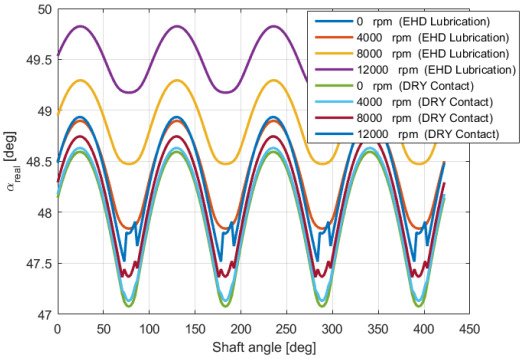

(f) Equivalent bearing angle α_{tot}

Figure 7.11: Comparison between Dry contact model and EHL of bearing reaction forces, moments and equivalent bearing angle

Chapter 8

Angular Contact Ball Bearings Modeling Techniques Conclusions

In this part, the developed modeling techniques for ball bearings have been described. First clearance and preload have been introduced defining the first model. Then, the second model has been defined introducing the centrifugal load which causes loss of symmetry. Finally, the third model has been defined introducing the lubrication in elastohydrodynamic regime.

The models developed through this part, allow the computationally efficient and high-fidelity prediction of angular contact ball bearings. The developed modeling techniques are generic. The same procedure has been applied to thrust ball bearings (Figure 8.1) deep groove ball bearings (Figure 8.2). However the results are not shown since they are alike the ones obtained for angular contact ball bearings.

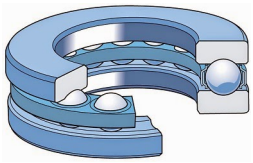

Figure 8.1: Thrust Ball Bearing

Figure 8.2: Deep Groove Ball Bearing

The developed contact models allow to predict the bearing behavior based on models with increasing fidelity. As the fidelity increases, also the computational effort required

to compute the solution increases. Even if the computational cost increases, the process remains affordable, since the computational time remains low if compared with the achieved fidelity level.

Since the developed modeling techniques are modular and based on contact modeling, they can be easily adapted to broaden the covered types. For example, a modeling technique for self aligning ball bearing (Figure 8.3) and all the types based on point contact can be easily created.

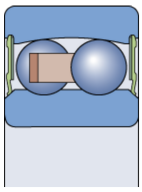

Figure 8.3: Self-Aligning Ball Bearing

Part II

Development of Modeling Techniques for Roller Bearings

Chapter 9

Introduction to Roller Bearings

This part shows how cylindrical and tapered roller bearings are modeled starting from the contact model to describe the bearing behavior.

Figure 9.1 shows a cylindrical roller bearing which is studied as first case since the tapered roller bearing case can be seen as a more complex variation of cylindrical roller bearings.

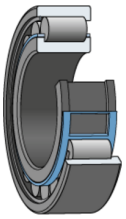

Figure 9.1: Cylindrical Roller Bearing

As first contact model the dry contact accounting for centrifugal load and clearance of a cylindrical roller on a raceway is analyzed. The introduced roller shape, takes into account the roller crowning by means of a logarithmic shape. In order to account for misalignment between the roller and the raceways a slicing technique is introduced. The slicing technique allows to account for variable penetration along the contact line. It consist of a discretization of the roller in slices, the thiner the slices, the more accurate is the solution since the penetration is considered constant in each slice. The coupling between deformation of slices is neglected.

Then once all these techniques are introduced, the equilibrium of a roller squeezed between the raceways is introduced.

The second level of fidelity introduces the lubricant effects. The roller is still discretized in slices and the leakage between slices is neglected. Due to the non-conformal contact, the contact operates in Elastohydrodynamic regime (EHL). The lubrication ensures more fidelity even if it increases the computational effort required to compute the solution.

The second type of roller bearings studied is the tapered roller bearings. An example is shown in Figure 9.2.

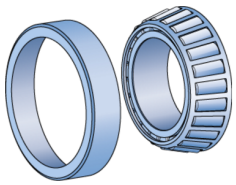

Figure 9.2: Tapered Roller Bearing

In order to model the tapered roller, the same contact models are introduced for the cylindrical roller are used. While the roller equilibrium has to be reformulated due to the flange and the conical shape of the roller which introduces one more direction in which the equilibrium has to computed. The flange is modeled as a constraint, even if a contact model for it can be easily introduced.

Once the solution for the tapered roller squeezed between the raceways is defined, a study case is introduced to show his behavior achieved with the techniques proposed, pointing out the differences between the different models.

Chapter 10

Cylindrical Roller Bearing in Dry Contact

The first model which has to be developed concerns the modeling technique for a roller squeezed between two raceways in *dry contact*. With respect to the ball, this case has an increased complexity since the load-deflection relation is no more 1-D but it has 2 degrees of freedom, since the penetration along the contact line can be both uniform (e.g. pure translation of the raceway, remaining parallel to the roller axis) or a linear function (e.g. pure rotation of the raceway along a direction perpendicular to the cross-section).

Moreover the crowning of the rolling element is taken into account, since any roller is not a perfect cylinder but is shaped in a way which reduces the stress concentration on the roller sides. The roller crowning adds more complexity to the penetration since it can no more be characterized as sum of a linear function and a constant one. The crowning of the roller is defined as *micro-geometry correction* since the amount of material removed is small compared to the roller dimensions and normally it cannot be seen by the unaided eye.

As done for angular contact ball bearings, the outer raceway is considered fixed in space while the inner one is displaced. The inner raceway movement can be defined by two parameters, s_i and θ_i, where the first one is the translation approach perpendicular to the roller axis and the second one is the inner raceway rotation on the cross section plane as shown in Figure 10.1.

The following assumptions are made:

- Roller skewing is neglected, since the focus in this work is to obtain accurate load-displacement predictions for the overall bearing, whereas roller skewing predominantly affect bearing durability;
- Raceway shoulder and flange effects are negligible;
- The dynamic loads as impacts or roller inertia forces are not taken in account (except centrifugal loads);
- Stress concentrations at roller sides due to line contact do not influence the solution;

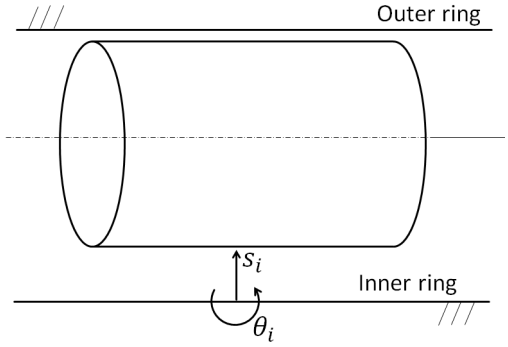

Figure 10.1: Roller between two raceways

- The proportional limit of the material is not exceeded, that is, all the deformation occurs in the elastic range;
- Shear stress on the contact surface is neglected, which means friction is neglected;
- The radii of curvature at the contact areas are very large compared with the dimensions on these areas;
- Lubricant effects are neglected, hence dry contact.

Since the penetration along the contact line is no more constant, the *Hertz formulation* for line contacts which predicts the contact load-deflection behavior is not further applicable. The technique which allows us to take into account this non uniform penetration is the *Slicing Technique*.

10.1 Slicing Technique

The slicing technique here described allows to consider variable penetration along the contact line, coming from raceway rotation and roller crowning. The slicing technique in line contact has been used in several cases (e.g. roller bearing, bevel gears etc.) because of its simplicity and its capability to account for many effects such as line contact along a curved line (e.g. bevel gears), non-uniform penetration and, moreover, the fidelity of the slicing technique can be tuned case by case.

The developed slicing technique is basically based on the work of Teutsch [25] which proposed first the classic slicing technique including some formulations to model the contact slice-raceway and then a method to take into account the coupling between slices. The coupling method presented in that work [25] is not suitable in our modeling technique since is not reliable for all cases. In fact the solution achieved with the method described in [25], fits the real solution only in some cases and it does not converge as the number of slices increases, making it somewhat questionable.

Many formulations to characterize the contact are listed in [25]; one of the most accurate predictions is done by Dinnik [20] which considered a parabolic distribution of pressure along the width of contact.

In the developed work, the Dinnik's formulations (10.1) and (10.2) are used. However, the developed modeling technique is modular and any other formulation could be used instead. This formulation is used since it takes into account the surfaces curvature and raceway thickness.

$$\delta_i = \left(\frac{2Q}{\pi L}\right) \cdot \left[\frac{1-\nu^2}{E}\left(\ln\frac{D}{b}+\frac{1}{3}\right)+\frac{1-\nu^2}{E}\left(\ln\frac{2R_i}{b}+\frac{1}{3}\right)\right] \tag{10.1}$$

$$\delta_o = \left(\frac{2Q}{\pi L}\right) \cdot \left[\frac{1-\nu^2}{E}\left(\ln\frac{D}{b}+\frac{1}{3}\right)+\frac{1-\nu^2}{E}\left(\ln\frac{t}{b}+\frac{1}{3}\right)\right] \tag{10.2}$$

Where R_i is the inner raceway radius of curvature.

Many different formulations have been proposed in the past. Many authors noticed that in line contacts the surfaces curvature has a minor influence on the solution, while many others developed formulas which account for more geometrical parameters, therefore offering a better contact prediction. The more accurate were developed by Kowalsky [20] in 1940 and by Tripp [23] in 1985. The last two cited authors' formulas are very close to the Dinnik's formulation. Since this, in order to be aligned with [25] the Dinnik's formulation is used.

Figure 10.2 shows a roller contacting with a flat raceway, where the contact semi-length b is shown.

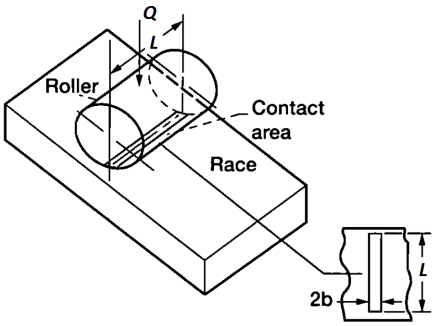

Figure 10.2: Schematic of flat roller profile on a flat race [38]

In order to implement a procedure as simple as possible, the equations (10.1)(10.2) have to be expressed as $\delta = C\,Q^n$ where C is a constant variable and $n \in \mathbb{R}$, in order to inverse and derive them easily. As reported in [25], Dinnik's formulas can be written in the following equivalent form:

$$\delta_i = 3.17\left(\frac{d_{pw}}{2}\right)^{0.08} \cdot \left(\frac{Q\left(1-\nu^2\right)}{EL}\right)^{0.92} \tag{10.3}$$

$$\delta_o = 2.66\left(\frac{t}{1+D/d_{pw}}\right)^{0.09} \cdot \left(\frac{Q\left(1-\nu^2\right)}{EL}\right)^{0.91} \tag{10.4}$$

By the latter equations the load Q can be isolated achieving the targeted expression.

The slicing technique principle is based on an approximation of the problem, by dividing the roller along its axis in a certain amount of slices which are analyzed separately assuming that the penetration remains constant along each slice. Thus at each slice the used value for penetration is calculated in correspondence of his mean plane.

The position of each slice along the roller axis, is defined by the parameter z_j which represent the distance between the *roller mean plane* and the *j-th slice mean plane*. Then, since the outer raceway is considered fixed in space, the inner raceway displacement w.r.t. the outer one has to be defined. This can be done introducing two motion parameters, s_i and θ_i which represent respectively the radial translation and the rotation in the cross-section plane of the inner raceway w.r.t. tho outer raceway. The same is done to describe the roller position w.r.t. an initial position, in the roller case they are called s_x and θ_y where the subscripts are referred to the local coordinate system. The above-mentioned is shown in Figure 10.3 where the following convention is adopted for the zero-position of the roller: the mean position between the undisplaced raceways considering also the *radial clearance* referred to as cl.

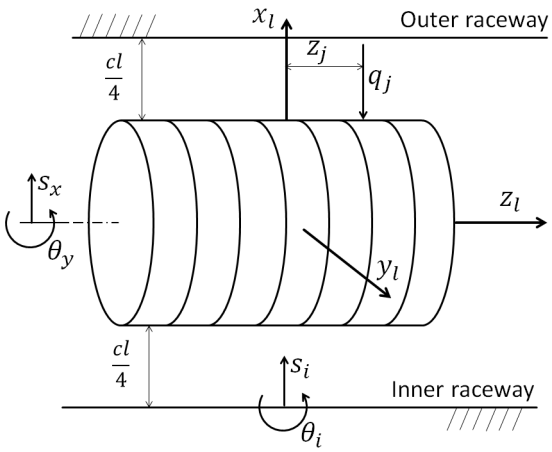

Figure 10.3: Sliced roller with reference parameters and local coordinate system

Figure 10.3 also shows the contact force acting between the raceway and the j-th slice, which is called $q_{i,j}$ or $q_{o,j}$ depending from which contact is referred to.

The slices are supposed to be short, the length of each slice will be called l while the amount of slices will be called as m.

Since the inner raceway displacement is the model input, the first step is to define an algorithm to calculate the penetration of the contact of each rolling element. First the penetration between the roller and the outer raceway is formulated, which is easier since it is function only of the roller position. Then the roller-inner raceway penetration is defined.

Roller-Outer Raceway Penetration Introducing the vector $\mathbf{z} \in \mathbb{R}^m$ which collects the z-coordinates of the slices' mean planes, the penetration can be divided in two contributions: a constant one which considers the translation of the rolling element and a linear function which describes the rotation effect. Therefore, adding the clearance

contributions, the penetration can be written as follows:

$$\mathbf{pen}_o = \begin{bmatrix}\delta_{o,1} & \dots & \delta_{o,m}\end{bmatrix}^T = s_x + \theta_y \mathbf{z} - cl/4 \tag{10.5}$$

Roller-Inner Raceway Penetration This penetration can be defined considering $\mathbf{pen}_o$ with the opposite sing, since if one slice approaches to the outer raceway it moves further away from the inner raceway of the same quantity. Then the contribute of the inner raceway movement is summed, which can be modeled as done before for the roller-outer raceway penetration. Thus the formulation reads:

$$\mathbf{pen}_i = \begin{bmatrix}\delta_{i,1} & \dots & \delta_{i,m}\end{bmatrix}^T = s_i + \theta_i \mathbf{z} - (s_x + \theta_y \mathbf{z}) - cl/4 \tag{10.6}$$

During the penetration calculation also the real shape of the roller has to be taken into account, since till now only a cylindrical shape has been considered. To do so, a crowning formulation has to be introduced, then both formulation will be merged in order to formulate the complete problem.

10.2 Optimized Logarithmic Roller Crowning

During the bearing design process, roller crowning is introduced in order to better distribute the contact stresses along the rolling element length, since without crowning the roller edges would be highly loaded because of stress concentrations. Moreover, in case of pure tilting, with a straight profile the line contact can degenerate in a point contact in the edge location which provokes a high stress gradient, which could compromise the durability of the component.

Currently there is not a standard shape, each supplier tunes it case by case. Many formulations have been proposed over the years and many different profiles have been studied. In the work of Fujiwara [39] the crowning issue is fully discussed in terms of durability and stress concentrations. This work refers to the formulation proposed in his work [40], which fits with many of the most used profiles.

Such a type of crowning can prevent the edge loading even in case the roller is tilted. It takes into account the fact that bearing rollers typically have a central land without any crowning. Then the crowning profile slightly tapers off the roller radius toward the roller ends, therefore the radius reduction is referred to as *crown drop*. The straight part of the profile together with the crowned one cover the whole roller length. In this formulation three parameters, shown in Table 10.1, are introduced to describe the roller shape.

A	Degree of the curvature of the crowning curve
l_s	Length of the central straight zone
z_m	Crown drop at the end of the ends of the effective contact

Table 10.1: Crowned profile parameters used in the showcase

According with Fujiwara [40], the crown drop of the j-th slice is defined as:

$$CrownDrop_j = -A \ln\left(1 - \left[1 - \exp\left(-\frac{z_m}{A}\right)\right]\left(\frac{2\,\mathbf{z}\,(j) - l_s}{l - l_s}\right)^2\right) \tag{10.7}$$

Which brings the shape shown in Figure 10.4, where only a quarter of the roller is shown, as the roller is symmetric.

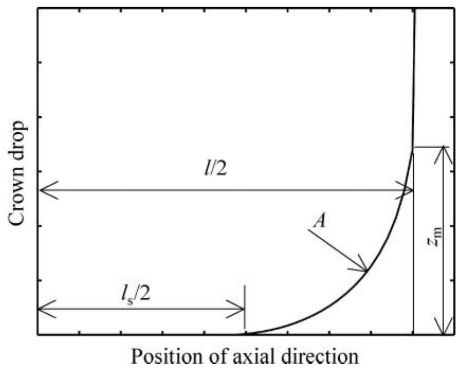

Figure 10.4: Logarithmic profile with the parameters A, l_s and z_m [39]

This method is illustrated in the following case study. For this purpose the parameters in Table 10.2 are introduced. The studied roller corresponds to the bearing which will be used to study the whole bearing behavior.

L	Roller length	10 mm
D	Roller diameter	5.69 mm
A	Degree of the curvature of the crowning curve	$3.46 \cdot 10^{-3}$ mm
l_s	Length of the central straight zone	5 mm
z_m	Crown drop at the end of the ends of the effective contact	$6.49 \cdot 10^{-3}$ mm

Table 10.2: Roller and crowning parameters

The parameters in Table 10.2 with the Eq. (10.7) return the shape shown in Figure 10.5 where the shape is magnified due to the different axes scale.

It is clear that as the inner raceway approaches, the contact line length increases, which influences the contact stiffness. On the other hand, it requires finer roller slices as well. In fact the stiffness variation is the only effect which matters for this work's purpose, since the goal is not a durability study but the overall bearing behavior.

10.3 Roller Equilibrium Accounting for Centrifugal Loads

This section describes the method to compute the rolling element equilibrium. As already mentioned, the axial displacement of the inner ring is not taken into account for two reasons. First, this type of bearings are not meant to bear axial loads, therefore

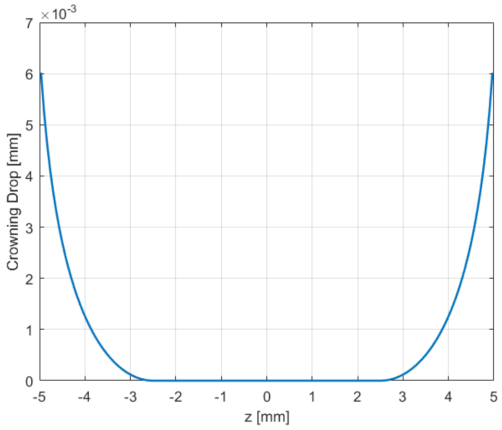

Figure 10.5: Logarithmic profile applied to a roller

they are usually combined with a tapered, angular contact or thrust bearing which carries the axial load. The second reason is based on the fact that most part of the radial roller bearing have flanges only on the outer ring while the inner one do not have them in order to avoid accidental axial loads. Because of this the roller has *2 dofs*, one translation and one tilting.

Section 10.1 explained how the roller and the inner ring displacement provoke penetration between the surfaces and by Eq. (10.6)and Eq. (10.5) the penetration vectors are calculated. However they do not account for the real profile shape. This can be done by subtracting the vector **CrownDrop** to the penetration, which brings to the following formulas:

$$\mathbf{pen}_o = s_x + \theta_y \mathbf{z} - cl/4 - \mathbf{CrownDrop} \tag{10.8}$$

$$\mathbf{pen}_i = s_i + \theta_i \mathbf{z} - (s_x + \theta_y \mathbf{z}) - cl/4 - \mathbf{CrownDrop} \tag{10.9}$$

The load-deflection relation for each contact of each slice can be formalized from Eq. (10.3) and Eq. (10.4) as follows:

$$q_{i,j} = C_i \, \mathbf{pen}_i \, (j)^{1/0.92} \tag{10.10}$$

$$q_{o,j} = C_o \, \mathbf{pen}_o \, (j)^{1/0.91} \tag{10.11}$$

Where:

$$C_i = \left[3.17 \left(\frac{d_{pw}}{2} \right)^{0.08} \cdot \left(\frac{Q \left(1 - \nu^2 \right)}{EL} \right)^{0.92} \right]^{-1/0.92} \tag{10.12}$$

$$C_o = \left[2.66 \left(\frac{t}{1 + D/d_{pw}} \right)^{0.09} \cdot \left(\frac{Q \left(1 - \nu^2 \right)}{EL} \right)^{0.91} \right]^{-1/0.91} \tag{10.13}$$

Finally the roller equilibrium can be written as:

$$\begin{cases} F_x &= \sum_{j=1}^{m} \left(q_{i,j} - q_{o,j}\right) + F_c &= 0 \\ M_y &= \sum_{j=1}^{m} \left[\left(q_{i,j} - q_{o,j}\right) \mathbf{z}\left(j\right)\right] &= 0 \end{cases} \tag{10.14}$$

Where F_c represent the centrifugal load acting on the roller.

In order to solve Eq. (10.14) an iterative process has to be used, since a closed-form solution would be difficult or even impossible to formulate. As usual, the iterative process is based on the *Newton-Raphson method*, which requires the evaluation of the Jacobian consisting of the partial derivative of the Eq. (10.14) w.r.t. the roller position parameters s_x and θ_y, as shown in Eq. (10.15).

$$\mathbf{J} = \begin{bmatrix} \dfrac{\partial F_x}{\partial s_x} & \dfrac{\partial F_x}{\partial \theta_y} \\ \dfrac{\partial M_y}{\partial s_x} & \dfrac{\partial M_y}{\partial \theta_y} \end{bmatrix} \tag{10.15}$$

Deriving Eq. (10.14) w.r.t. s_x and θ_y, it becomes:

$$\frac{\partial F_x}{\partial s_x} = \sum_{j=1}^{m} \left(\frac{\partial q_{i,j}}{\partial s_x} - \frac{\partial q_{o,j}}{\partial s_x} \right) \tag{10.16}$$

$$\frac{\partial F_x}{\partial \theta_y} = \sum_{j=1}^{m} \left(\frac{\partial q_{i,j}}{\partial \theta_y} - \frac{\partial q_{o,j}}{\partial \theta_y} \right) \tag{10.17}$$

$$\frac{\partial M_y}{\partial s_x} = \sum_{j=1}^{m} \left[\left(\frac{\partial q_{i,j}}{\partial s_x} - \frac{\partial q_{o,j}}{\partial s_x} \right) \mathbf{z}\left(j\right) \right] \tag{10.18}$$

$$\frac{\partial M_y}{\partial \theta_y} = \sum_{j=1}^{m} \left[\left(\frac{\partial q_{i,j}}{\partial \theta_y} - \frac{\partial q_{o,j}}{\partial \theta_y} \right) \mathbf{z}\left(j\right) \right] \tag{10.19}$$

The latter equations do not allow to find an immediate solution, therefore it is necessary to rework them in order to achieve an easy formulation for the partial derivatives. Those terms can be considerably simplified expanding the derivatives in more factors,

as follows:

$$\frac{\partial q_{i,j}}{\partial s_x} = \frac{\partial q_{i,j}}{\partial \mathbf{pen}_i(j)} \frac{\partial \mathbf{pen}_i(j)}{\partial s_x} \tag{10.20}$$

$$\frac{\partial q_{o,j}}{\partial s_x} = \frac{\partial q_{o,j}}{\partial \mathbf{pen}_o(j)} \frac{\partial \mathbf{pen}_o(j)}{\partial s_x} \tag{10.21}$$

$$\frac{\partial q_{i,j}}{\partial \theta_y} = \frac{\partial q_{i,j}}{\partial \mathbf{pen}_i(j)} \frac{\partial \mathbf{pen}_i(j)}{\partial \theta_y} \tag{10.22}$$

$$\frac{\partial q_{o,j}}{\partial \theta_y} = \frac{\partial q_{o,j}}{\partial \mathbf{pen}_o(j)} \frac{\partial \mathbf{pen}_o(j)}{\partial \theta_y} \tag{10.23}$$

Each factor in these formulas can be easily calculated analytically:

$$\frac{\partial q_{i,j}}{\partial \mathbf{pen}_i(j)} = \frac{1}{0.92} C_i \, \mathbf{pen}_i(j)^{1/0.92-1} \tag{10.24}$$

$$\frac{\partial q_{o,j}}{\partial \mathbf{pen}_o(j)} = \frac{1}{0.91} C_i \, \mathbf{pen}_o(j)^{1/0.91-1} \tag{10.25}$$

$$\frac{\partial \mathbf{pen}_i(j)}{\partial s_x} = -\frac{\partial \mathbf{pen}_o(j)}{\partial s_x} = -1 \tag{10.26}$$

$$\frac{\partial \mathbf{pen}_i(j)}{\partial \theta_y} = -\frac{\partial \mathbf{pen}_o(j)}{\partial \theta_y} = -\mathbf{z}(j) \tag{10.27}$$

$$\tag{10.28}$$

Substituting the Eq. (10.27)-(10.24) in Eq. (10.20)-(10.23) and then again in Eq. (10.16)-(10.19) the Jacobian formulation is finally achieved.

Obviously this kind of formulation returns reliable results just in case of positive penetration (i.e. bodies deformation), otherwise in case of negative values of the penetration it will return a complex value which is indeed physically meaningless.

Since the Jacobian is defined, the *Newton Raphson method* can be implemented. Then the usual formulation follows in Eq. (10.29), where k refers to the k-th iteration step.

$$\begin{bmatrix} s_x \\ \theta_y \end{bmatrix}_{k+1} = \begin{bmatrix} s_x \\ \theta_y \end{bmatrix}_k - \mathrm{J}_k^{-1} \begin{bmatrix} F_r \\ F_a \end{bmatrix}_k \tag{10.29}$$

The load distribution along the contact line obtained by the above-mentioned solution process is in general variable along the line of contact.

A case study is done using the following parameters:

Running the method the contact loads distribution shown in Figure 10.6 is obtained. The roller crowning and the inner ring displacement have been magnified for visualization and the centrifugal load has been visualized with the red arrow.

s_i	$2.8 \cdot 10^{-2}\ mm$
θ_i	$0.03°$
ω_{pw}	$1000\ rpm$

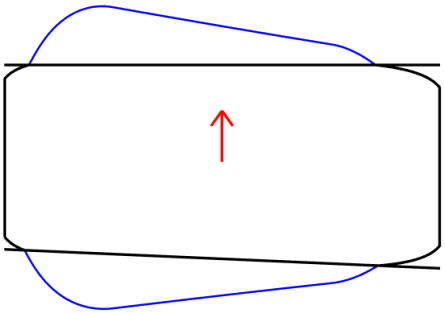

Figure 10.6: Load distribution along the contact lines

The roller behavior is now computed setting as inner raceway tilting $\theta_i = 0.03°$while varying the inner raceway approach s_i and the shaft rotational speed ω_{shaft}. The simulation results are shown in Figure 10.7, where with Meq_y and Feq_x are indicated the statically equivalent contact force and moment acting on the roller element.

It is clearly visible how the centrifugal load slightly affect the solution; in fact differences between different speeds are visible only in the first zone of the plots where there is no contact due to clearance. In that part the only non-zero load is the one between the roller and the outer raceway since it has to balance the centrifugal load. After all, since the centrifugal load does not increase the computational cost of the procedure, it has no sense to neglect it. Even if the differences are nearly negligible, it has sense to account for it, since it slightly decreases the reaction loads on the inner ring. This increased accuracy comes at no additional cost.

10.3.1 Solution Convergence Varying the Amount of Slices

The solution is affected by the number of slices used, as well as the computational cost. It is somehow predictable that increasing the number of slices, the solution for a given inner ring displacement will converge to a value. This can be shown plotting the statically equivalent forces and moments w.r.t. the center of gravity of the roller varying the number of slices. First the inner ring displacement has to be introduced as $s_i = 0.028\ mm$ and $\theta_i = 0.03°$, and then the statically equivalent force and moment are plotted as function of the amount of slices used. The obtained function is shown in Figure 10.8.

In this particular case the solution converges using at least 40 slices; increasing this number the solution remains almost the same while the computational effort increases.

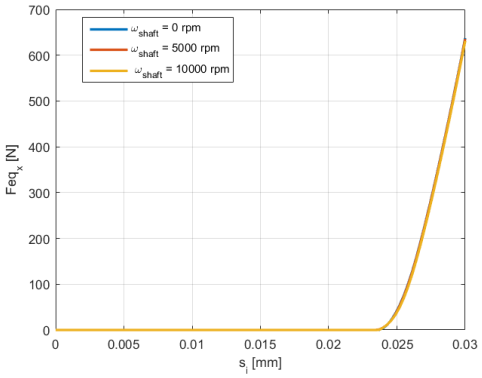

(a) Equivalent contact force between roller and inner raceway

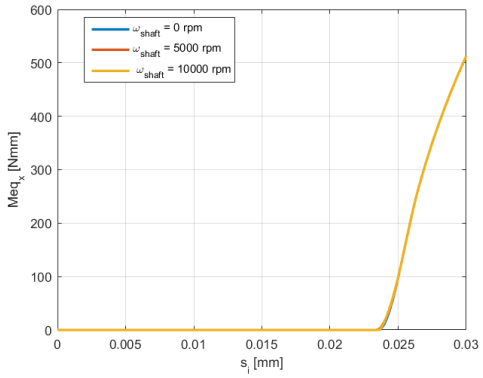

(b) Equivalent contact moment between roller and inner raceway

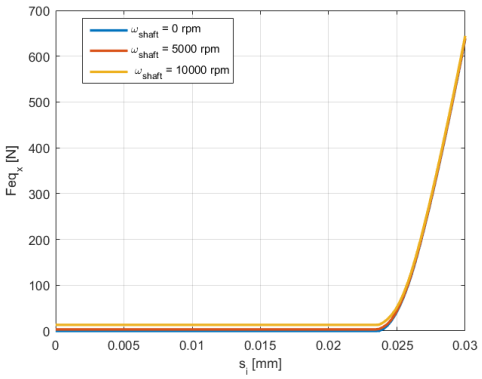

(c) Equivalent contact force between roller and outer raceway

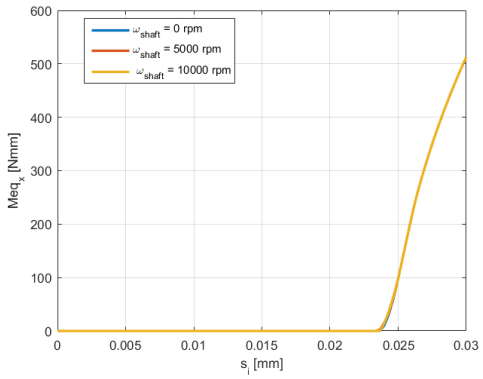

(d) Equivalent contact moment between roller and outer raceway

Figure 10.7: Statically equivalent contact forces and moments between roller and raceways, setting $\theta_i = 0.03°$ and accounting for centrifugal loads

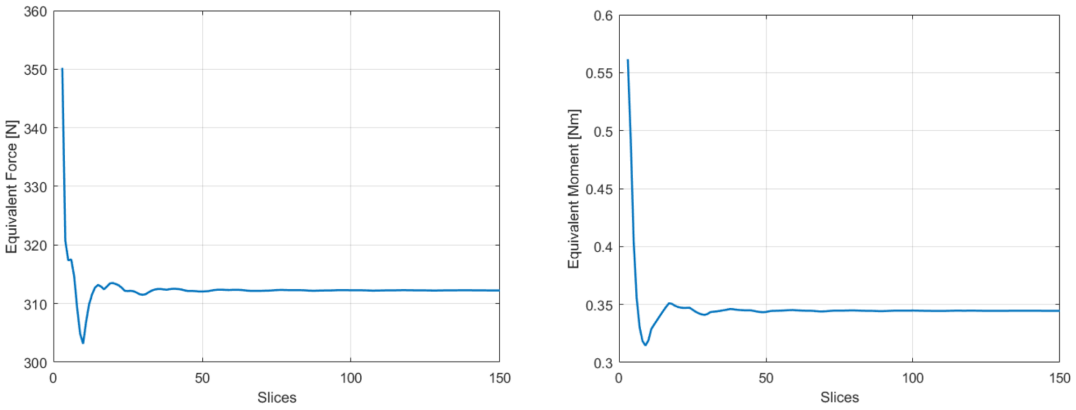

(a) Equivalent force

(b) Equivalent moment

Figure 10.8: Static equilibrium solution convergence as function of the amount of slices

Chapter 11

Radial Roller Bearing in EHL Contact

In almost all of the application cases of roller bearings and, more in line contact in general, the interface between the two bodies in contact is lubricated in order to reduce noise while increasing durability and reliability. Also in gears, seals, cams etc. the contact area is lubricated and they are designed to operate in specific lubrication regimes. Among the years many models have been developed to calculate the minimum film thickness in order to evaluate the correct design of the pair. The minimum lubricant film thickness has negligible effects for our purpose, while the key-role is played by the film thickness in the contact center, which defines the lubricant stiffness. An approximation of the central film thickness is proposed by *Gelink and Schipper* [28], which proposed a formulation fitting a function through the four lubrication regimes (isoviscous-rigid, pieziviscous-rigid, isoviscous-elastic, piezoviscous-elastic). To evaluate the combined lubricant-bodies effect an efficient methodology has been proposed by Wiegert et al. [31] where the contact is modeled as two springs in series, one representing the lubricant and one the solid bodies in contact. Less work has been done to investigate the load-deflection behavior of the contact with coupled fluid film-bodies effect.

Even so, an accurate solution can be computed modeling the contact as two springs in series.

11.1 EHL Line Contact Modeling

This section describes the model used to model the lubricated contact behavior. The roller is divided in several slices as described in Chapter 10 and for each slice the EHL contact model is applied to estimate the contact loads due to a given penetration coming from the current iteration step.

The lubricant fluid film thickness is estimated by the model proposed by *Gelink and Schipper* [28], while the coupling between lubricant and solid bodies behavior is modeled as two spring in series as proposed by Wiegert et al. [31]. As will be fully explained, since the fluid film behavior has a complex formulation, an iterative process

will be involved to compute the contact force for a given penetration.

11.1.1 Lubricant Fluid Film Behavior

As usual in tribology, the problem is formulated introducing dimensionless quantities, usually defined using *optimum similarity analysis*, which allow to determine the most efficient set of dimensionless parameters to model the problem. Usually, to avoid heavy calculations, pre-existing sets of parameters are used, as in this case in which the *Moes-Numbers* are used.

Moes-Numbers are then defined as follows [28]:

$$H_c = \overline{h}_c U^{-1/2},\ M = WU^{-1/2},\ L = GU^{-1/4} \tag{11.1}$$

Where [28]:

$$\overline{h}_c = \frac{h_c}{R_{eq}},\ W = \frac{q}{E_{eq}R_{eq}l},\ U = \frac{\eta_0 u_s}{E_{eq}R_{eq}},\ G = \alpha_{barus}E_{eq} \tag{11.2}$$

The formula developed by Gelink and Schipper can also account for the direction and the value of the surface roughness. This parameter is hard to estimate, and its effect is orders of magnitude smaller than many others effects which are not accounted for in this work. In fact, line contact modeling is more complex if compared with point contact modeling, since the side effects, lubricant leakage between slices and slice coupling are still phenomena which cannot be modeled in an analytic way.

Based on the Reynolds equation, Moes [27] made an accurate function fit to predict the central film thickness in line contact:

$$H_c = \left[\left(H_{RI}^{7/3} + H_{EI}^{7/3}\right)^{3/7\ s} + \left(H_{RP}^{-7/2} + H_{EP}^{-7/2}\right)^{-2/7\ s}\right]^{s^{-1}} \tag{11.3}$$

where s is an auxiliary variable defined as:

$$s = \frac{1}{5}\left(7 + 8\,\exp\left(-2\ H_{EI}/H_{RI}\right)\right) \tag{11.4}$$

in which the four basic asymptotes relevant in EHL are described as function of L and M.

$$H_{RI} = 3M^{-1} \tag{11.5}$$
$$H_{EI} = 2.621M^{-1/5} \tag{11.6}$$
$$H_{RP} = 1.287L^{2/3} \tag{11.7}$$
$$H_{EP} = 1.311M^{-1/8}L^{3/4} \tag{11.8}$$

In the latter equations the subscripts denote:

- RI: Rigid/Isoviscous;
- RP: Rigid/Piezoviscous

- EI: Elastic/Isoviscous
- EP: Elastic/Piezoviscous

By Eq. (11.3) the load-fluid film thickness relation for the lubricant is defined; since the lubricant behavior is been defined, now a model to describe the bodies deformation has to be introduced. Therefore merging the two models the contact behavior will be described.

11.1.2 Solid Bodies Behavior

The bodies behavior results from the pressure distribution through the fluid film. In case of zero speed the model corresponds to the one developed in Chapter 10, while in case of surfaces velocity the lubricant plays a key role to determine the pressure distribution.

For zero or even negative penetration, as the surfaces velocity increases, the solid bodies compliance cannot be neglected, even if the lubricant separates the surfaces from each other. This can be proven solving the Reynolds equations accounting for lubricant piezoviscosity while neglecting the bodies compliance. The result is a narrow and high pressure peak, of which the maximum value exceeds the values which no longer allows to neglect the body compliance. A qualitative example of this solution is shown in Figure 11.1.

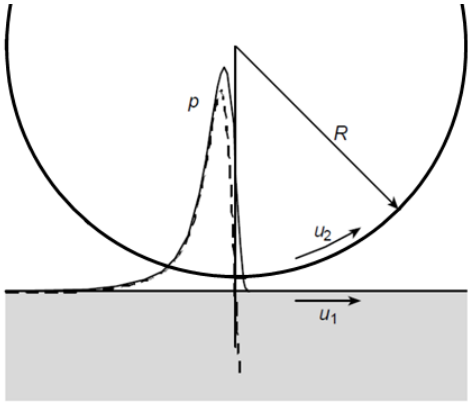

Figure 11.1: Pressure distribution under of RP and RI hypothesis

Accounting for surface deformation, the solution is similar to what is described in Chapter 6. The roller deformed shape changes depending on the dimensionless parameters (11.2). When varying for example the load dimensionless parameter W, the deformed shape of the roller surface and the pressure distribution will be as shown in Figure 11.2.

First of all, it can be noticed that load variations barely affect the film thickness: between the case (**1**) and the case (**2**) in Figure 11.2 the load is increased by a factor of 20, while the film thickness decreases by a factor of 0.33. Furthermore:

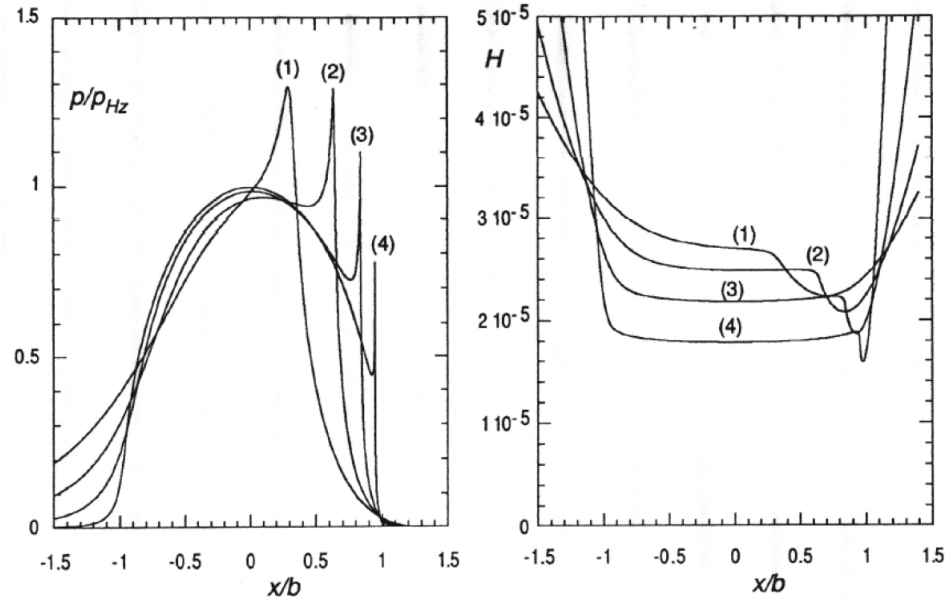

Figure 11.2: Pressure distribution and fluid film thickness in case of: $U = 10^{11}$, $G = 5000$ and: $(\mathbf{1})W = 10^{-5}$, $(\mathbf{2})W = 2 \cdot 10^{-5}$, $(\mathbf{3})W = 5 \cdot 10^{-5}$, $(\mathbf{4})W = 2 \cdot 10^{-4}$. [41]

- Increasing the load, the pressure distribution tends to fit the Hertian one (excluding the outlet peak), while reducing the load, the pressure distribution approximate the isoviscous-rigid one;
- As the load increases, the outlet pressure peak reduces its maximum value, becomes narrower and moves closer to the outlet.

A similar effect is observable varying U or G, the peak moves to the outlet, getting narrower and smaller as the parameters increase.

Due to the similarity between Hertian pressure distribution and EHL pressure distribution, the solid body behavior is described using the dry contact introduced in Chapter 10. This deformation will be used to correlate the penetration with the fluid film thickness described by Eq. (11.3).

11.1.3 Contact Solution

As contact solution input the penetration is given, the corresponding contact force for each slice has to be computed, as well as his derivative w.r.t. the penetration.

In equilibrium, the penetration is overcome by the solid bodies deformation, while accounting for the additional surface separation due to the fluid film thickness, and while respecting the equality of the loading onto the solid and the lubricant.

The penetration can be written as function of fluid film thickness and roller deformation, referring to Figure 11.3, penetration, fluid film thickness and solid bodies relation can be written as in Eq. (11.9) and Eq. (11.10).

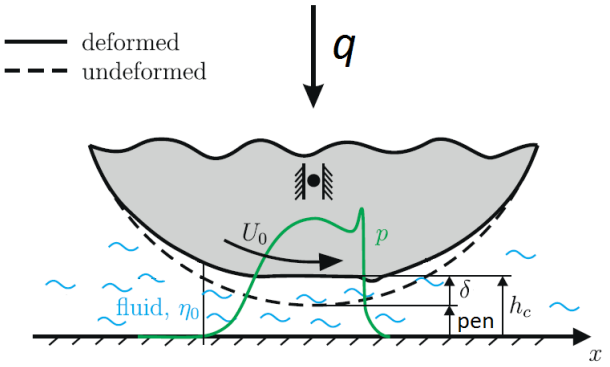

Figure 11.3: Contact penetration arrangement. [31]

$$\mathbf{pen}_i(j) \;=\; \delta_{i,j} - h_{c_{i,j}} - \mathbf{CrownDrop} \;=\; C_i^{-0.92}\, q_{i,j}^{0.92} - H_{c_{i,j}} U_{i,j}^{-1/2} R_{i,eq} - \mathbf{CrownDrop} \tag{11.9}$$

$$\mathbf{pen}_o(j) \;=\; \delta_{o,j} - h_{c_{o,j}} - \mathbf{CrownDrop} \;=\; C_o^{-0.91}\, q_{i,j}^{0.91} - H_{c_{o,j}} U_{o,j}^{-1/2} R_{o,eq} - \mathbf{CrownDrop} \tag{11.10}$$

Where the Dinnik's contact model equations (10.12) and (10.13) have been introduced as well as Eq. (11.3). In the solution the above-mentioned equations cannot be used directly since the inverse formulation is required. Due to the complex formulation of H_c, the inverse function of Eq. (11.9) and Eq. (11.10) have to computed using an iterative process, thus the *Newton-Raphson method* is used again.

The function which has to be solved can be written starting from the definition of the penetration, for example for the slice-inner raceway contact, it reads:

$$f_{i,j}(q_{i,j}) \;=\; \delta_{i,j} - h_{c_{i,j}} - \mathbf{pen}_i(j) - \mathbf{CrownDrop} \tag{11.11}$$

The same can be done for the slice-outer raceway contact, defining $f_{o,j}(q_{o,j})$. To implement the iterative method the derivative of f w.r.t. the contact force has to be calculated:

$$\frac{\partial f_{k,j}(q_{k,j})}{\partial q_{k,j}} \;=\; \frac{\partial \delta_{k,j}}{\partial q_{k,j}} - \frac{\partial h_{c_{k,j}}}{\partial q_{k,j}}, \quad k \;=\; i, o \tag{11.12}$$

The derivatives of $\mathbf{pen}_i(j)$ and $\mathbf{pen}_o(j)$ are zero, since they are constant, while the term derived form the Dinnik's formulation becomes:

$$\frac{\partial \delta_{i,j}}{\partial q_{i,j}} \;=\; 0.92\; C_i^{-0.92}\; q_{i,j}^{0.92-1} \tag{11.13}$$

$$\frac{\partial \delta_{o,j}}{\partial q_{o,j}} \;=\; 0.91\; C_o^{-0.91}\; q_{o,j}^{0.91-1} \tag{11.14}$$

Concerning the terms $\partial h_{c_{i,j}}/\partial q_{i,j}$ and $\partial h_{c_{o,j}}/\partial q_{o,j}$, the derivative can not be calculated manually, since $q_{k,j}$ is located also in the exponent of the exponential function. This derivative has been calculated using a symbolic tool. Finally, the iterative process can be formulated as follows:

$$q_{i,j_{k+1}} = q_{i,j_k} + \frac{f_{i,j}(q_{i,j_k})}{f'_{i,j}(q_{i,j_k})}, \quad k = 1, ... \tag{11.15}$$

$$q_{o,j_{k+1}} = q_{o,j_k} + \frac{f_{o,j}(q_{o,j_k})}{f'_{o,j}(q_{o,j_k})}, \quad k = 1, ... \tag{11.16}$$

11.2 Roller Equilibrium Accounting for EHL and Centrifugal Loads

The rolling element equilibrium can be computed using the same procedure described in Section 10.3. The only difference is situated in the terms $\partial q_{i,j}/\partial \mathbf{pen}_i\,(j)$ and $\partial q_{o,j}/\partial \mathbf{pen}_o\,(j)$ which are now composed of two different terms, one related to the lubricant stiffness and one related to the solid bodies stiffness.

According with Wiegert et al. [31] each single contact can be modeled as two springs in series, as showed in Figure 11.4.

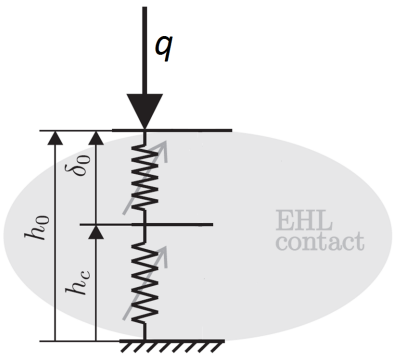

Figure 11.4: Force model of EHL contact. [31]

In order to compute the local stiffness in a defined configuration, one needs to calculate the two separate stiffnesses and then combine them.

Starting from Eq. (11.12) it can be seen how the total equivalent compliance can be read as the sum of the compliance of both contributions. The compliance itself is the inverse of the stiffness. Hence the contact stiffness can be calculated by simply computing the inverse of Eq. (11.12), hence:

$$\frac{\partial q_{i,j}}{\partial \mathbf{pen}_i(j)} = \left(\frac{\partial \delta_{i,j}}{\partial q_{i,j}} - \frac{\partial h_{c_{i,j}}}{\partial q_{i,j}}\right)^{-1} \tag{11.17}$$

$$\frac{\partial q_{o,j}}{\partial \mathbf{pen}_o(j)} = \left(\frac{\partial \delta_{o,j}}{\partial q_{o,j}} - \frac{\partial h_{c_{o,j}}}{\partial q_{o,j}}\right)^{-1} \tag{11.18}$$

This formulation is moreover convenient since the value of any term in the above-mentioned equations is already calculated during the process to compute the contact force. Therefore this calculation does not requires any additional computational effort.

Once the contact stiffness is computed, the iterative process can take place using the equations described in Section 10.3. In this case the process is indeed more time consuming, due to the iterative processes involved to compute the contact forces.

The roller shape is still the one introduced in Section 10.2, the parameter u_s which quantify the surfaces speed is calculated alike what is described in Section 6.2. A case study was done using the parameters in Table 11.1.

s_i	$2.8 \cdot 10^{-2}\ mm$
θ_i	$0.03°$
ω_{pw}	$1000\ rpm$

Table 11.1: Showcase parameters

The developed methodology returns the qualitative picture shown in Figure 11.5 where the centrifugal load applied in the center of gravity is shown in red, and the contact forces distribution in blue. The crowning and the fluid film thickness between the surfaces have been magnified for visualization.

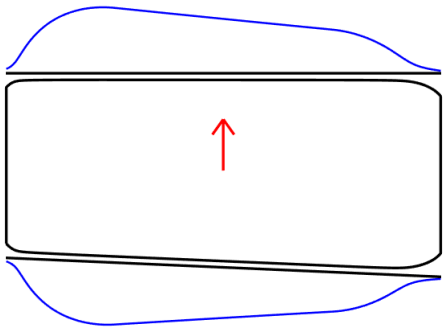

Figure 11.5: Load distribution along the contact lines

It is interesting how, even if the surfaces are relatively far from each other, a certain amount of force is still visible. Moreover it is visible how the bodies do not get in contact because of the lubricant film. Which explains why the contact forces are higher than the ones in the dry case, for the same inner ring displacement.

The roller behavior is now computed setting as inner raceway tilting $\theta_i = 0.03°$while varying the inner raceway approach s_i and the shaft rotational speed ω_{shaft}. The simulation results are shown in Figure 11.6, where with Meq_y and Feq_x indicate the equivalent contact force and moment acting on the rolling element. It can be seen how the roller-outer raceway contact becomes slightly greater than the roller-inner raceway contact due to the centrifugal load which becomes non-negligible as the shaft speed increases.

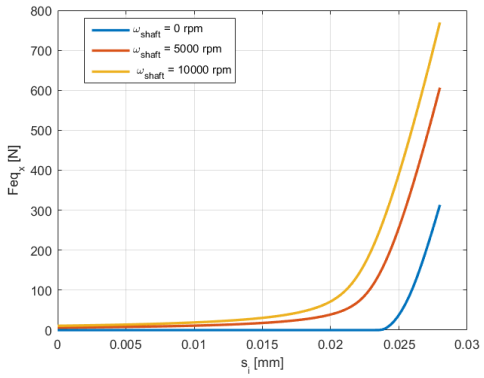

(a) Equivalent contact force between roller and inner raceway

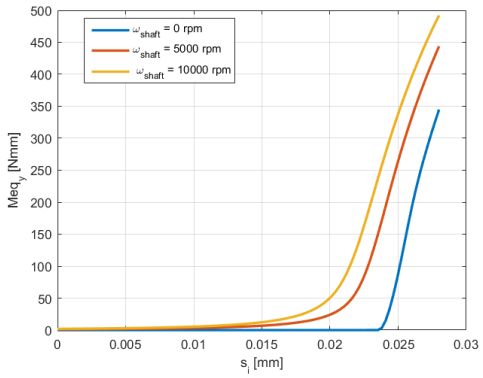

(b) Equivalent contact moment between roller and inner raceway

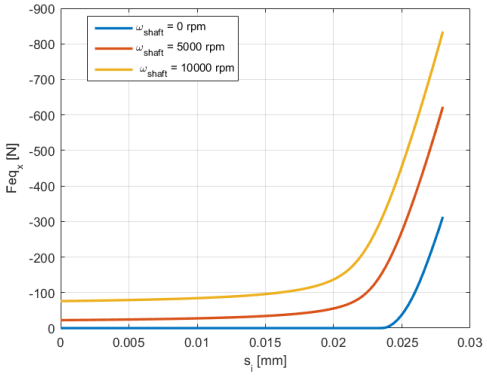

(c) Equivalent contact force between roller and outer raceway

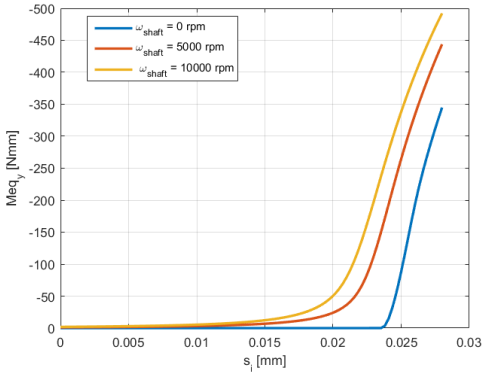

(d) Equivalent contact moment between roller and outer raceway

Figure 11.6: Statically equivalent contact forces and moments between roller and raceways setting $\theta_i = 0.03°$and accounting for centrifugal loads and EHL

Furthermore, as the speed increases, the contact loads increase too, since the lubricant effect becomes more significant. Therefore the roller is squeezed between the raceways with greater forces as the velocity increases. This will have a considerable effect on the whole roller bearing behavior.

Comparing Figure 11.6 with Figure 10.7, it is clearly visible how the model fidelity of the dry case decreases as ω_{shaft} increases. However, the increase in model fidelity of the EHL case comes at an increased computation effort.

11.3 Solution Convergence Varying the Amount of Slices

As done in Section 10.3.1 the solution convergence varying the amount of slices used to describe the roller will now be studied. A smoother convergence is expected, due to the more continuous contact behavior. In fact, because of the lubrication, the contact force

is defined even if the penetration is greater than zero. In case of dry contact, when the slice gets in contact with the raceway, it suddenly transmits a contact force. Whereas if one accounts for lubrication, even if the surfaces are far from each other, a certain amount of force is still defined, smoothening the contact behavior.

As done in dry case, the inner ring displacement is set as $s_i = 0.028\ mm$ and $\theta_i = 0.03°$, while the amount of slices used is kept as variable. The equivalent force and moment is then computed, as function of the amount of slices as Figure 11.7 shows.

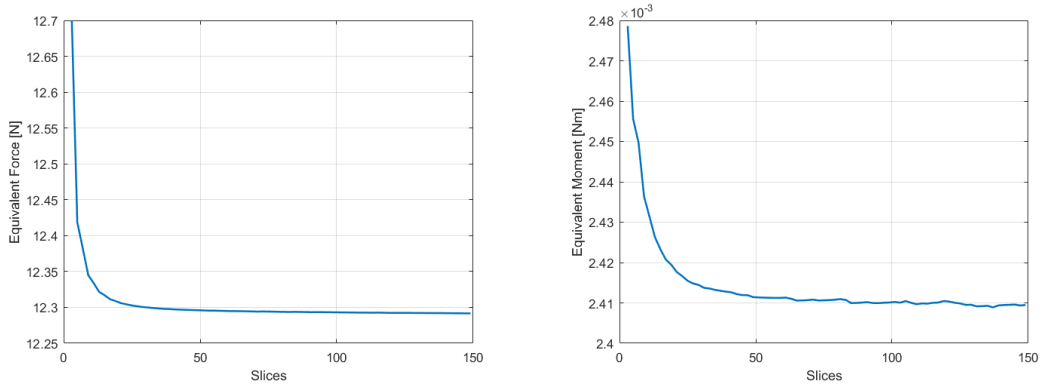

(a) Equivalent force

(b) Equivalent moment

Figure 11.7: Static equilibrium solution convergence as function of the amount of slices

In this case, the convergence is indeed smoother as compared to the dry case, even if the curves trend is similar to the trend of Figure 10.8. In case of lubricated contact, even for low amount of slices the solution is already reliable, since between the converged value and the value for low amount of slices there is only a slight difference ($\leq 5\%$). This allows a coarser roller discretization which drastically reduces the required computational effort.

Chapter 12

Tapered Roller Bearing

An important type of roller bearing is indeed represented by the *Tapered Roller Bearings* which allow both high radial loads and high axial loads due to their design. The roller shape is then a truncated cone since the axis of rotation is no more parallel to the bearing axis but it forms an angle which value is between 0°(radial roller bearing) and 90°(thrust roller bearing).

Tapered roller bearing are used, for example, combined with radial roller bearings in order to allows for high radial loads while being in charge of axial load carrying. The contact models used for tapered rollers are the same as the ones developed for radial rollers in Chapter 10 and Chapter 11, while the definition of penetration and the roller equilibrium changes due to the different geometry. As will be shown the tapered roller equilibrium is still 2-D but the flange will introduce one more variable to the problem.

12.1 Tapered Roller Geometry

In this section the tapered roller is introduced, Figure 12.1 shows the roller geometry. As shown, the roller configuration can be defined by the two angles α and β which are respectively the contact angle and the roller angle.

Since the roller is tapered, the roller diameter D is defined as a function of the vector $\mathbf{z}$ which still represent the roller axial coordinate. Naming D_m the roller mean diameter, the vector $\mathbf{D}$ which collect the diameters corresponding to each slice, is defined as:

$$\mathbf{D} = \frac{D_m}{2} + \mathbf{z}\frac{D_g - D_l}{L} \tag{12.1}$$

Where D_g and D_l are respectively the major roller radius and the minor roller radius. Since the roller diameter is variable, all the radius of curvature are function of $\mathbf{z}$ so the equations mentioned in the previous chapters have increased their complexity even if they are substantially still equivalent, then in order to streamline the text they are not mentioned again.

The roller angle β can be easily calculated by:

$$\beta = 2\text{atg}\left(\frac{D_g - D_l}{2L}\right) \tag{12.2}$$

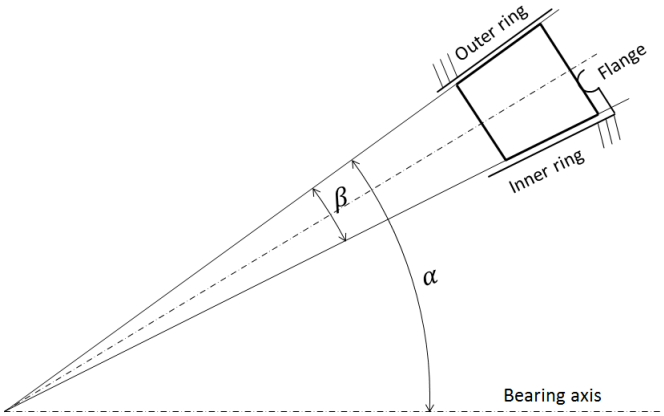

Figure 12.1: Tapered roller geometry

The outer ring thickness vector $\mathbf{t}$, which has to be used in Eq. 10.4 can be only approximated since the exact geometry has to be known, therefore an approximate formulation is proposed, it works well with contact angles α up to $40 - 50°$. Otherwise a more precise formulation has to be introduced. It is defined as follows:

$$\mathbf{t} = \frac{D_{ob} - D_{pw}}{2} - \frac{\mathbf{D}}{2\cos(\alpha - \beta/2)} + \mathbf{z}\ \mathrm{tg}(\alpha - \beta/2) \tag{12.3}$$

Due to the outer ring conformation, the clearance is not defined. In fact the tapered bearings structure can support only unidirectional axial loads, otherwise the outer ring gets dismounted.

12.1.1 Tapered Roller Equilibrium

As above-mentioned, the roller equilibrium becomes more complex introducing the flange effect and the tapered shape of the roller. Since the inner ring approach s_i is no more along the radial direction, the axial and the radial inner ring approach are introduced again, as usual they are named respectively δ_a and δ_r. By this two parameters the inner raceway translation perpendicular to the raceway surface can be computed as follows:

$$s_i = \delta_r \cos(\alpha - \beta) + \delta_a \sin(\alpha - \beta) \tag{12.4}$$

while θ_i comes directly from the inner ring displacement since it is still along the same direction defined for radial roller bearings.

The roller position is defined as usual by the coordinates s_x and θ_y as shown in Figure 12.3 where is also shown the centrifugal force F_c which is no more applied on the roller mean plane due to the tapered shape, moreover is shown the flange contact force F_{fl} which act at a distance of d_fl from the roller axis.

In this model the flange effect is modeled as a force, which means that the roller is not able to move along its axis. This assumption has negligible effects since the flange-roller real contact induces small movements along the roller's axis, since F_{fl} is usually

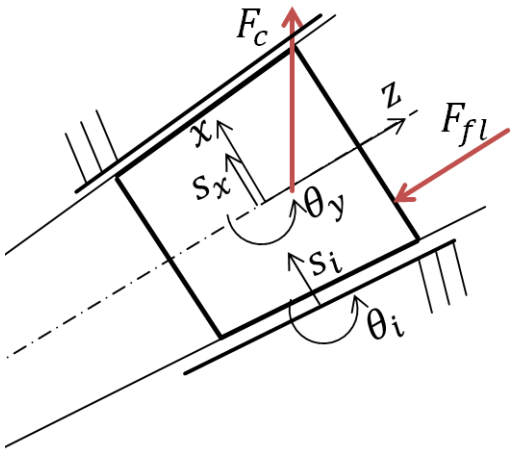

Figure 12.2: Tapered roller equilibrium

few orders of magnitude smaller than the contact forces between the roller and the raceways. On the other hand it has to be taken into account since provokes a moment which can slightly change the load distribution between the raceways.

Since the centrifugal load is no more applied to the roller center, if the roller equilibrium is computed w.r.t. the roller center, it provokes also a moment. Then the total centrifugal load is considered as a load distribution among the slides. Then each slice will have his own centrifugal load. Collecting all the centrifugal loads in one vector, hence $\mathbf{f}_c(j)$, it can be computed as follows:

$$\mathbf{f}_c = \omega_{pw_j}^2 \frac{D_{pw,j}\ \mathrm{d}m_j}{2} \tag{12.5}$$

where $\mathrm{d}m_j$ is the mass of the j-th slice, $D_{pw,j}$ is the pitch diameter of the j-th slice and ω_{pw_j} is the rotational speed of the pitch diameter of the j-th slice.

Due to the angle β and the flange contact force, one more equation has to be introduced at the equilibrium as well as one more unknown is inside these equations.

They can be written as follows:

$$\begin{cases} F_x &= \sum_{j=1}^{m} (q_{i,j} - q_{o,j}) \cos(\beta/2) + \sum_{j=1}^{m} \mathbf{f}_c(j) \cos(\alpha - \beta/2) &= 0 \\ F_z &= \sum_{j=1}^{m} (q_{i,j} + q_{o,j}) \sin(\beta/2) + \sum_{j=1}^{m} \mathbf{f}_c(j) \sin(\alpha - \beta/2) - F_{fl} &= 0 \\ M_y &= \sum_{j=1}^{m} [(q_{i,j} - q_{o,j}) \mathbf{z}(j)] \cos(\beta/2) + \sum_{j=1}^{m} \mathbf{f}_c(j) \mathbf{z}(j) \cos(\alpha - \beta/2) & \\ & \quad + \sum_{j=1}^{m} \left[(q_{i,j} - q_{o,j}) \sin(\beta/2) \frac{\mathbf{D}(j)}{2} \right] - F_{fl} d_{fl} + M_g &= 0 \end{cases} \tag{12.6}$$

where M_g is the gyroscopic moment due to the roller rotation around two incidence straight lines. It can be computed as proposed by Harris and Kotzlas [12] which proposed the following formulation:

$$M_g = 8.37 \cdot 10^{-12} \left(D_m \cdot 10^{-3}\right)^4 \left(L \cdot 10^{-3}\right) \left(\omega_{pw} \frac{60}{2\pi}\right) \left(\omega_{roll} \frac{60}{2\pi}\right) \sin(\alpha - \beta/2) \tag{12.7}$$

To introduce the iterative method to compute the solution of the Eq. (12.6) the partial derivatives of these equations have to be computed w.r.t. s_x, θ_y and F_{fl} which represent the unknowns. Then the derivatives are:

$$\frac{\partial F_x}{\partial s_x} = \sum_{j=1}^{m} \left(\frac{\partial q_{i,j}}{\partial s_x} - \frac{\partial q_{o,j}}{\partial s_x} \right) \cos(\beta/2) \tag{12.8}$$

$$\frac{\partial F_y}{\partial s_x} = \sum_{j=1}^{m} \left(\frac{\partial q_{i,j}}{\partial s_x} + \frac{\partial q_{o,j}}{\partial s_x} \right) \sin(\beta/2) \tag{12.9}$$

$$\frac{\partial M_y}{\partial s_x} = \sum_{j=1}^{m} \left(\frac{\partial q_{i,j}}{\partial s_x} - \frac{\partial q_{o,j}}{\partial s_x} \right) \mathbf{z}(j) \cos(\beta/2) \tag{12.10}$$

$$\frac{\partial F_x}{\partial \theta_y} = \sum_{j=1}^{m} \left(\frac{\partial q_{i,j}}{\partial \theta_y} - \frac{\partial q_{o,j}}{\partial \theta_y} \right) \cos(\beta/2) \tag{12.11}$$

$$\frac{\partial F_y}{\partial \theta_y} = \sum_{j=1}^{m} \left(\frac{\partial q_{i,j}}{\partial \theta_y} + \frac{\partial q_{o,j}}{\partial \theta_y} \right) \sin(\beta/2) \tag{12.12}$$

$$\frac{\partial M_y}{\partial \theta_y} = \sum_{j=1}^{m} \left(\frac{\partial q_{i,j}}{\partial \theta_y} - \frac{\partial q_{o,j}}{\partial \theta_y} \right) \mathbf{z}(j) \cos(\beta/2) \tag{12.13}$$

$$\frac{\partial F_x}{\partial F_{fl}} = 0 \tag{12.14}$$

$$\frac{\partial F_y}{\partial F_{fl}} = -1 \tag{12.15}$$

$$\frac{\partial M_y}{\partial F_{fl}} = d_{fl} \tag{12.16}$$

The above-mentioned equations can be handled as explained in Section 10.3 with the only difference in the partial derivatives of the penetration, since the penetration vectors have to be modified due to the roller angle β which change the contact normal vector. By simple mathematical steps the following formulation is achieved:

$$\begin{aligned}\mathbf{pen}_i = & -\mathbf{z}\theta_y \cos(\beta/2) + \frac{\mathbf{D}}{2}\theta_y \sin(\beta/2) - s_x \cos(\beta/2) \\ & +\delta_r \cos(\alpha - \beta/2) + \delta_a \sin(\beta/2) + \mathbf{z}\theta_i - \mathbf{CrownDrop}\end{aligned} \tag{12.17}$$

$$\mathbf{pen}_o = \mathbf{z}\theta_y \cos(\beta/2) - \frac{\mathbf{D}}{2}\theta_y \sin(\beta/2) + s_x \cos(\beta/2) - \mathbf{CrownDrop} \tag{12.18}$$

which leads to the following formulation concerned the derivatives:

$$\frac{\partial \mathbf{pen}_i(j)}{\partial s_x} = -\frac{\partial \mathbf{pen}_o(j)}{\partial s_x} = -\cos(\beta/2) \tag{12.19}$$

$$\frac{\partial \mathbf{pen}_i(j)}{\partial \theta_y} = -\frac{\partial \mathbf{pen}_o(j)}{\partial \theta_y} = -\mathbf{z}\cos(\beta/2) + \frac{\mathbf{D}}{2}\sin(\beta/2) \tag{12.20}$$

Than the Jacobian matrix can be built in the following form:

$$\mathbf{J} = \begin{bmatrix} \frac{\partial F_x}{\partial s_x} & \frac{\partial F_x}{\partial \theta_y} & \frac{\partial F_x}{\partial F_{fl}} \\ \frac{\partial F_z}{\partial s_x} & \frac{\partial F_z}{\partial \theta_y} & \frac{\partial F_z}{\partial F_{fl}} \\ \frac{\partial M_y}{\partial s_x} & \frac{\partial M_y}{\partial \theta_y} & \frac{\partial M_y}{\partial F_{fl}} \end{bmatrix} \tag{12.21}$$

Finally the iterative process is formalized as:

$$\begin{bmatrix} s_x \\ \theta_y \\ F_{fl} \end{bmatrix}_{k+1} = \begin{bmatrix} s_x \\ \theta_y \\ F_{fl} \end{bmatrix}_k \mathbf{J}_k^{-1} \begin{bmatrix} F_x \\ F_x \\ M_y \end{bmatrix}_k \tag{12.22}$$

A solution is then computed introducing the parameters in Table 12.1. The solution is computed for both dry and EHL contact models, since the contact models are alike the ones used for cylindrical roller bearings.

Achieving the qualitative results shown in Figure 12.3 where as usual the crowning and the penetration are magnified for visualization; the blue arrow represent the flange contact force, while the red one the centrifugal load.

δ_a	$0\ mm$
δ_r	$0.01\ mm$
θ_i	$-0.02°$
ω_{pw}	$1000\ rpm$
α	$6°$
β	$0.046°$

Table 12.1: Showcase parameters

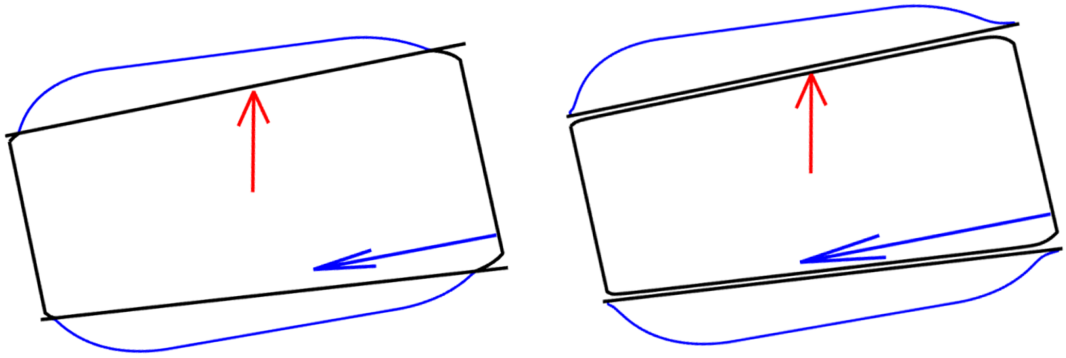

(a) Equivalent force (b) Equivalent moment

Figure 12.3: Tapered roller equilibrium in Dry and EHL lubricated case, where crowning and displacements are magnified for visualization

Is interesting to notice how, even if the axial displacement of the inner ring is zero, the flange is still carrying a certain load due to the β angle which induce a load in z direction which has to be balanced by the flange.

Moreover Figure 12.3 shows how the surfaces of the rolling element and the raceways do not get in contact in the EHL case because of the lubricant thin layer between the them, while in dry case the surfaces get in contact. Another lubricant effect can be seen in the load distribution which in the EHL case is greater than the dry case since the solid bodies deformation has to be grater in order to allow the lubricant layer between the surfaces. In particular, in lubricated case, even if the surfaces are relatively far from each others a certain amount of load is still defined.

Now the tapered roller equilibrium is computed, both in dry contact and in EHL field. This is useful to compare the results pointing out which are the advantages and disadvantages of each model, exactly as has been done for the radial roller bearings. First some parameters are introduced in Table 12.2.

Figure 12.4 shows the behavior of the statically equivalent forces and moments which the raceways do on the roller.

Similar to the case of radial roller in dry contact, the shaft speed do not have a huge influence on the tapered roller behavior, since due to the high contact stiffness it becomes quickly negligible. Anyway it do not increases the computational cost. Is also

δ_a	$1 \cdot 10^{-3}\ mm$
θ_i	$0.02°$
α	$6°$
β	$0.046°$

Table 12.2: Tapered roller showcase parameters

visible how the flange works in order to keep the roller between the raceways, which in case of absence of the flange would be pushed out of the bearing due to the β angle.

Comparing Figure 12.4 with Figure 10.7 is clearly visible how the tapered roller has less stiffness, due to the displacement δ_r which is not along the contact direction but it is reduced by the contact angle α and the roller angle β.

The same solution can be computed for the EHL case, still introducing the displacements from Table 12.2. Figure 12.5 shows the solution achieved.

In EHL regime the shaft speed has a big influence on the solution, in fact increasing the shaft speed, the centrifugal force indeed increases, but the biggest effect on the contact force is due to the greater surfaces speed which lead to an increased lubricant effect. Is clearly visible how the plots translate while in the dry case the curves are almost overlapped. Furthermore is clear how, as usual, the dry case underestimate the contact forces.

12.2 Solution Convergence Varying the Amount of Slices

The solution convergence varying the amount of slices used is not computed, since the contact models used for tapered roller bearings are the same used in radial roller bearings, thus the behavior will be the same since the only difference is the set of equations to compute the roller equilibrium.

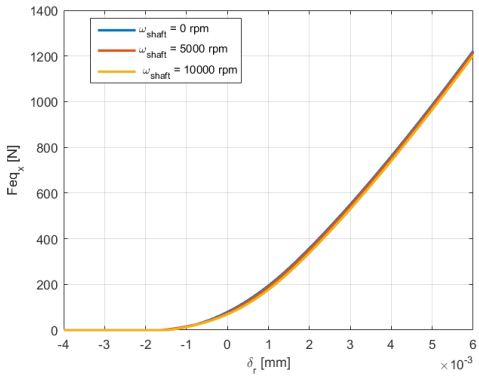

(a) Equivalent contact force between roller and inner raceway

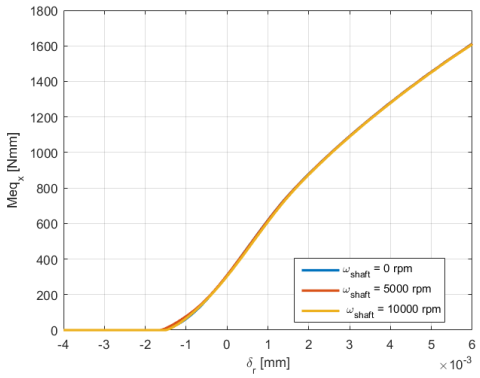

(b) Equivalent contact moment between roller and inner raceway

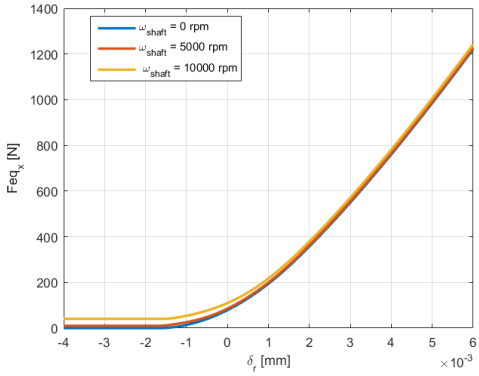

(c) Equivalent contact force between roller and outer raceway

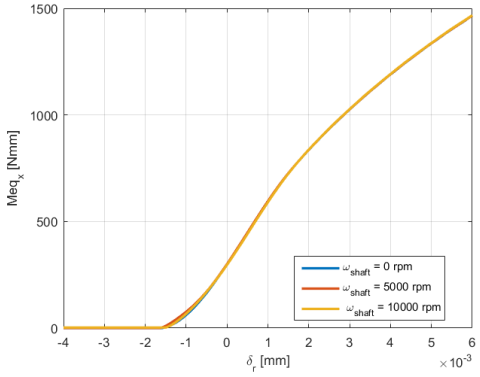

(d) Equivalent contact moment between roller and outer raceway

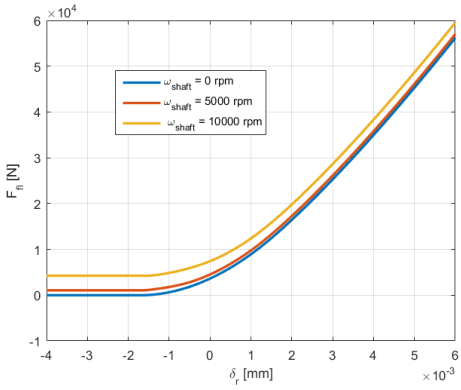

(e) Flange-roller contact force

Figure 12.4: Contact statically equivalent forces and moments between roller and raceways and between roller and flange in dry case

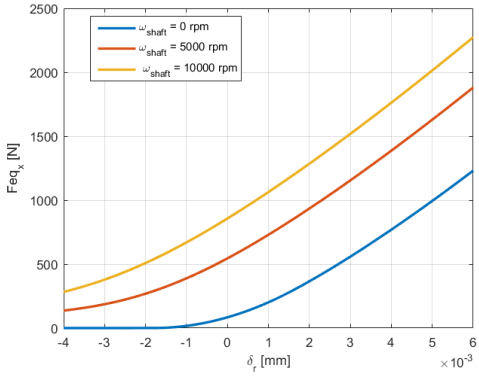

(a) Equivalent contact force between roller and inner raceway

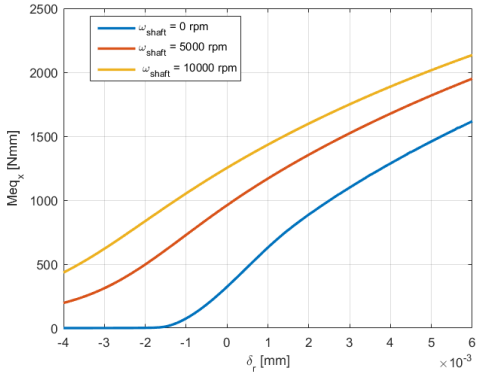

(b) Equivalent contact moment between roller and inner raceway

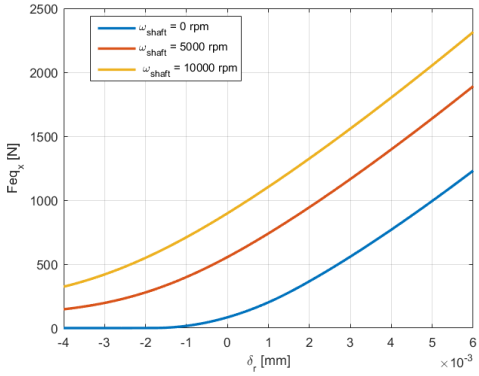

(c) Equivalent contact force between roller and outer raceway

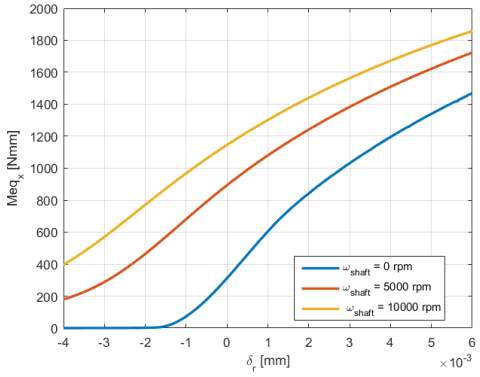

(d) Equivalent contact moment between roller and outer raceway

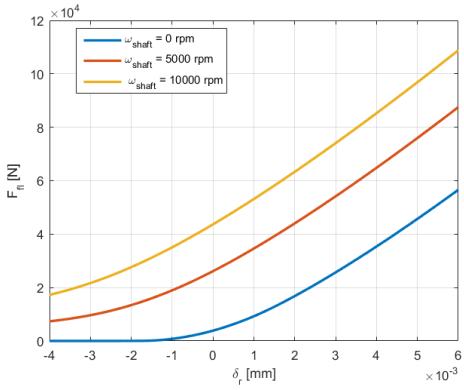

(e) Flange-roller contact force

Figure 12.5: Contact statically equivalent forces and moments between roller and raceways and between roller and flange in EHL regime

Chapter 13

Roller Bearing Behavior

The procedure explained in this chapter is based on what has been developed in Chapter 7, since many steps are exactly the same. The main differences are related to the contact wrench vector which in this case has two different components: the statically equivalent force F_x and the statically equivalent moment M_y. Also the local displacement has one more component, since in order to define the local inner ring displacement, two parameters have to be defined: the translation approach s_i in case of cylindrical roller bearings or δ_a and δ_r in case of tapered roller bearings, while the second parameter is the same in both cases and it is the local inner ring rotation θ_i. Since the developed procedure is general, is easy to adapt it to each case.

13.1 From Global to Local Displacements

In this section is explained how the procedure developed in Chapter 7 is adapted to roller bearings and tapered roller bearings.

The definition of global and local coordinate system is still the same and they are shown in Figure 13.1 for a tapered bearing.

The local deflection in case of radial roller bearings is formalized as follows:

$$s_i = \delta_x \cos\psi + \delta_y \sin\psi \tag{13.1}$$

$$\theta_i = \mathbf{R}_{gl}^T(2,:) \begin{bmatrix} \gamma_x & \gamma_y & 0 \end{bmatrix}^T \tag{13.2}$$

Where with $\mathbf{R}_{gl}^T(2,:)$ is pointed out the second row of the matrix, since the inner ring rotation around the x and z axis do not have effects on the model. While in case of tapered roller bearings the reference radius has to be defined. The reference radius fix the distance between the bearing axis and the local coordinate system. The mentioned radius is defined as follows:

$$r_{ref} = r_{pw} - \frac{D_g - D_l}{2} \cos\left(\alpha - \beta/2\right) \tag{13.3}$$

then the local displacements as:

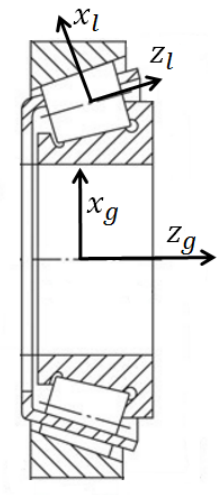

Figure 13.1: Global and local coordinate system in tapered roller bearings

$$\delta_r = \delta_x \cos\psi + \delta_y \sin\psi \tag{13.4}$$
$$\delta_a = -\left[\delta_z + r_{rif}\left(\gamma_x \sin\psi - \gamma_y \cos\psi\right)\right] \tag{13.5}$$

13.2 From Local to Global Loads

The procedure to calculate the contribution of each rolling element to the global bearing behavior is exactly the same as described in Chapter 7, the only difference is in the local wrench vector which in this case is composed by two components:

$$^{j}w = \begin{bmatrix} ^{j}F_x & 0 & 0 & 0 & ^{j}M_y & 0 \end{bmatrix}^T \tag{13.6}$$

13.3 Cylindrical Roller Bearing Behavior

This section shows how a cylindrical roller bearing (Figure 13.5) behaves when a certain displacement is applied st the inner ring. The procedure and the hypothesis are the ones mentioned in Chapter 7. To compute the solution is taken as showcase the bearing *NU 1010 ECP* from SKF, as done for angular contact ball bearing the internal geometry is estimated using the norms [36] and [35], therefore the estimated values are shown in Table 13.1.

The solution is then computed introducing the displacements in Table 13.2 where δ_z is set as zero since it do not affect the solution due to assumptions done.

The shaft speed rotation starts from 0 *rpm* and it goes up to 10000 *rpm* with an intermediate step at 5000 *rpm*. The shaft rotation angle is given in order to have a cage rotation of 180°, even if a minor rotation angle would be sufficient since is expected a behavior periodicity of $360°/Z = 20°$.

Figure 13.2: Cylindrical Roller Bearing

B	16 mm	Outer ring width
D_{ob}	80 mm	Outer bore diameter
D_{ib}	50 mm	Inner bore diameter
D	5.69 mm	Roller diameter
L	10 mm	Roller length
t	7.16 mm	Outer ring thickness
$clnc$	0.05 mm	Radial clearance
D_{pw}	60 mm	Pitch diameter
Z	18	Number of rolling elements
E	206 GPa	Young modulus
ν	0.3	Poisson ratio
ρ	7.8 kg/dm^3	Material density
α_{barus}	$1 \cdot 10^{-8}$ Pa^{-1}	Lubricant pressure-viscosity coefficient
η_0	0.1 Pas	Lubricant viscosity at ambient pressure

Table 13.1: Estimated geometrical and material proprieties of *NU 1010 ECP*

Roller Bearing Behavior in Dry Contact The case based on the contact modeling technique developed in Chapter 10 is shown in Figure 13.6, where are shown all the bearing reactions to the imposed inner ring displacement.

Is clearly visible how in this case the centrifugal load really matter. Even if the roller behaves substantially in a similar way with different rotational speeds, this difference in the bearing behavior can be explained by the amount of rolling elements composing the bearing. If each rolling element has a inner ring contact load reduction of few tens of Newton due to the centrifugal load which push in the same direction. If this value is multiplied by a factor of eight, which can be the number of rolling element in contact due to clearance, then the factor becomes easily the reduction factor of the reaction load in Figure 13.6. Moreover, the behavior periodicity above-mentioned is visible since in the plots nine peaks are visible.

The shaft speed has less influence on the reaction moments, since the centrifugal load do not provokes any concentrated moment w.r.t. the roller's gravity center. Thus

δ_x	$3 \cdot 10^{-2}\ mm$
δ_y	$3 \cdot 10^{-2}\ mm$
δ_z	$0\ mm$
γ_x	$0.03°$
γ_y	$0.02°$

Table 13.2: Input displacements for the simulation of *NU 1010 ECP*

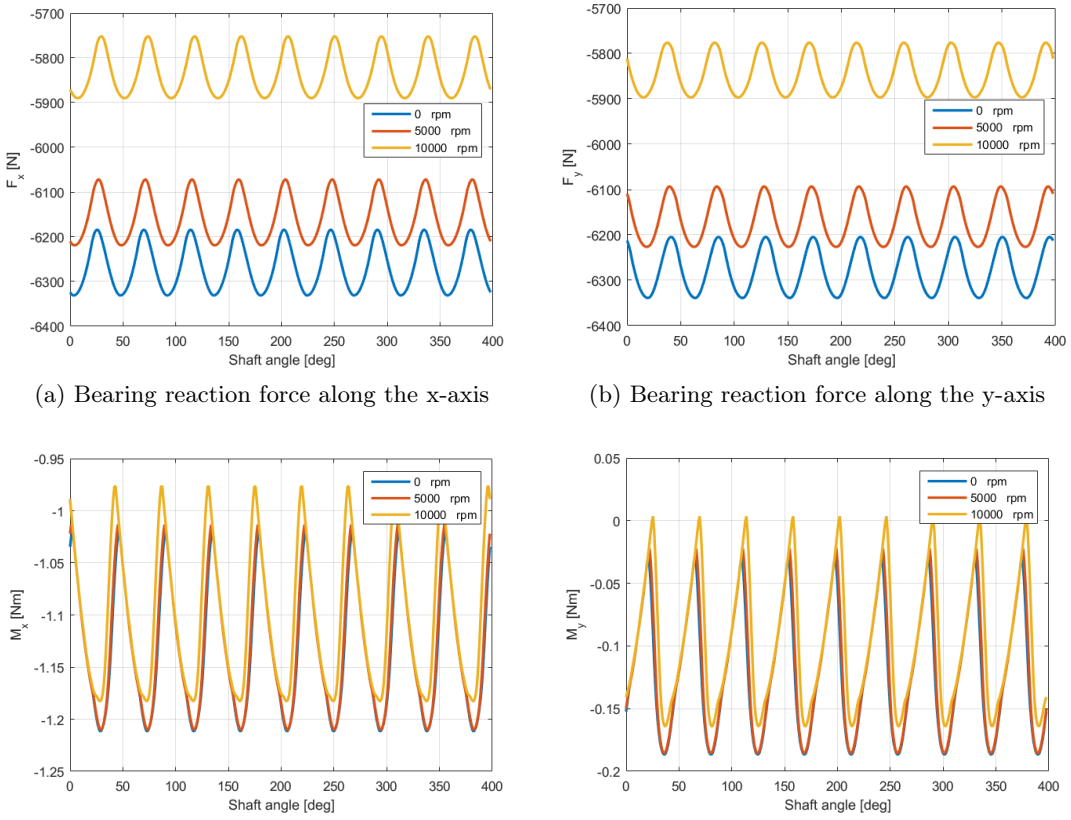

(a) Bearing reaction force along the x-axis

(b) Bearing reaction force along the y-axis

(c) Bearing reaction moment along the x-axis

(d) Bearing reaction moment along the y-axis

Figure 13.3: Roller bearing reaction forces, moments assuming dry contact

the moments variation is just due to the non linear contact behavior.

Cylindrical Roller Bearing Behavior in EHL Contact Now the dry contact model is replaced with the EHL model which accounts for the lubricant behavior and interaction between lubricant and bodies. The load conditions of this bearing are exactly the same of the previous case since comparable results are required, the load conditions are then listed in Table 13.2.

Computing the solution is immediately clear that the process is slower than the dry one, this should not be a surprise since more is the model accuracy and more is the

computational effort required. Even if the computational time is increased, the process still results as acceptable. The results of the simulation are shown in Figure 13.7.

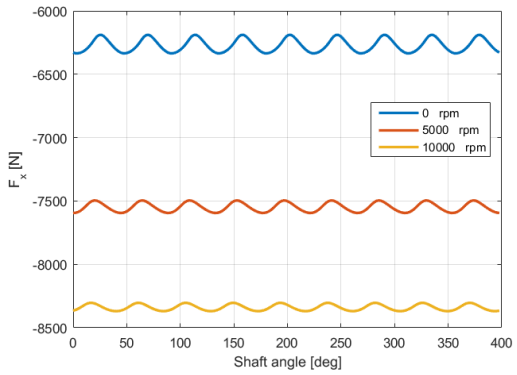

(a) Bearing reaction force along the x-axis

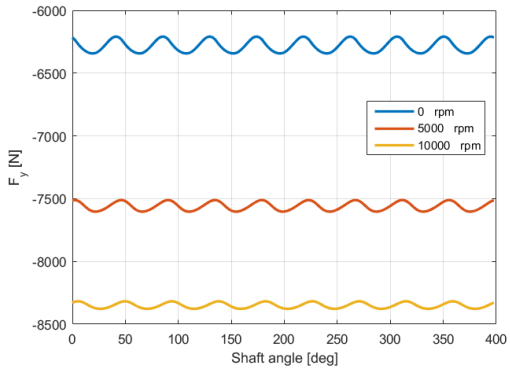

(b) Bearing reaction force along the y-axis

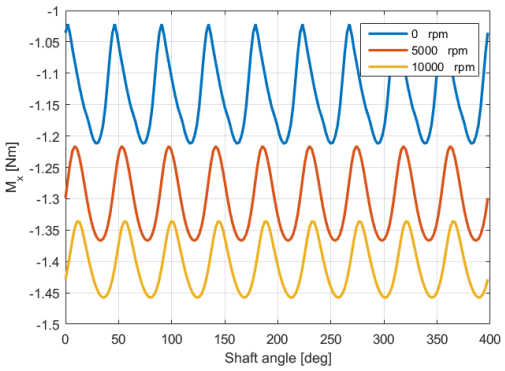

(c) Bearing reaction moment along the x-axis

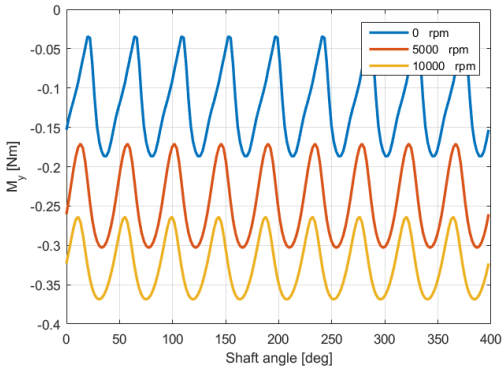

(d) Bearing reaction moment along the y-axis

Figure 13.4: Roller bearing reaction forces, moments assuming EHL contact

As expected, the behavior referred to 0 *rpm* shaft speed is exactly the same achieved with the dry contact model of Figure 13.6 while in this case, increasing the shaft speed the reaction forces and moments increase due to the lubricant effect on the rolling elements which increases the roller deformation, so the load distribution.

13.4 Tapered Roller Bearing Behavior

This section shows the behavior of a tapered roller bearing (Figure), as usual it is based on the contact modeling described thorough Chapter 12. As study-case the bearing *33010/Q* from the SKF catalog, which has dimensions similar to the ones of *NU 1010 ECP*. As already done with the previous cases, the internal geometry has been estimated by the ISO norms [36] and [35]. The estimated values and the ones from the catalog are listed in Table 13.3.

In order to compute the solution the displacements of Table 13.4 are set as model's input. The solution is then computed with both contact models in order to have a clear

Figure 13.5: Tapered Roller Bearing

B	24 mm	Inner ring width
B_o	19 mm	Outer ring width
D_{ob}	80 mm	Outer bore diameter
D_{ib}	50 mm	Inner bore diameter
D_g	7.84 mm	Greater roller diameter
D_l	7.06 mm	Lower roller diameter
L	17 mm	Roller length
d_{fl}	2.6 mm	Roller axis and flange contact point distance
α	6°	Contact angle
D_{pw}	65 mm	Pitch diameter
Z	24	Number of rolling elements
E	206 GPa	Young modulus
ν	0.3	Poisson ratio
ρ	7.8 kg/dm^3	Material density
α_{barus}	$1 \cdot 10^{-8}$ Pa^{-1}	Lubricant pressure-viscosity coefficient
η_0	0.1 Pas	Lubricant viscosity at ambient pressure

Table 13.3: Estimated and from catalog values of the geometrical and material proprieties of *33010/Q*

comparison between the two cases.

The shaft speed rotation starts again from 0 rpm and it goes up to 10000 rpm with an intermediate step at 5000 rpm. The shaft rotation angle is given in order to have a correspondent cage rotation of 180°, even if a minor rotation angle would be sufficient since is expected a behavior periodicity of $360°/Z = 15°$.

Tapered Roller Bearing Behavior in Dry Contact In this case the reaction forces and moments do not have visible fluctuations rotating the shaft, this is because of the greater amount of rolling element composing the bearing. In fact in this case the amount of rolling element is 24 while the bearing used as study case for radial roller bearings had 18 rolling element. Figure 13.6 shows also how increasing the shaft speed, the reaction forces and moments become smaller due to the centrifugal load which reduces the contact force between the inner raceway and the rolling element.

δ_x	$3 \cdot 10^{-2}\ mm$
δ_y	$3 \cdot 10^{-2}\ mm$
δ_z	$0\ mm$
γ_x	$0.03°$
γ_y	$0.02°$

Table 13.4: Input displacements for the simulation of *33010/Q*

Tapered Roller Bearing Behavior in EHL Contact Then the same solution is computed accounting for lubrication, as usual a more speed-dependent behavior is expected since the surfaces speed has a big influence in the lubricant effects on the contact. Figure 13.7 shows the bearing behavior accounting for centrifugal load and EHL.

In fact the computed solution has a strongly depend on the shaft speed due to the lubricant effect. In this case increasing the shaft speed, also the reaction forces and moments increase.

Comparison between Tapered Roller bearing in Dry contact and EHL In this paragraph a comparison between the two developed methods in showed in order to evaluate the differences and the advantages of one method w.r.t. another one. Figure 13.8 shows the computed comparison between the methods.

The first difference between the dry model and the EHL model behavior is that the increment of the shaft rotational speed has two opposite effect. Neglecting the lubrication the centrifugal force induce a decrease in the reaction forces and moments, while accounting for EHL the result achieved sometimes is exactly the opposite, since increasing the shaft speed also the surfaces speed increase then the lubricant effect becomes more important than the centrifugal load. It is clearly visible in the reaction forces along the x, y axis. Furthermore the lubricant effect is preponderant in the bearing behavior since due to this the reaction forces and moments increases even of a factor of $200 \div 400\%$.

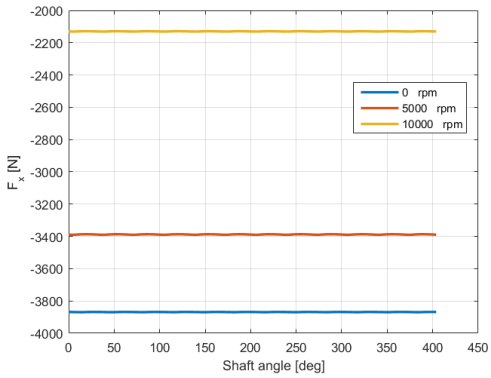

(a) Bearing reaction force along the x-axis

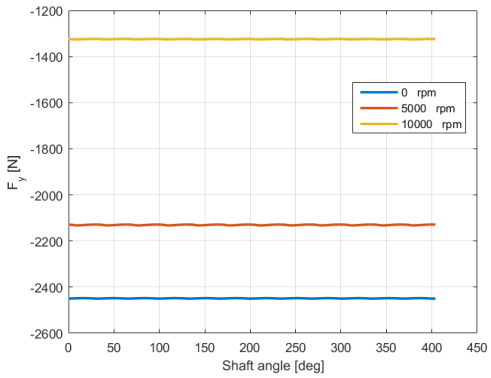

(b) Bearing reaction force along the y-axis

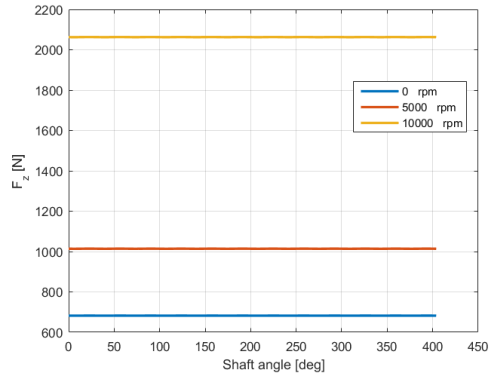

(c) Bearing reaction force along the z-axis

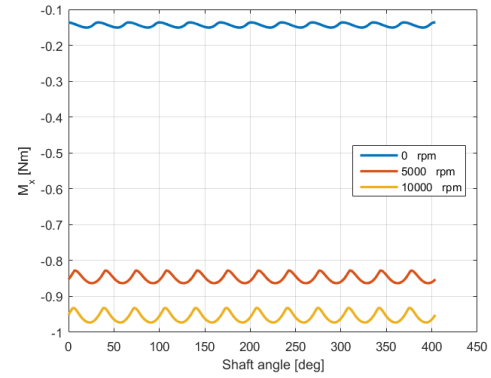

(d) Bearing reaction moment along the x-axis

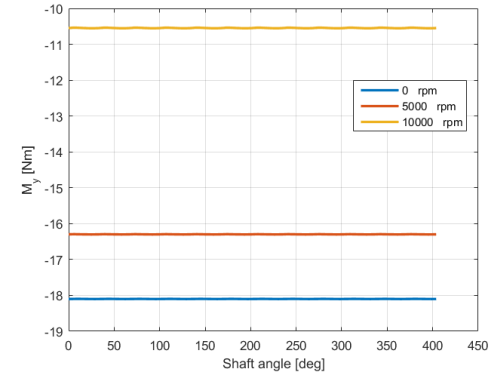

(e) Bearing reaction moment along the y-axis

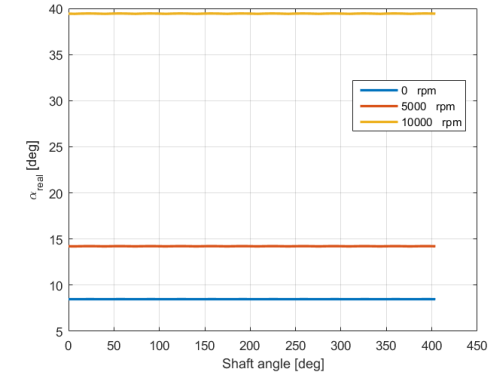

(f) Real contact angle

Figure 13.6: Roller bearing reaction forces, moments and real contact angle assuming Dry contact

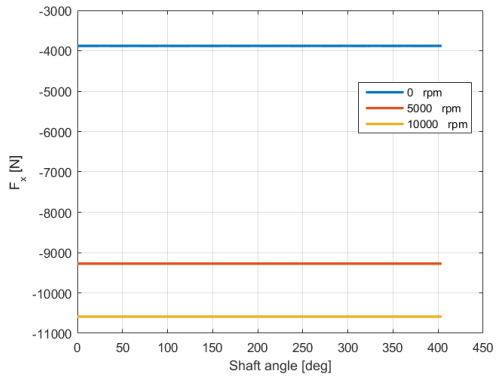

(a) Bearing reaction force along the x-axis

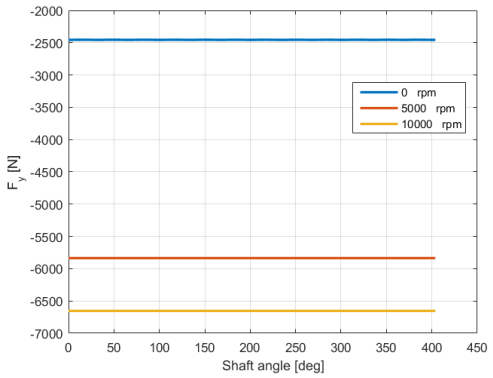

(b) Bearing reaction force along the y-axis

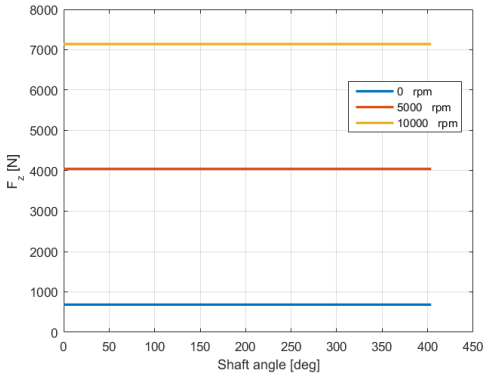

(c) Bearing reaction force along the z-axis

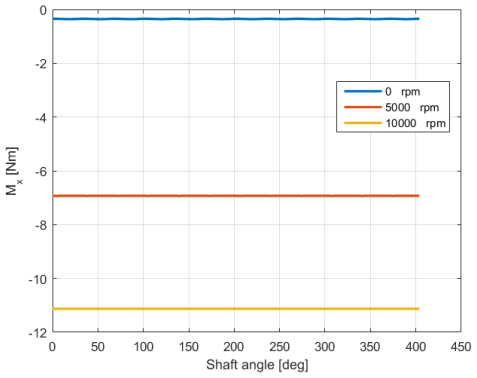

(d) Bearing reaction moment along the x-axis

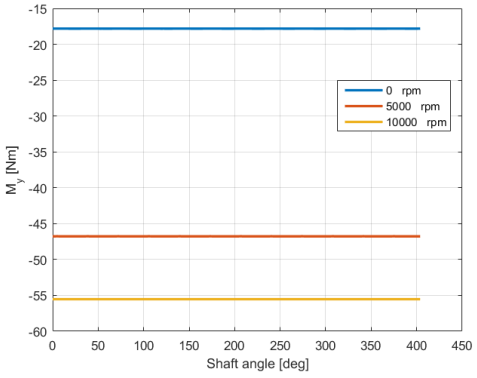

(e) Bearing reaction moment along the y-axis

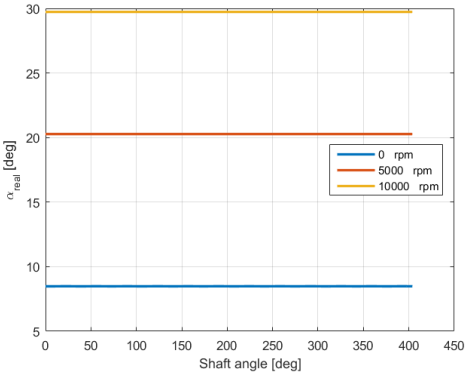

(f) Real contact angle

Figure 13.7: Roller bearing reaction forces, moments and real contact angle accounting for lubrication

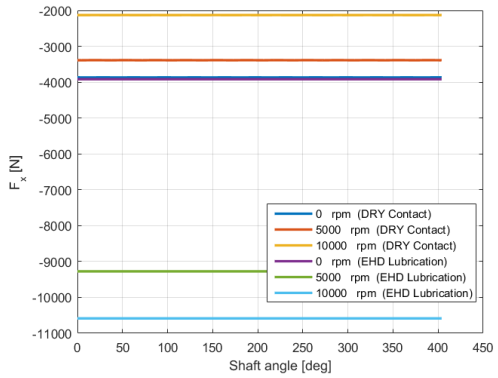

(a) Bearing reaction force along the x-axis

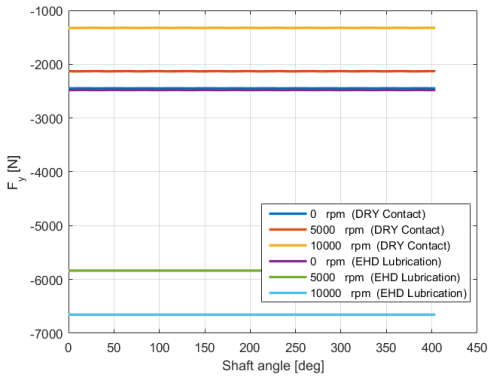

(b) Bearing reaction force along the y-axis

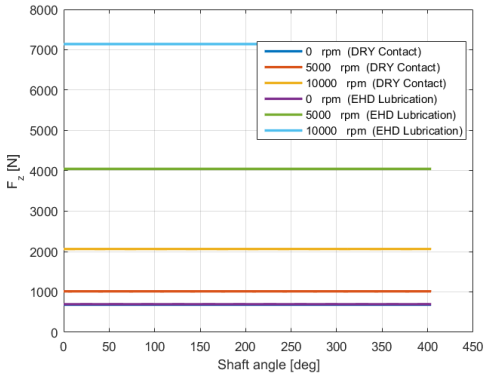

(c) Bearing reaction force along the z-axis

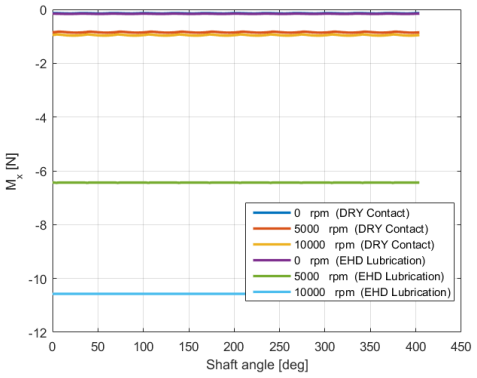

(d) Bearing reaction moment along the x-axis

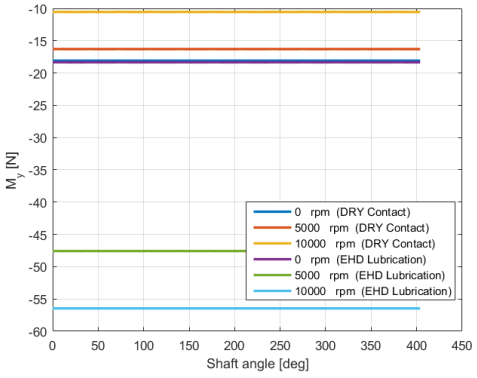

(e) Bearing reaction moment along the y-axis

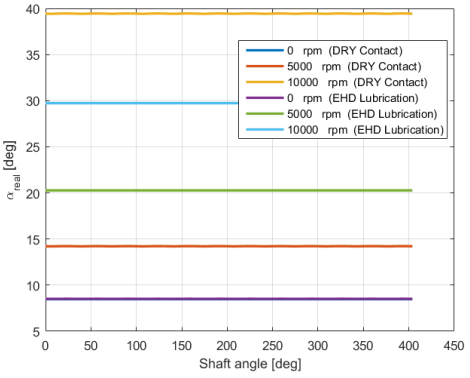

(f) Real contact angle

Figure 13.8: Roller bearing reaction forces, moments and real contact angle computed with the two models compared

Chapter 14

Roller Bearings Modeling Techniques Conclusions

In this part, the developed modeling techniques for cylindrical and tapered roller bearings have been described. First the roller crowning and the slicing technique have been introduced to describe the roller-raceway penetration. Then, the dry contact model based on the Dinnik's formulas has been used to model the discretized line contact. The first model also accounts for centrifugal load and clearance. While the flange contact in tapered roller bearings has been introduced as constraint. As second model, the dry contact has been replaced with the EHL contact model in order to account for lubrication. Introducing the lubricant effects, the solution increased its reliability while increasing the computational effort required.

The modeling techniques proposed in this part allow the computationally efficient and high fidelity predictions of cylindrical and tapered roller bearings under different assumptions. The most important assumption concerns the lubrication of the contact. In fact, if the contact is modeled as dry, the fidelity becomes questionable, while if the lubrication is introduced, the fidelity increases significantly, while on the other hand the computational effort required to compute the solution also increases.

For a given inner ring displacement the models return the reaction forces and moments accounting for the coupling between axial, radial and tilting motion. The developd modeling techniques can take into account the most relevant phenomena such as centrifugal loads, gyroscopic moments, lubrication and roller's crowning.

It is expected that in many types of analysis, the time to achieve the solution results more than acceptable if compared with the fidelity offered. As second implementation step, the iterative processes can be optimized in order to reduce the computational cost of the procedure, achieving shorter computational time, hence a more suitable implementation.

Thanks to the modular implementation and to the contact models, the bearing types covered can be extended with a minimal effort. For example the modeling techniques can be easily extended to barrel roller bearings (Figure 14.1) and self-aligning roller bearings (Figure 14.2) since the contact can be described with the techniques developed in this part.

Possible extensions and improvements are discussed in the next chapter.

Figure 14.1: Barrel Roller Bearing

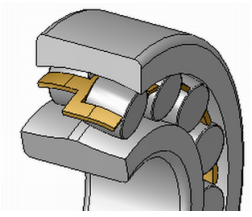

Figure 14.2: Self-Aligning Roller Bearing

Chapter 15

Future Developments

The modeling techniques developed in this work can predict the steady-state behavior of a rolling element bearing under few assumptions. The future developments concern overcoming the limitations originating from limitations. The first improvement can indeed be to account for the dynamics of the element motion. Introducing degrees of freedom for describing the dynamic motion of the rolling element, the solution will be more accurate, since more phenomena could be predicted (e.g. rolling element bouncing between the raceways).

The future improvements can be divided in two levels. The first one is the contact scale, while the second one is the bearing.

Concerning the contact, many improvements can be done. A first one is to account for the damping of the lubricated contact. Many models already exist to predict the contact damping for a single exciting frequency, even if due to the non linearity, the superposition principle cannot be applied. Thus an error evaluation has to be done in order to evaluate the error produced summing the effects of different frequencies. If the superposition principle produces non-reliable results, then a novel technique to evaluate the lubricated contact damping excited with a non-periodic excitation needs to be developed or identified in literature. A second contact modeling improvement is to account for contact friction, since it can give multiple advantages. The first is to have a prediction of the whole bearing friction coefficient. Secondly, it allows to describe the motion of the cage more accurately, which causes the periodicity of stiffness fluctuations hence a possible source of vibrations. To predict friction, a more advanced model for lubricated contact has to be introduced, since local pressure within the lubricated contact area needs to be evaluated. Due to the accuracy of this model, it could also be used to predict wear and stresses, and hence for durability purposes.

Furthermore, all these techniques can be applied to many other cases, such as gears. In fact, the contact between meshing gears teeth is a non-conformal contact, hence the modeling techniques developed for bearings can be applied to gears and vice versa. For example the contact modeling developed for the rollers, can be used to model the contact in spur and helical gears since these are typically also designed to make line contact. Hypoid and bevel gears (Figure 15.1),typically make point contact, due to restrictions in common manufacturing techniques. The point contact modeling techniques developed in this work could be applied there too.

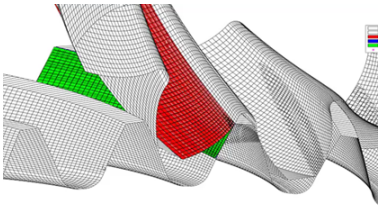

Figure 15.1: Bevel gears meshing

The bearing level improvements can start with a time dependent solution, in order to account for the dynamics of the rolling elements. Introducing the dynamics of rollers and cage more phenomena can be predicted, such as rolling element bouncing between the raceways, or rolling element slipping on the raceway due to a high inner ring acceleration etc. A time dependent solution will likely increase the computational cost, even if the solution process may become more stable and robust. A second but equally important improvement can be to account for the compliance of the surrounding structure, as bearing rings, shaft and housing. Figure 15.2 shows a bearing analysis, involving a combination of FE and multibody modeling, to account for the rings' compliance.

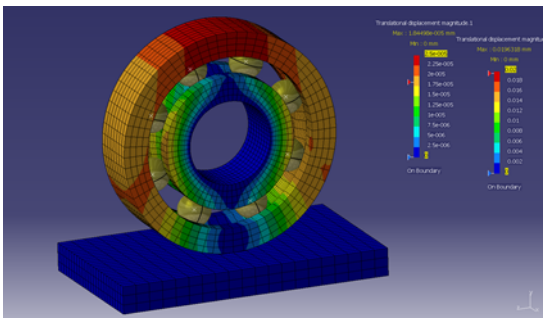

Figure 15.2: Analysis of a bearing with combination of FE and multibody modeling

The compliance of the surrounding structure can influence the internal load distribution of the bearing as pointed out by Harris and Kotzalas [11]. It can be done with a hybrid FE-analytical procedure. Siemens PLM has developed such an approach for gears (see [42]). The procedure splits the problem in two sub-problems: an FE analysis to evaluate the compliance of the structure far from the contact, hence gentle stress gradients and complex geometry, where a coarser mesh is sufficient, while analytical contact modeling in the contact area where the stress gradients are strong but the geometry is simple.

Introducing the above-mentioned, the accuracy of the behavior prediction can achieve very high levels with high reliability, hence highly accurate $N\&V$ analysis. Moreover these improvements would allow to use these modeling techniques to investigate the durability of bearings. In both $N\&V$ and durability analysis these modeling techniques allow for fast *what if* analyses to accurately design alternatives.

Bibliography

[1] Arvid Palmgren. "Ball and roller bearing engineering". In: *Philadelphia: SKF Industries Inc., 1959* 1 (1959) (cit. on p. 3).

[2] AB Jones. "The mathematical theory of rolling element bearings". In: *Mechanical Design and Systems Handbook* (1964), pp. 13–1 (cit. on p. 3).

[3] AB Jones. "A general theory for elastically constrained ball and radial roller bearings under arbitrary load and speed conditions". In: *Journal of Basic Engineering* 82.2 (1960), pp. 309–320 (cit. on p. 3).

[4] AB Jones and JM McGrew Jr. *Rotor-bearing Dynamics Technology Design Guide. Part 2. Ball Bearings*. Tech. rep. DTIC Document, 1978 (cit. on p. 3).

[5] AB Jones and JM McGrew Jr. *Rotor-bearing Dynamics Technology Design Guide. Part 3. Tapered Roller Bearings*. Tech. rep. DTIC Document, 1979 (cit. on p. 3).

[6] AB Jones and JM McGrew Jr. *Rotor-bearing Dynamics Technology Design Guide. Part 4. Cylindrical Roller Bearings*. Tech. rep. DTIC Document, 1979 (cit. on p. 3).

[7] Staffan Andréason. "Load distribution in a taper roller bearing arrangement considering misalignment". In: *Tribology* 6.3 (1973), pp. 84–92 (cit. on p. 3).

[8] S Andreason. "Theoretische Grundlagen fur die Berechnung von mit Kraften und Momenten belasteten zweireihigen Schragkugellagern". In: *Konstruktion* (1970), pp. 245–248 (cit. on p. 3).

[9] S Andreason. "Theoretische Grundlagen fur die Berechnung von mit Kraften und Momenten belasteten Rillenkugellagern". In: *Konstruktion* (1969), pp. 105–109 (cit. on p. 3).

[10] JY Liu. "Analysis of tapered roller bearings considering high speed and combined loading". In: *Journal of Lubrication Technology* 98.4 (1976), pp. 564–572 (cit. on p. 3).

[11] Tedric A Harris and Michael N Kotzalas. *Essential concepts of bearing technology*. CRC press, 2006 (cit. on pp. 3, 10–13, 18, 100).

[12] Tedric A Harris and Michael N Kotzalas. *Advanced concepts of bearing technology: rolling bearing analysis*. CRC Press, 2006 (cit. on pp. 3, 81).

[13] H Hertz. *On the contact of Rigid Elastic Bodies and on Hardness, Miscellaneous Papers*. 1886 (cit. on pp. 4, 8).

[14] Osborne Reynolds. "On the Theory of Lubrication and Its Application to Mr. Beauchamp Tower's Experiments, Including an Experimental Determination of the Viscosity of Olive Oil." In: *Proceedings of the Royal Society of London* 40.242-245 (1886), pp. 191–203 (cit. on pp. 4, 28).

[15] AM Ertel. "Hydrodynamic lubrication based on new principles". In: *Akad. Nauk. SSSR, Prikladnaya Matematika i Mekhanika* 3.2 (1939), pp. 41–52 (cit. on p. 4).

[16] AN Grubin and I Vinogradova. "Fundamentals of the hydrodynamic theory of lubrication of heavily loaded cylindrical surfaces". In: *Investigation of the contact Machine Components* 30 (1949), pp. 115–166 (cit. on p. 4).

[17] Bernard J Hamrock and Duncan Dowson. "Isothermal elastohydrodynamic lubrication of point contacts: Part 1—Theoretical formulation". In: *Journal of Lubrication Technology* 98.2 (1976), pp. 223–228 (cit. on p. 4).

[18] Achi Brandt and Oren E Livne. *Multigrid techniques: 1984 guide with applications to fluid dynamics*. Vol. 67. SIAM, 2011 (cit. on p. 4).

[19] Ysbrand Hans Wijnant. *Contact dynamics in the field of elastohydrodynamic lubrication*. Universiteit Twente, 1998 (cit. on pp. 4, 28–31).

[20] Harold A Rothbart. *Mechanical Design and Systems Handbook*. 2nd. McGraw-Hill, 1985 (cit. on pp. 4, 58, 59).

[21] Arvid Palmgren. *Grundlagen der Wälzlagertechnik*. Franckh'sche Verlag, 1950 (cit. on p. 4).

[22] Karlheinz Kunert. "Spannungsverteilung im Halbraum bei elliptischer Flächenpressungsverteilung über einer rechteckigen Druckfläche". In: *Forschung auf dem Gebiet des Ingenieurwesens A* 27.6 (1961), pp. 165–174 (cit. on p. 4).

[23] Luc Houpert. "An engineering approach to hertzian contact elasticity—Part I". In: *Journal of tribology* 123.3 (2001), pp. 582–588 (cit. on pp. 4, 59).

[24] C Weber and K Banaschek. "Formänderung und Profilrücknahme bei Gerad-und Schrägverzahnten Antriebstechnik". In: *Vieweg, Braunschweig* 11 (1953) (cit. on p. 4).

[25] Roman Teutsch and Bernd Sauer. "An alternative slicing technique to consider pressure concentrations in non-Hertzian line contacts". In: *Journal of Tribology* 126.3 (2004), pp. 436–442 (cit. on pp. 4, 58, 59).

[26] H Reussner. "Druckflächenbelastung und Oberflächen verschiebung im Wälzcontact von Rotationskörpen". In: Ph. D. Thesis University of Karlsruhe, Germany (in German). 1977 (cit. on p. 4).

[27] H Moes. "Optimum similarity analysis with applications to elastohydrodynamic lubrication". In: *Wear* 159.1 (1992), pp. 57–66 (cit. on pp. 4, 30, 70).

[28] ERM Gelinck and DJ Schipper. "Calculation of Stribeck curves for line contacts". In: *Tribology International* 33.3 (2000), pp. 175–181 (cit. on pp. 4, 69, 70).

[29] Tokio Sasaki, Haruo Mori, and Norio Okino. "Fluid Lubrication Theory of Roller Bearing—Part I: Fluid Lubrication Theory for Two Rotating Cylinders in Contact". In: *Journal of Basic Engineering* 84.1 (1962), pp. 166–174 (cit. on p. 4).

[30] H Rahnejat. "Computational modelling of problems in contact dynamics". In: *Engineering analysis* 2.4 (1985), pp. 192–197 (cit. on p. 4).

[31] Benedikt Wiegert, Hartmut Hetzler, and Wolfgang Seemann. "A simplified elastohydrodynamic contact model capturing the nonlinear vibration behaviour". In: *Tribology International* 59 (2013), pp. 79–89 (cit. on pp. 4, 69, 73, 74).

[32] David E Brewe and Bernard J Hamrock. "Simplified solution for elliptical-contact deformation between two elastic solids". In: *Journal of Lubrication Technology* 99.4 (1977), pp. 485–487 (cit. on p. 12).

[33] JM De Mul, JM Vree, and DA Maas. "Equilibrium and Associated Load Distribution in Ball and Roller Bearings Loaded in Five Degrees of Freedom While Neglecting Friction—Part I: General Theory and Application to Ball Bearings". In: *Journal of tribology* 111.1 (Jan. 1989), pp. 142–155 (cit. on pp. 20, 22–24).

[34] Carl Barus. "Isothermals, isopiestics and isometrics relative to viscosity". In: *American journal of science* 266 (1893), pp. 87–96 (cit. on p. 30).

[35] ISO 76:2006. *Rolling bearings — Static load ratings* (cit. on pp. 41, 88, 91).

[36] ISO 281:2007. *Rolling bearings — Dynamic load ratings and rating life* (cit. on pp. 41, 88, 91).

[37] Jeroen Anton Wensing. *On the dynamics of ball bearings*. University of Twente, 1998 (cit. on p. 41).

[38] Joseph V Poplawski, Steven M Peters, and Erwin V Zaretsky. "Effect of roller profile on cylindrical roller bearing life prediction—Part I: Comparison of bearing life theories". In: *Tribology Transactions* 44.3 (2001), pp. 339–350 (cit. on p. 59).

[39] Hiroki Fujiwara et al. "Optimized logarithmic roller crowning design of cylindrical roller bearings and its experimental demonstration". In: *Tribology Transactions* 53.6 (2010), pp. 909–916 (cit. on pp. 61, 62).

[40] Hiroki Fujiwara and Tatsuo Kawase. "Logarithmic profiles of rollers in roller bearings and optimization of the profiles". In: *NTN Technical Review* 75 (2007), pp. 140–148 (cit. on pp. 61, 62).

[41] Enrico Ciulli and Bruno Piccigallo. *Complementi di lubrificazione*. SEU, 1996 (cit. on p. 72).

[42] Gert Heirman. "Extension of the ease-off concept for contact detection and penetration computation." US 2015P01440US01 (10247-15001A). 2015 (cit. on p. 100).